## Dissertation zur Erlangung des Doktorgrades der Fakultät für Chemie und Pharmazie der Ludwig-Maximilians-Universität München

# Design of Experiment-Based Optimization of Nebulized Pulmonary PBAE-siRNA Delivery Systems



## **Adrian** Philipp Eckart Kromer

aus

Stuttgart, Deutschland

2025

## **Eidesstattliche Versicherung**

## Erklärung

Diese Dissertation wurde im Sinne von § 7 der Promotionsordnung vom 28. November 2011 von Frau Prof. Dr. Olivia Merkel betreut.

## Eidesstattliche Versicherung

Diese Dissertation wurde eigenständig und ohne unerlaubte Hilfe erarbeitet.

München, 15.06.2025

Adrian Kromer

Dissertation eingereicht am: 27.06.2025

1.Gutachterin: Prof. Dr. Olivia Merkel

2.Gutachter: Prof. Dr. Wolfgang Frieß

Mündliche Prüfung am: 23.09.2025

## "PER ASPERA AD ASTRA"

- Seneca

## **INDEX**

I. Ain	n of the Thesis	
II. In	troductiontroduction	2
1.	Potential and Challenges of siRNA-Based Therapies	2
2.	PBAEs as delivery candidates and the need for control	3
3.	Pharmaceutical Experimental Design	5
4.	Preparation of PBAE nanoparticles	8
5.	The human lung as barrier and target	9
	Design of Experiments Grants Mechanistic Insights into the Synthesis of Sperminal PBAE Copolymers	
1.	Abstract	
2.	Introduction	
3.	Methods and Materials	16
4.	Results and Discussion	19
5.	Conclusion	29
6.	Acknowledgements	29
7.	Supporting Information	30
IV. M	achine Learning on an Orthogonal Polymer Library Reveals Governing Factor	S
and (	Optimizes PBAE Copolymers' Synthesis and Performance	46
1.	Abstract	47
2.	Introduction	48
3.	Materials and Methods	50
4.	Results and Discussion	57
5.	Conclusion	68
6.	Data Availability	68
7.	Acknowledgements	68
8.	Supporting Information	69
	bulization of RNA-Loaded Micelle-Embedded Polyplexes as a Potential Treatmorphic Pulmonary Fibrosis	
1.	Abstract	83
2.	Introduction	84
3	Materials and Methods	87

4.	Results and Discussion	94
5.	Conclusion	107
6.	Acknowledgments	107
7.	Supporting Information	108
VI. S	Summary and Perspective	115
VII. Publication List VIII. Reference List		117
		119
IX. Acknowledgments		128

### I. Aim of the Thesis

The aim of this work was the development of a PBAE polymer-based siRNA therapy delivery system for pulmonary application using DoE as streamlining tool. To achieve this, siRNA was encapsulated into polyplexes through electrostatic interaction with PBAE polymers which were then nebulized to achieve deep lung deposition. For this cause, in a first step the polymer synthesis was optimized and characterized to gain control and understanding of the process. Here, DoE was applied to reduce the number of experiments and resources spent to control the synthesis. Utilizing the controlled synthesis, numerous polymers were prepared and tested regarding their stability, toxicity and efficiency in vitro and in vivo. Here, core principles governing the nanoparticles performance were identified and optimized. To achieve the goal of pulmonary application, different nanoparticles were tested for nebulization-based delivery. Therefore, nanoparticle stability in regards of physicochemical characteristics and efficacy after VMN based nebulization was investigated. Nanoparticles encapsulating therapeutic siRNA were able to mitigate disease relevant gene expression after nebulization and application onto diseased ex vivo human tissue. Finally, the manufacturing process of the nanoparticles was optimized applying DoE on a microfluidic setup. Large scale production of clinically relevant batch size was tested and evaluated.

**Chapter II** gives a brief introduction into the most relevant topics covered in this work.

**Chapter III** describes the optimization and characterization of the synthesis of the PBAE polymers and the validation of the DoE model describing the synthesis.

**Chapter IV** is the continuation of the work presented in chapter 2. It describes how the key findings and characteristics of all polymers were analyzed, and a new best performing candidate was found. The challenges associated with the translation from *in vitro* to *in vivo* models are briefly discussed.

**Chapter V** demonstrates how VMNs are useful nebulization devices which can be used to nebulize different PBAE based nanoparticles into aerosols with favorable size ranges for deep alveolar deposition. The approach is validated using diseased *ex-vivo* human tissue.

**Chapter VI** summarizes the concluding findings of the work and gives an outlook on the topics which still need further investigation.

## II. Introduction

## 1. Potential and Challenges of siRNA-Based Therapies

Small interfering RNA (siRNA) is a ubiquitously expressed regulatory ribonucleic acid which plays a crucial role in cell homeostasis. Under physiological conditions it is derived from long dsRNA which is cut into small fragments of 20-24 base pairs by dicer enzymes<sup>1,2</sup>. Its mechanisms were firstly described in 1998<sup>3</sup>. Briefly, the guide strand associates with an argonaut protein and forms the RNA-Induced Silencing Complex (RISC) which scans the cytosol for complementary mRNA sequences. If the RISC finds and attaches to a complementary mRNA, it induces mRNA cleavage and thereby downregulates the targeted gene expression<sup>4</sup> (Figure 1). This mechanism is essential for the gene regulation in all living cells. Crucially, it can be utilized as treatment for previously undruggable diseases by downregulating relevant genes through synthetically synthesized complementary siRNA<sup>5</sup>.

Though the potential for siRNA-based therapies seems endless, it is limited by two challenges. The first is to identify disease relevant proteins and find the best performing RNA sequence<sup>6,7</sup>. The second is the successful delivery of siRNA into the cytosol of the target cells. Due to their high electrochemical charge, RNA gets poorly internalized by cells and is subjected to repulsion from the negatively charged cell membrane<sup>8</sup>. Additionally, free intercellular siRNA gets recognized by Toll-like receptors and can induce immune reactions<sup>9</sup>. Also, it is rapidly degraded by ubiquitously expressed RNase enzymes. To protect the RNA structure and overcome the delivery associated challenges, scientists developed numerous approaches in the last decades<sup>8</sup>. Most prominent due to their recent clinical success are lipid nanoparticle (LNP) formulations like Onpattro®, which was approved in 2018<sup>10</sup>. It consist of several lipids and cholesterol and proofed to be a save and efficient delivery agent<sup>11</sup>. However, they are challenging to manufacture and are associated with high costs. The very first successful trials of siRNA delivery were done many years before the first LNP formulation.

Polylysine polymers were one of the first compound classes which were applied to deliver nucleic acids into cells<sup>12</sup>. Polymers in general have many advantages as delivery vehicle. They are cheaply synthesized and easily tunable and there are numerous different structures available<sup>13</sup>. Nanoparticles (NPs) can be formulated in an easy fashion applying them. However, despite these advantages, there is no clinically approved polymer-based therapy by the time of this thesis<sup>14</sup>. One reason can be the heterogenous nature of polymers and their difficulty to control during synthesis, which makes a reproducible nanoparticle formulation challenging.

Additionally, polycationic polymers like polyethylenimine (PEI) are associated with major cytotoxic concerns<sup>15,16</sup>.

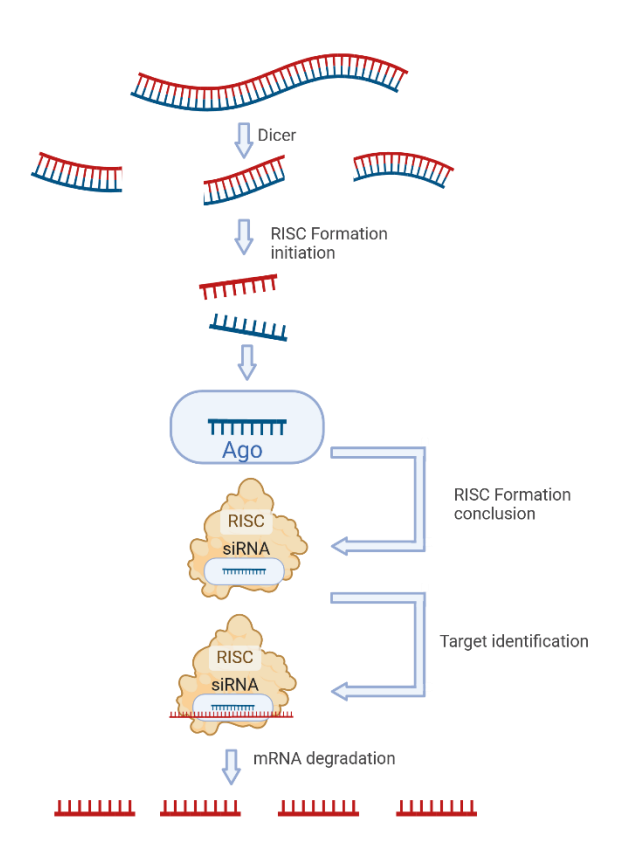


**Figure 1.** Schematic representation of mRNA cleavage through the RISC and siRNA generation through dicer enzymes. Generated with BioRender.

## 2. PBAEs as delivery candidates and the need for control

In the year 2000 Robert Langer and his coworkers introduced poly(β-aminoesters) (PBAE) as biodegradable polymer class for self-assembled pDNA delivery. These polymers are synthesized through Michael-addition of diacrylate groups with primary or secondary amines in a step-growth mechanism<sup>17</sup>. The resulting tertiary amines are protonated at physiological pH which enables them to electrostatically encapsulate DNA and RNA molecules into NP's. Pure PBAEs are quickly degraded through ester hydrolysis of their backbone in a pH dependent manner. This is an important property to reduce cytotoxicity which is often associated with polycations. In NP form they are much more resistant to hydrolysis and stabilize their cargo for prolonged timeframes<sup>18</sup>. Both attributes are necessary to protect the encapsulated siRNA during the application process but also degrade the polymer after successful delivery to the cytosol.

Early research on PBAEs quickly found out that the tertiary amines in the backbone could only achieve insufficient electrostatic encapsulation of nucleic acids. A broadly applied modification to improve the encapsulation efficiency was the end-capping of polymers. For this, molecules with one or more primary and secondary amines were covalently bound to the terminal acrylate groups of PBAEs in a subsequent reaction step. This method could boost the performance of PBAE NPs substantially<sup>19,20</sup>.

In the last decade, numerous researchers found that copolymers, combining a polycationic subunit and a hydrophobic subunit could realize superior transfection performances, forming the next evolution stage of PBAE Polymers. The polycationic subunit thereby is necessary for higher encapsulation efficiency mitigating the need of end-capping groups and the hydrophobic unit is necessary to achieve higher cell uptake and endosomal escape<sup>21</sup>.

Until today endosomal escape is considered the biggest barrier for successful gene delivery to the cytosol. Less than 5% of internalized nanoparticles are able to escape the endosome<sup>22</sup>. There are several mechanisms proposed as to how nanoparticles can escape the endosome. The firstly proposed mechanism is the "Proton Sponge" effect. It postulated that amines in the polymer structure would be able to buffer the physiological acidification of endosomes by "catching" the protons. This would lead to an increased proton influx, followed by osmotic swelling and ultimately bursting of endosomes which would finally release the cargo<sup>23</sup>. The proton sponge effect is currently regarded as beneficial at best but not as main driving force of endosomal escape<sup>24</sup>. An augmented theory postulated a particle swelling upon acidification which is accompanied by shedding of polymers from the nanoparticle. These shed polymers become free to interact with the endosomal membrane leading to pore formation or burst<sup>25</sup>. Alternatively, it was postulated that hydrophobic polymers or lipids can be incorporated directly into the endosomal membrane destabilizing their structure<sup>26,27</sup>. This destabilization depends on the conformation of the hydrophobic parts and can lead to pore formation or partial membrane disintegration, allowing small nucleic acids to escape through them. It is commonly agreed that unsaturated lipids which show conformational kinks are favorable for destabilizing lipid bilayers<sup>28</sup>. One lipid with a favorable conformation for high fusogenicity and destabilization of membranes is oleylamine which was incorporated into a PBAE copolymer with the polycation Spermine by Jin et al $^{21}$ .

A major problem associated with polymeric nanoparticles is the control of the synthesis. For a clinical application and approval in humans a precise product of unchanging critical quality

attributes (CQA) is necessary. The step growth mechanism of PBAEs is a process which follows several reaction steps until a thermodynamic equilibrium is reached. In the first instance all monomers react to dimers, which subsequently react to a tetramer and so on until chains become so long that their reaction kinetic becomes too small to react further (thermodynamic equilibrium). In the case of copolymers, these reactions can be timely shifted between the two building blocks and mixed building blocks can be formed resulting in unruly mixtures of polymers in different sizes<sup>29</sup>. A typical quality criterion of polymers is their number and weight determined weight  $M_N$  and  $M_W$  given by the following equations:

$$M_N = \frac{\sum N_i M_i}{\sum N_i}$$

$$M_W = \frac{\sum N_i M_i^2}{\sum N_i M_i}$$

with  $N_i$  being the number of polymers with a certain length and  $M_i$  being the respective molecular weight of the polymer chains. The previously described synthesis mechanism can lead to considerable differences between  $M_N$  and  $M_W$ . These differences are described by the polydispersity index (PDI) of polymers derived from the following equation:

$$PDI = \frac{M_W}{M_N}$$

A large PDI can lead to heterogenous nanoparticle suspensions and thereby heterogenous responses. Therefore, researchers are tasked with finding a synthesis method which produces reproducibly polymers with small PDIs and molecular weights inside their target area. One possible solution for this is the application of statistical experimental design to characterize, understand, optimize and control a synthesis process.

## 3. Pharmaceutical Experimental Design

The origin of statistical experimental design or design of experiments (DoE) was in the 1920s in agricultural economic research institutes. Driven by the seasonal restrictions doing agricultural experiments was extremely time consuming, often one experiment would take one year. Out of this problem a statistical approach to experimental design plans was founded to reduce the amount of experiments needed which is still in use as of today<sup>30</sup>. DoE applies orthogonal experiment designs to estimate impact factors on a predefined response and fit a polynomial model equation onto it. This model fit allows the generation of what is called a

response surface applying the response surface methodology (RSM) (Figure 2). Using RSM the model prediction can be plotted visually and optimal setpoints can be easily identified<sup>31</sup>. The big advantage of this becomes clear if one compares the RSM to classical optimization approaches. Imagining a process, e.g. a synthesize which depends on 4 different factors, with each factor being able to assume one of three different levels. A classical approach to understand this synthesis would require doing all possible 3<sup>4</sup> experiments, so 81 in total. DoE and the RSM estimates the effect sizes of each factor directly together with a model offset and would therefore only require 1 experiment for the model offset and 14 experiments for a complete estimation of all factor impacts and possible factor interactions (reasoning for the number of experiments, see below). RSM would therefore allow to find the optimal synthesis settings with a drastically reduced workload. This technique can not only be applied to synthesis but also to numerous classical pharmaceutical problems. In the 1980s and 90s numerous studies applying DoE to optimize tablet mixtures, granulation or hot melt extrudates were conducted<sup>32–34</sup>. More recently DoE was applied in numerous studies to optimize the formulation of LNPs<sup>35–37</sup>.

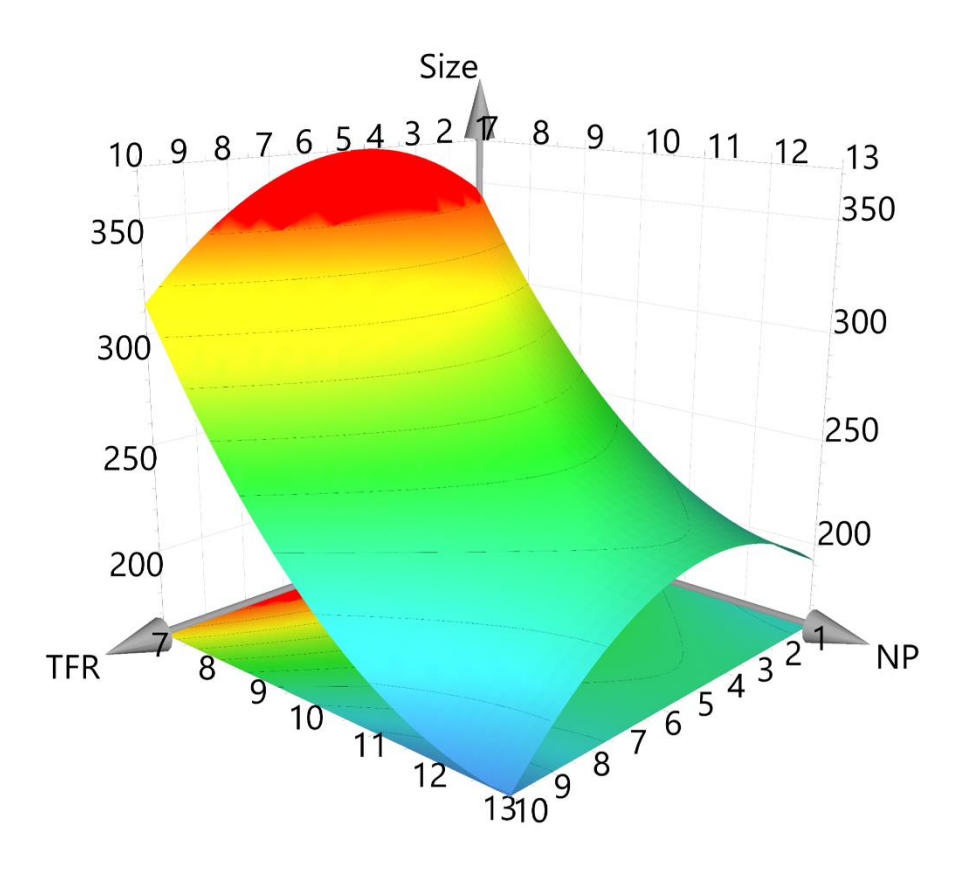


**Figure 2.** Graphical representation of a model equation generated by the response surface methodology. Generated in Modde 13.

To generate clinically and approval relevant models they need to be accurate and statistically significant. DoE models are mostly generated through a multiple linear regression followed by an ANOVA analysis. In detail, a general polynomial equation is postulated with undetermined estimators for each factor, deemed having a significant impact on the model. Since the underlying *true* process can have interactions between factors and factor influences can be potentially quadratic these terms are included into the postulated model as well. In general, a first order interaction model can be described by the model offset, k factor terms, k(k-1)/2 interaction terms and k quadratic factors, with k being the number of factors deemed relevant for the model.

For a process dependent on 3 factors (A, B and C) the model equation would look as follows:

$$y = \beta_0 + \beta_A A + \beta_B B + \beta_C C + \beta_{A^2} A^2 + \beta_{B^2} B^2 + \beta_{C^2} C^2 + \beta_{AB} A B + \beta_{BC} B C + \beta_{AC} A C$$

with  $\beta_i$  being the estimator and A, B, and C being the process parameters. Higher order interactions and cubic or higher influences are often of neglectable magnitude but can be incorporated if significant lack of fit (LOF) is found in the model (see below). For this process  $\sum_{i=1}^{n} \beta_i$  experiments are necessary to get a solution for each estimator. The multiple linear regression function searches a solution for all estimators  $\beta_i$  which minimizes the squared residual sum  $\sum_{j=1}^{n} (y_j - \hat{y}_j)^2$  with  $\hat{y}_j$  being the predicted response for the experimental settings j for each of the conducted experiments. The generated model is tested for significant regression, showing if a significant correlation between the model prediction and the true values was found and lack of fit, showing if the model itself fits the reality in a significant manner or if the model needs to be adjusted by adding or deleting factors. For a lack of fit test there needs to be at least one experiment point which was repeated several times independently. For both cases an ANOVA is conducted as follows<sup>38</sup>:

First the total sum of squares (SS<sub>tot</sub>) is calculated by  $\sum_{i=1}^{n} (y_i - \bar{y})^2$  with  $\bar{y}$  being the mean of all experiments conducted. In a next step the SS of the residuals (SS<sub>res</sub>) is calculated by  $\sum_{i=1}^{n} (y_i - \hat{y})^2$ . From this the SS of the regression (SS<sub>reg</sub>) can be derived by  $SS_{reg} = SS_{tot} - SS_{res}$ . From the SS the respective mean squares (MS) can be calculated by dividing the MS through the respective degrees of freedom (df)

$$MS_x = \frac{SS_x}{df_x}$$

which are estimated after  $df_{res} = N - p$  and  $df_{reg} = p - 1$  with p being the number of factor estimators. To determine the statistical relevance of the regression an F-value can be derived by  $F_{df_{reg},df_{res}} = \frac{MS_{reg}}{MS_{res}}$  and  $\alpha$  levels can be estimated.

Since model estimators often correlate to real process functions or physical interactions it is important to check if not only the correlation of a model is significant but also if all relevant factors are estimated and nothing is overlooked. For this a lack of fit analysis should follow the classical ANOVA. For this it is necessary to have independently repeated experiments in the design plan. If this is the case a SS of the pure error (SS<sub>err</sub>) can be calculated by  $SS_{err} = \sum_{i=1}^{n} \sum_{j=1}^{r_i} (y_{ij} - \bar{y}_i)$  with  $\bar{y}_i$  being the mean of the respective replicate and  $r_i$  being the number of different replicates. The df<sub>err</sub> can be calculated by  $df_{err} = \sum_{i=1}^{n} (r_i - 1)$ . The SS of the LOF can be derived by  $SS_{lof} = SS_{res} - SS_{err}$  and the df<sub>lof</sub> by  $df_{lof} = df_{res} - df_{err}$ . Finally, by calculating  $df_{err}$  and  $df_{err}$  and  $df_{err}$  and  $df_{err}$  are equation as above, Fishers test can be conducted for lack of fit by  $f_{df_{lof},df_{err}} = \frac{df_{slof}}{df_{err}}$ . No matter the process, if the regression is significant and LOF is not, one can state that the model includes all relevant impact factors and estimated them correctly.

Design of experiment is therefore a universally applicable statistical approach which can quickly generate predictive models using limited resources. In this work it is applied to optimize the synthesis of PBAE polymers as well as the formulation of nanoparticles with the resulting polymers.

## 4. Preparation of PBAE nanoparticles

To prepare NPs from PBAE polymers there are two commonly applied methods. The first being classical batch mixing. In this approach a solution containing the polymer and a solution containing the nucleic acid are quickly mixed using manual pipetting as mixing method. This approach is fast and quickly applicable. However, it is difficult to scale up and highly dependent on the manufacturer<sup>39</sup>. Since an approved therapeutic system needs to be able to be produced in a reproducible large scale approach this method does not seem feasible. A different approach is the application of microfluidics. Here both solutions are loaded into syringes or comparable fluid reservoirs and pumped through channels into a mixing chip<sup>40</sup>. Several different mixing chip architectures and materials have been reported in the last years. They all have in common that they produce nanoparticle dispersions of higher quality regarding size and polydispersity. Additionally, this is a continuous manufacturing process which can be easily scaled up and a

batch independent manufacturing becomes possible<sup>41</sup>. However, microfluidic mixing outcomes are highly dependent on the chip architectures<sup>42</sup>, used polymers and solvents as well as the total flow rate (TFR) and flow rate ratio (FRR) of both solutions. These factors can increase the difficulty of finding the optimal process parameters quickly. This is therefore another example in which DoE can be applied to achieve satisfactory results with limited time and resources spent<sup>43</sup>.

## 5. The human lung as barrier and target

Lung-related diseases rank among the top ten leading causes of death worldwide, according to the World Health Organization (WHO), with two of these diseases occupying the second and third positions in mortality rates in 2021. Collectively, they account for more annual deaths than ischemic heart disease, the leading global cause of death<sup>44</sup>. This makes the lungs a highly relevant target for pharmaceutical formulations. Additionally, the lungs can be targeted directly by pulmonary active pharmaceutical ingredients (API) applications which can reduce dosages and increase safety and efficacy<sup>45</sup>. However, the human lungs possess a highly branched structure, complicating successful delivery.

The respiratory track starts at the trachea, which bifurcates into two main bronchi, those branch further several times into smaller bronchi followed by bronchioles and finally the terminal bronchioles which terminate into the alveolar sacs (Figure 3). The composition and protective coating of the epithelial lining vary depending on the region of the lungs. In the bronchial epithelium, a mucus layer serves as a protective barrier, whereas in the alveoli, a surfactant layer reduces surface tension and provides additional protection<sup>46</sup>. The bronchial epithelium also contains ciliated cells which stroke in an upward direction toward the pharynx, removing old mucus and foreign substances from the airways. This forms the mucociliar clearance barrier<sup>47</sup>. In nearly all alveoli there are alveolar macrophages which play a crucial role in innate immunity by endocytosing and clearing a big proportion of all foreign substances which reach alveolar space. They thereby form an additional cellular barrier to protect the alveolar epithelium<sup>48</sup>.

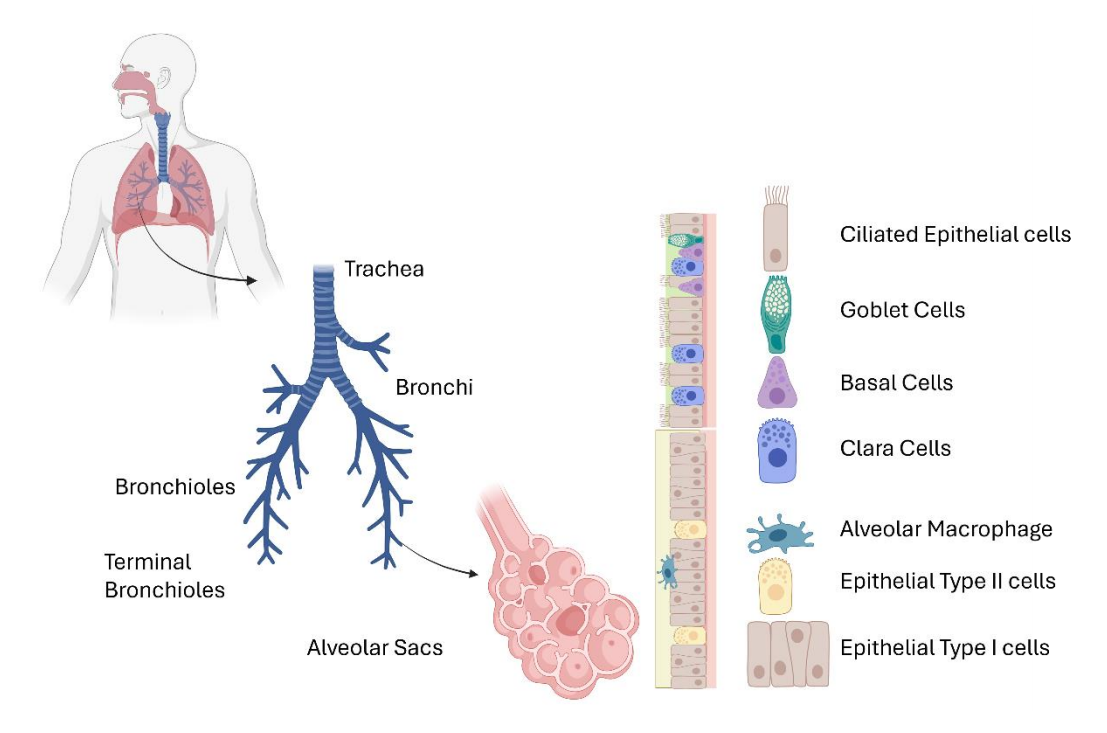


Figure 3. Structure and cellular composition of the human airways. Generated with BioRender.

Inhalation is the predominant method for delivering APIs to the lungs. There are two main formulation approaches: dry powder and liquid formulations. Both need to be converted into an inhalable aerosol of suited particle size distribution. To reach the alveolar region, it is commonly accepted that a mass median aerodynamic diameter (MMAD) of  $1-5~\mu m$  is necessary  $^{46,47}$ . To generate liquid aerosols within the desired size range there are several technologies available. Most relevant for this work are vibrating mesh nebulizers (VMN) which are often clinically used and pose several advantages over other approaches.

During the SARS-CoV-2 pandemic, many patients in critical condition, including those in comas, were unable to actively inhale, which excludes the application of many respiratory drug formulations. VMN Aerosols can be connected to lung ventilator devices and do not require the patient to actively inhale. Additionally, their nebulization process is much less shear intensive than e.g. jet nebulizers, which makes them a promising technology for nebulization of sensitive higher-order structures like polyplexes<sup>49</sup>. Concretely, VMN generate an aerosol through a micropore sized mesh connected to a piezoelectric crystal which can vibrate in the kilohertz frequency range upon connection to an electric current. The micropores are usually of conic shape. Through the vibrational back-and-forth movement of the mesh small droplets of controlled size are dispelled from the solution<sup>50</sup>. Though this process is gentler than most other aerosolization techniques, there are still challenges associated with it. Most importantly, the

mesh heat up during the nebulization process, posing a potential thermal threat to the drug solution<sup>51</sup>. Additionally, the mesh itself needs to be composed of a bioinert material to minimize the risk of drug adhesion, which could lead to disintegration, particularly in the case of polyplexes. Therefore, before applying VMN on polyplexes, it needs to be shown that the nebulization process does not alter the functional and structural integrity of the drug formulation.

## III. Design of Experiments Grants Mechanistic Insights into the Synthesis of Spermine-Containing PBAE Copolymers

This Chapter was published in ACS Applied Materials & Interfaces:

Kromer, A. P. E.; Sieber-Schafer, F.; Farfan Benito, J.; Merkel, O.M. Design of Experiments Grants Mechanistic Insights into the Synthesis of Spermine-Containing Pbae Copolymers. ACS Appl. Mater. Interfaces 2024, 16 (29), 37545–37554.

The Contribution to this chapter consisted in the draft of the experimental plan, the synthesis and analysis of the polymers as well as the data analysis and prediction.

#### 1. Abstract

Successful therapeutic delivery of siRNA with polymeric nanoparticles seems to be a promising but not vastly understood and complicated goal to achieve. Despite years of research, no polymer-based delivery system has been approved for clinical use. Polymers, as a delivery system, exhibit considerable complexity and variability, making their consistent production a challenging endeavor. However, a better understanding of the polymerization process of polymer excipients may improve the reproducibility and material quality for more efficient use in drug products. Here, we present a combination of Design of Experiment and Python-scripted data science to establish a prediction model, from which important parameters can be extracted that influence the synthesis results of poly( $\beta$ -aminoesters) (PBAEs), a common type of polymer used preclinically for nucleic acid delivery. We synthesized a library of 27 polymers, each one at different temperatures with different reaction times and educt ratios using an orthogonal central composite (CCO-) design. This design allowed a detailed characterization of factor importance and interactions using a very limited number of experiments. We characterized the polymers by analyzing the resulting composition by 1H-NMR and the size distribution by GPC measurements. To further understand the complex mechanism of block polymerization in a onepot synthesis, we developed a Python script that helps us to understand possible step-growth steps. We successfully developed and validated a predictive response surface and gathered a deeper understanding of the synthesis of polyspermine-based amphiphilic PBAEs.

#### 2. Introduction

Since the SARS-CoV-19 pandemic, the delivery of ribonucleic acid (RNA) by nanoparticles has become an ever more rapidly developing field of research. Up to now, the clinically approved drug delivery systems for RNA drugs are all based on Lipid Nanoparticles (LNP) technology <sup>52,53</sup>. However, LNPs face problems with regard to storage and stability <sup>54</sup> and encapsulate only a very low drug load of approximately 4% w/w 55. Polymeric delivery systems, such as poly(β-aminoesters) (PBAEs), that were initially designed by the group of Robert Langer in 2000 <sup>17</sup> represent a reasonable and well-studied alternative. In general, this type of polymer is easy to synthesize and in the past, end-capped homopolymers <sup>56</sup> and co-polymers <sup>20</sup> showed promising transfection on DNA<sup>57</sup>, mRNA <sup>58</sup> and siRNA <sup>59</sup> in *in vitro* and *in vivo* models<sup>20</sup>. However, synthesis of polymers, especially copolymers is hard to control <sup>60</sup> and often leads to a mixture of different molecular weight and composition species <sup>61</sup>. This is undesirable, since these factors decrease reproducibility on the one hand but govern the ability to deliver the cargo to target cells 62 and the level of toxicity 63,64 on the other hand. Furthermore, they complicate a clean correlation between species and activity. Therefore, a strategy is needed that helps control and reveal the underlying mechanisms of step-growth polymerization and help understand the process. To do so, often dozens of experiments are needed to interpret and predict all the possible influencing factors.

For many years the help of Design of Experiment (DoE) <sup>65</sup> has been used to decrease the number of necessary experiments to address a problem and to help analyze important factors as well as define predictive models that can design an accurate response surface that is used to make assumptions about future experiments and helps therefore to reduce the waste of resources and to improve sustainability of chemical synthesis.

In recent years, the combination of data science and high throughput synthesis allowed for a significant knowledge gain in the field of nanomedicine<sup>66–68</sup>. This approach can be extremely useful since it allows for optimized decision in situations, where it is rather complicated to understand the mechanistic insights of how nanocarrier design influences the delivery of cargo<sup>69</sup>. DoE can also be applied here to guide scientists in designing the experiments to achieve optimization and valuable insights into complex processes<sup>70,71</sup>. In our work, we aim to use these tools to face difficult tasks in polymeric delivery such as controlling and understanding the synthesis of amphiphilic co-polymers<sup>72</sup> and their molecular weight distribution<sup>61</sup>.

To demonstrate how data science can be used to understand and facilitate complicated scientific questions such as the controlled synthesis of block co-polymers for the encapsulation of RNA,

we synthesized spermine- and oleylamine-modified PBAE-based co-polymers using DoE to iterate over a variable space with reasonable ranges for synthesis parameters including temperature, reaction time and the ratio of monomers, that influence the characteristics of the synthesized materials <sup>73</sup>, <sup>74</sup>. Spermine was chosen as a body-own polycation to enhance RNA encapsulation efficiency and oleylamine to introduce hydrophobicity into the resulting polyplexes to facilitate the endosomal escape, demonstrated by previous work from our group<sup>75</sup>. As readout, we selected the final composition of blocks in the resulting polymer and different results from the size measurements of the polymer. For analysis we used multiple linear regression to generate a Response Surface Model and made use of different estimators that allow insights into the variables, which were most important for the prediction. To gather more information about possible structures, we designed a Python script that proposes possible polymeric compositions for Gel-Permeation-Chromatography (GPC) peak sequences. This approach was chosen to help interpret the often quite hard to analyze GPC chromatograms of co-polymers. Finally, we developed an assay that is able to mimic intracellular unpackaging of siRNA from polyplexes. This work presents a method to handle limited data effectively by using DoE and open source python libraries to facilitate the understanding and the analysis of complex synthesis mechanisms.

#### 3. Methods and Materials

#### **Materials**

Di-tert-butyl decarbonate, oleylamine, spermine, dimethylformamide (99,5% pure) and SYBR Gold Nucleic Acid Gel Stain were purchased from Fischer Scientific (Hampton, NH, USA). Ethyl trifluoroacetate, sodium chloride, heparin sodium salt 180 USP units/mg and Triton-X 100% solution were bought from Sigma Aldrich (Taufkirchen, Germany) and 1,4-butanendiol diacrylate was obtained from TCI Chemical Industry Co., LTD (Tokio, Japan). Triflouroacetic acid (99,9%, extra pure) was purchased from Acros Organics (Geel, Belgium). Methanol-d6 was obtained from Deutero (Kastellaun, Germany). Dichlormethane, methanol, ammonia, potassium permanganate, magnesium sulfate, acetone, pentane and formic acid (>99% pure) were purchased from VWR Chemicals (Ismaning, Germany).

#### **Triboc-spermine synthesis**

Tri-tert-butyl carbonyl spermine, abbreviated as tri-Boc-spermine (TBS) was synthesized as described elsewhere <sup>76</sup>. In brief, spermine (1 eq) was dissolved in methanol and stirred at -78 °C, ethyl trifluoroacetate (1 eq) was added dropwise subsequently and stirred at - 78 °C for 1 h, then 0 °C for 1 h. Without isolation, di-tert-butyl decarbonate (4 eq) was added dropwise to the solution and stirred at room temperature for 2 days. Finally, the solution was adjusted to a pH above 11 by 25% ammonia and stirred overnight to cleave the trifluoroacetamide protecting group. The mixture was then evaporated under vacuum and the residue was diluted with dichloromethane (DCM) and washed with distilled water and saturated sodium chloride aqueous solution. The DCM phase was finally dried by magnesia sulfate and concentrated to give the crude product. The crude product was purified by column chromatography (CH2CI2\MeOH\NH3, aq. 7:1:0.1, SiO2, KMnO4; Rf = 0.413). TBS was isolated and characterized by 1H nuclear magnetic resonance spectroscopy (<sup>1</sup>H-NMR).

#### Polymer synthesis and characterization

Poly-spermine-*co*-oleylamine β-aminoesters (P(SpOABAE)) were synthesized based on a previously described approach<sup>77</sup>. Briefly, TBS as hydrophilic monomer, oleylamine (OA) as hydrophobic monomer and 1,4-butanendiol diacrylate (DA) were mixed in different molar ratios in dimethylformamide (DMF) resulting in total concentrations of 300 mg/mL. Polymers were stirred at different temperatures and for different durations (Compare Table 1). After the respective reaction time, mixtures were transferred to petri dishes to evaporate the solvent. The subsequent deprotection of the polymer was carried out in a mixture of 20 ml dichloromethane (DCM) and 1 ml trifluoroacetic acid (TFA) for 100 mg polymer, followed by stirring for 2 hours

at room temperature. In the following, DCM/TFA was evaporated and the dry deprotected product was precipitated 3 times in pentane using acetone to dissolve the precipitate (Figure 1a). Supernatants were discarded and the final precipitate was dried for 2 days under vacuum (room temperature, 20 mbar). Final polymers were characterized by <sup>1</sup>H-NMR (Figure S1) and GPC. Measurements were performed with an Agilent aqueous GPC using a PSS Novema max Lux 100A followed by two PSS Novema max Lux 3000A columns. The chromatographic system and calibration standards were set up according to pre-analysis from Agilent Technologies on P(SpOABAE) polymers. Measurements were performed at 40°C in 0.1 M sodium chloride solution supplemented with 0.3% formic acid. Samples were prepared at 4 g/L and measured at a flow rate of 1 mL/min. Molar mass distributions were obtained through the Agilent WinGPC software against pullulan calibration standards in the range of 180 Da to 1450 kDa. A daisy-chain detector setup of an Agilent 1260 VWD was used followed by an Agilent 1260 GPC/SEC MDS and ending with an Agilent 1260 RID.

#### **Design of Experiment**

A Response Surface Method (RSM) <sup>78</sup> was applied using the MODDE® Pro 13.0.2 (Sartorius Data Analytics, Göttingen, Germany) software. Briefly, four critical process parameters (CPP) at three levels were chosen based on their theoretical impact on the critical quality attributes (CQA) of molecular weight and final subunit ratio. The four CPPs were i) reaction temperature (set to 80°, 100° or 120° Celsius), ii) reaction time (set to 24h, 48h or 72h), iii) initial molar OA ratio, defined as the molar ratio of primary amines from OA to the overall number of primary amines (set to 0.30; 0.55 or 0.80), and iv) the ratio between the diacrylate (DA) and the total theoretical number of primary amines (0.80; 1.00 or 1.20). A Central Composite Design for maximized Orthogonality (CCO) was chosen using a starpoint distance of 1.55<sup>79</sup>. Three center points were added to evaluate the process stability (Figure 1b+c). Statistical significance was determined by ANOVA and defined by p-values below 0.05. Predictions with 95% confidence intervals were generated based on fitted, significant RSM model terms.

#### PeakFinder software

To gather more insights into the polymerization process, a program was written using Python3 programming language (version 3.11.5). Pandas (version 2.0.3) was used for data handling. The molecular weights of the monomer units are used as input data in the code together with information about the single peak maxima (Mp), the associated component ratio (obtained from NMR spectra), an error range, a maximal iteration parameter and a boolean expression parameter if endcapping with diacrylate is possible or not. Based on this information, possible

polymer structures are calculated for each peak and the program outputs the sequence of monomer combinations that fits the data best.

#### Species isolation via spin columns

To isolate a single polymer species represented by a GPC peak, polymers were dissolved at 4 mg/mL in the mobile phase. 1 mL of solution was transferred to 30 kDa cutoff Vivaspin 6 centrifugal concentrator columns from Sartorius (Göttingen, Germany). Samples were concentrated at 8000 g for 15 min. The concentrated samples were diluted to 1 mL with fresh mobile phase. This procedure was repeated three times. Final samples were measured using the before mentioned GPC method.

#### Particle formation with siRNA

Polymers were dissolved in cell culture grade DMSO at a concentration of 25 mg/mL. Nanoparticles were prepared at a ratio of protonated amines in the polymer to negatively charged phosphates in the siRNA backbone (N/P Ratio) of 10. Polymer stocks and siRNA (IDT, Leuven, Belgium) were diluted in 10 mM Hepes Buffer pH 5.4 to equal volumes before mixing. Mixing was done using an Integra Voyager 125 µL pipette (Integra Biosciences, Zizers, Switzerland), resulting in final concentrations of 500 nM siRNA. After mixing, particles were incubated for 90 minutes at room temperature to allow proper particle formation. The hydrodynamic diameter (DH) and polydispersity index (PDI) of the obtained nanoparticles were determined by dynamic light scattering. Therefore, a Zetasizer Ultra series (Malvern Instruments, U.K.) was used running 3 measurements per sample at a backscatter angle of 173°.

#### **Stability**

The stability of the resulting nanoparticles was evaluated by a modified polyanion competition assay<sup>80</sup>. Briefly, differently concentrated mixtures of Triton-X and heparin were applied to release the siRNA from the nanoparticles. In a black 384-well plate, 10 µL nanoparticle suspension was mixed with 20 µL of stress solution with the respective concentration level. Seven different concentrations plus a blank were used per nanoparticle suspension. After adding the stress solutions, plates were sealed to avoid evaporation and incubated at 37°C at 150 rpm for 1h. Afterwards 5 µL of a 4x SYBR Gold dye was added to the mixture and incubated for 5 minutes in the dark. Finally, the fluorescence was measured using a TECAN Spark plate reader (TECAN, Männedorf, Switzerland) plate reader at 492 nm excitation and 537 nm emission wavelength. Using the GraphPad Prism5 2007 Software, a nonlinear fit was performed to calculate the EC50 values of each polymer relative to the maximum released siRNA in each sample.

#### 4. Results and Discussion

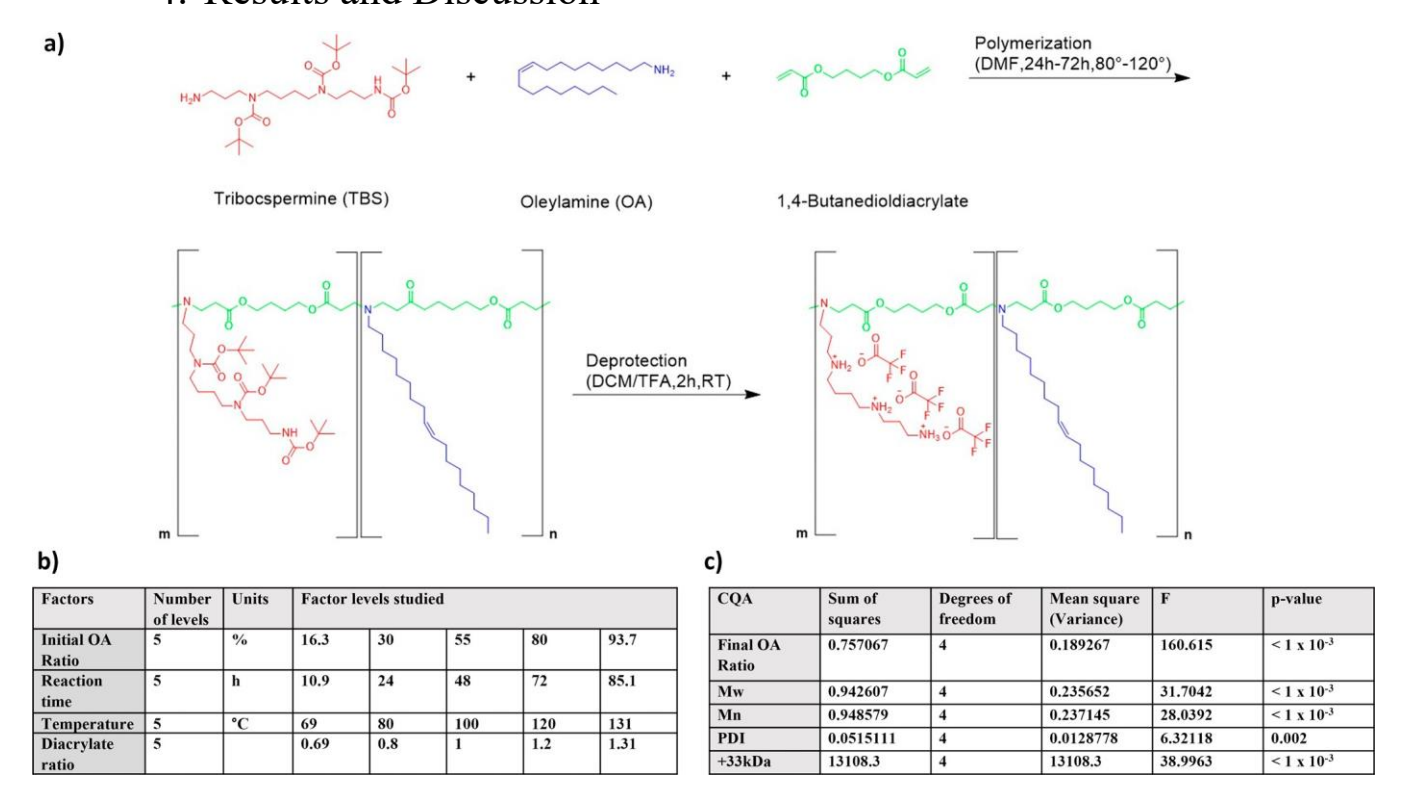


**Figure 1.** (a) Overview of the applied synthesis for the used poly( $\beta$ -aminoesters). Polymerization was carried out using different time points, temperatures, and component ratios. (b) Factors used for the CCO design and (c) CQAs selected as a readout together with the data from ANOVA.

#### Controlling the synthesis via DoE

The two most important CQAs controlling the nucleic acid delivery performance of a polymer are the molecular weight distribution <sup>63,64</sup> and the composition of the polymer itself <sup>81</sup>. In case of amphiphilic spermine-modified PBAEs, previous studies showed that the ratio of hydrophobic side chains <sup>75</sup> plays a major role in the transfection efficiency of PBAE copolymers <sup>77</sup>. Additionally, it was shown for numerous PBAEs that the molecular weight plays vital functions in governing the performance as well as toxicity <sup>82</sup>. Therefore, the main goal of this study was to establish a synthesis route which would allow the precise prediction and control over the final constitution of the P(SpOABAE) polymers. By using the CCO, the design space, which was investigated, was maximized and by investigating 5 levels for each factor (Figure 1b) the prediction strength was increased (Table 1).

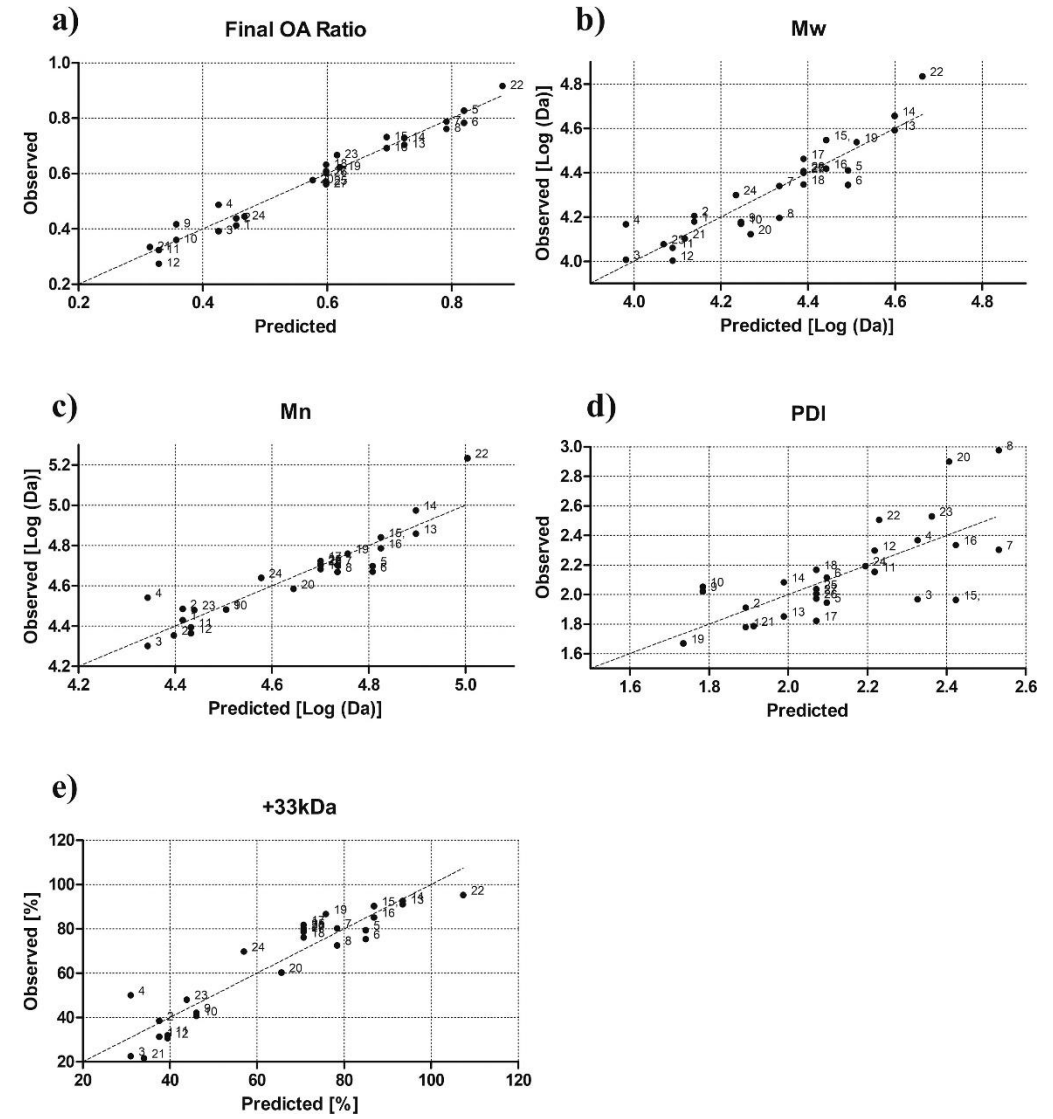
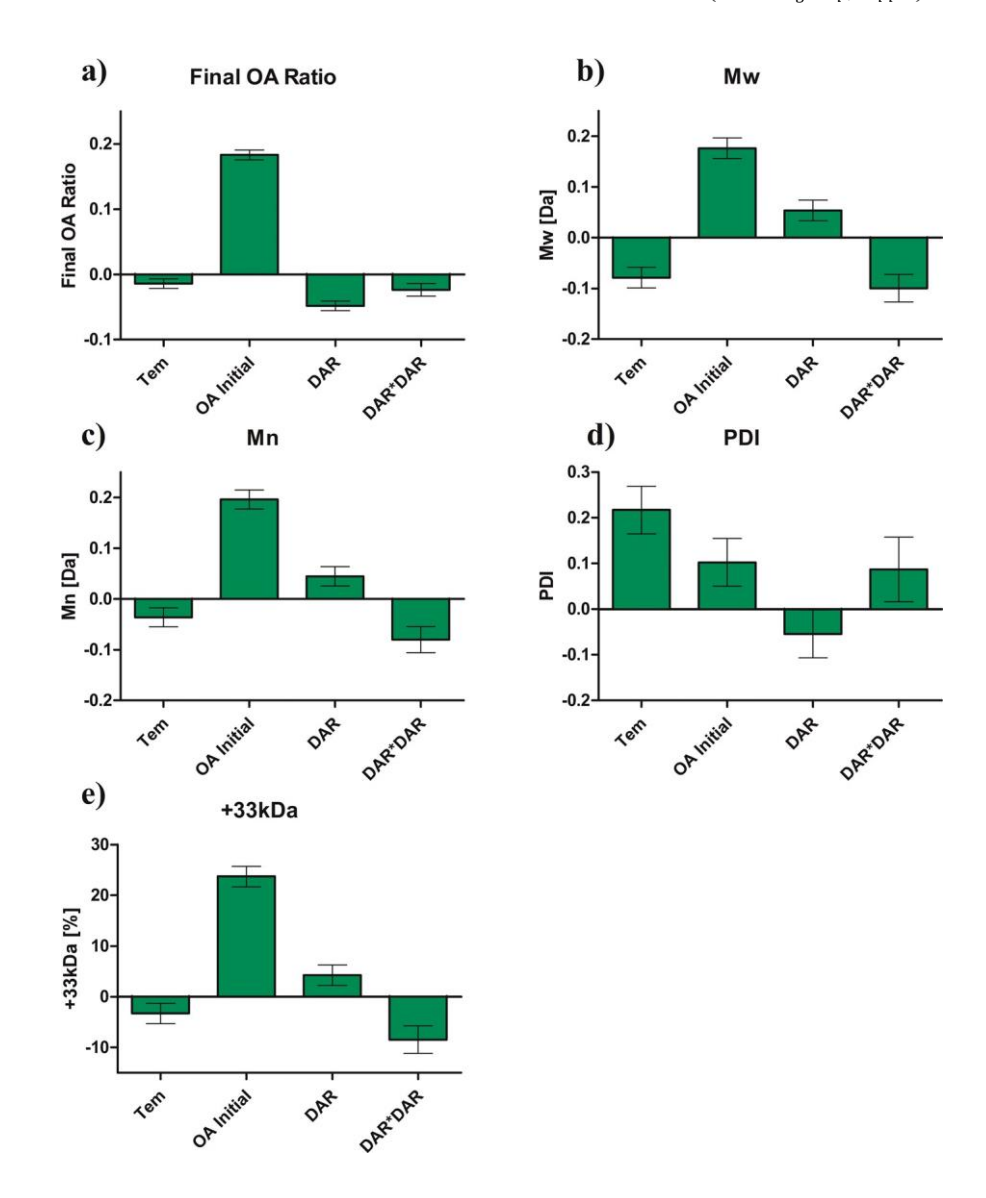


Figure 2. Observed vs predicted plot for (a) final OA ratio (R2 = 0.97), (b) Mw (R2 = 0.85), (c) Mn (R2 = 0.84), (d) PDI (R2 = 0.53), and (e) >33 kDa (R2 = 0.88) for the CCO-design generated with 27 polymers.

After performing the synthesis and analysis, the responses (Figure 1c) were fitted using multiple linear regression. For the CQA final OA ratio, a strong regression of  $R_2 = 0.968$  and a high validity of  $Q_2 = 0.948$  were found indicating a strong model (Figures 2a and S2). In the next step, the factors, which had been the most relevant for the model fit were investigated. By choosing a CCO, the factor strengths for linear as well as quadratic model terms, together with interactions between different CPPs was estimated. For the final OA ratio, only three model terms showed a p-value below 0.05 and were deemed significant (Figure S7). Unsurprisingly, the most relevant CPP was the initial OA ratio with a scaled and centered coefficient of 18.3%. Also, according to expectations, the temperature and reaction time did not impact the final OA ratio significantly. Surprisingly, the two other significant CPPs were the linear and quadratic

diacrylate ratio with coefficients of -4.8% and -2.6% (Figures 3a and S7). Although they were less relevant, it is still unexpected that this CPP can influence the final OA ratio. A potential reason for this observation might be the calculation approach chosen to determine the final OA ratio (eq.1). In this approach, the diacrylate backbone is taken into account in the formula and thereby naturally impacts the final results.

$$OA\ Ratio = \frac{I_{(0.9ppm)}}{n_{H(terminal\ group, 0.9\ ppm)}} x \frac{n_{H(backbone, 4.2ppm)}}{I_{(4.2ppm)} - \left(n_{H(terminal\ group, 0.9\ ppm)}\right) x \frac{I_{(0.9ppm)}}{n_{H(terminal\ group, 0.9\ ppm)}} \quad \text{(eq. 1)}$$



**Figure 3.** Model coefficients for (a) final OA ratio ( $R_2 = 0.97$ ;  $Q_2 = 0.95$ ), (b)  $M_w(R_2 = 0.85; Q_2 = 0.77)$ , (c) Mb ( $R_2 = 0.84$ ;  $Q_2 = 0.75$ ), (d) PDI ( $R_2 = 0.53$ ;  $Q_2 = 0.29$ ), and (e) >33 kDa ( $R_2 = 0.88$ ;  $Q_2 = 0.81$ ) for the CCO-design generated with 27 polymers.

In contrast to other polymerization mechanisms, the step-growth Michael-addition did not lead to a single polymer species but rather a mixture of several distinctive peaks. This finding will be further discussed below. To evaluate the presence of unreacted monomers the, numerical percentage of species below 2,000 Da (<2 kDa) was determined (Table 1). Since the DoE can only interpret discrete numerical values, a way to make our library "interpretable" for the DoE algorithms had to be found. Therefore, several specific CQAs rather than a single molar mass distribution were added. To start, the overall Mn, Mw, PDI of the polymer as well as the numerical percentage of the polymer species above 33,000 Da (>33 kDa) were analyzed and introduced. For each CQA except for the PDI, a model with a regression above  $R_2 = 0.84$  and a cross-validation value above  $Q_2 = 0.75$  were found (Figure 2 b-e, 3 b-e, S8-S11). This outcome confirmed that the model was able to understand the synthesis and which CPPs govern the polymerization mechanisms. Surprisingly, the main factor controlling the three responses of Mn, Mw and >33 kDa was the OA ratio. Since the PDI of polymers is calculated by dividing the Mw by the Mn, this CQA is susceptible to error propagation. This problem is reflected in higher scatters in the observed vs predicted plot (Figure 2 d) and higher standard deviations in the coefficient plot (Figure 3 d).

Reaction time was not significant for any of the responses and temperature only played a minor role on the Mn.

#### **Understanding key mechanisms**

The initial hypothesis was that the molecular weight of the polymers would be mainly governed by the reaction time and temperature following common consensus <sup>83</sup>. However, the presented data suggest a more complex mechanism. Since the analyses showed that the main factor governing the large >33 kDa species was the OA ratio, it was concluded that the reaction kinetics of OA was faster than the kinetics of the TBS subunits. A faster reaction of hydrophobic subunits was already reported in literature <sup>60</sup>. However, it was observed that the maximum size of the >33 kDa species correlated with the OA ratio as well (Figure 3e). This could not be explained with faster kinetics alone. Analyzing all GPC data more extensively showed that all polymers had a characteristic sequence in which the peaks occurred (Figure 4a). This was explained by the mechanism of step-growth polymerization.

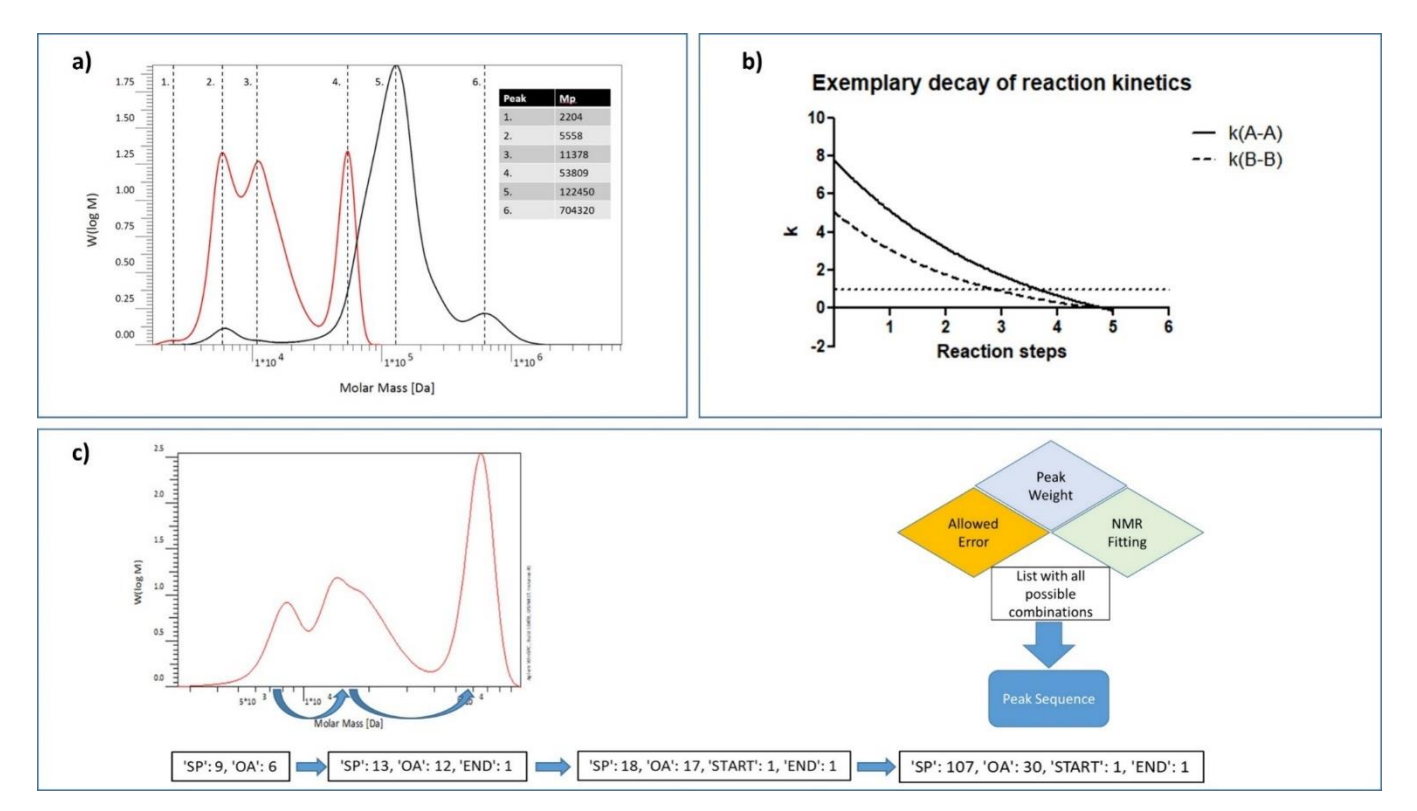


**Figure 4.** (a) Exemplary GPC peaks and  $M_p$  weights of polymers 3 (red) and 22 (black) in an overlay molar mass distribution. (b) Exemplary decay of different reaction kinetics as a function of already occurred reaction steps. (c) The PeakIdentifier tries to give the researcher an assumption, starting from the molecular weight distribution in GPC data, about peak sequences. On the right, a schematic overview illustrates how the PeakIdentifier attempts to match individual peaks and the peak sequence using the available data. At the bottom, an example sequence proposed by the PeakIdentifier for the molecular weight distribution above is shown. The units and the corresponding numbers suggest the peak compositions that matches the data best.

In step-growth polymerization, monomers undergo simultaneous parallel reactions to form dimers, which subsequently engage in further parallel reactions to produce tetramers and subsequent oligomeric species <sup>29</sup>. Interestingly, in co-polymers the same mechanism applies with the difference that three kinetics are occurring in parallel. The kinetics of two building blocks of the same type reacting with each other (kA-A, kB-B) and the kinetics of two different building blocks reacting with each other (kA-B, kB-A). Additionally, each reaction slows down exponentially, with the number of reactions (r) that have already occurred [25]. With this behavior, the following relation could be drawn:

$$kA-A (r=1) > kA-A (r=2) > ... > kA-A (r=n)$$
 (eq.2)  
 $kB-B (r=1) > kB-B (r=2) > ... > kB-B (r=n)$  (eq.3)  
 $kA-B (r=1) > kA-B (r=2) > ... > kA-B (r=n)$  (eq.4)  
 $kB-A (r=1) > kB-A (r=2) > ... > kB-A (r=n)$  (eq.5)

Together with the finding that the OA homopolymerization kinetics are faster than TBS homopolymerization kinetics, a new hypothesis was established.

It was proposed that the reaction reaches its thermodynamic equilibrium after a certain amount of steps after which the reaction kinetics decrease to a level where statistically no more reactions occur, for example, where a certain threshold was reached. How many reactions it takes, for example, and how long the polymers become before the threshold is reached is hence governed by the initially faster kinetics (kA-A). In this case the kinetics and initial amount of OA (Figure 4b).

Although the relationship between the >33 kDa species and the initial OA content may be explained by this hypothesis, one needs to take into account that in theory only one single species of varying size should have arisen from each synthesis. The fact that one can simultaneously observe all different stages of the step-growth polymerization underlined the reversibility of the Michael-addition (Figure 4a) <sup>84</sup>.

$$(A) + (B) \rightleftharpoons (AB) \rightleftharpoons (ABAB) \rightleftharpoons (ABABABAB)$$
 (eq.6)

The reversibility indicated that all stages of the step-growth synthesis are in equilibrium with each other. The equilibrium that the reactions reaches (eq.6) is, according to these findings, governed by the ratio between faster reacting OA and slower reacting TBS (Figure 4b).

A deeper investigation of the impact of the diacrylate (Figure 3b+c and 5b+c) showed that the Carother's equation <sup>85</sup> also held true for these polymers, showcasing that a diacrylate ratio of 1.0 leads to the largest polymers.

To incorporate the new hypothesis into the data set, an in-house software package was written. The software aimed to mimic the block-copolymer step-growth reaction, which was expected in this system. Therefore, the absolute Mw of single building blocks was combined together with an error term, to allow variance. This step was repeated for every peak in the chromatogram, which led to a list of all possible peak sequences. Finally, peak sequences were matched with the corresponding peak-weight and the polymer block composition data obtained from NMR to match the most suitable peak sequences. The software then outputs the peak sequence with the best match. To increase the likelihood that the sequence matched the data, the program was constrained to select only sequences that assumed a growth in single building blocks. Additionally, end capping with diacrylate was only possible when there was an excess in the amount of diacrylate used for synthesis.

It was important to note that the function did not apply any further physicochemical steps to

calculate a matching sequence and the results were calculated from the obtained data. Therefore, high data quality was a major assumption of the program.

Figure 4c shows an example for the PeakIdentifier from sample number 10. The error range was set to 15 % to allow for the absolute combined monomers to vary with this value from the proposed combination, and the NMR ratio was set to 38.42 [%]. The PeakIdentifier suggested a scenario where Oleylamine (OA) and Triboc-spermine (TBS) react with equal probability. This assumption was based on the understanding that although OA reacts more quickly (due to faster kinetics), TBS is available in greater concentration within the reaction mixture, balancing the reaction likelihood between the two. The last peak observed might be the result of a subsequent synthesis reaction, where the higher concentration of TBS in the sample prompts the oligomers to undergo a reaction. What was shown clearly, is that the PeakIdentifier explained possible step-growth reactions in combination with different kinetics. It has to be mentioned that the PeakIdentifier provided a range of possibilities, but since the program worked with absolute data one had to make sure to precisely select a reasonable error range. To validate the software (Figure S12), two single peak fractions were isolated using spin columns. To verify a successful isolation, GPC was measured again (Figure S13). The NMR results from the isolated fractions were compared to the PeakIdentifier results. From the NMR data for polymer 16, an 89.29% OA ratio was observed in the isolated peak at 67,750 Da and for polymer 17, 62.0% OA monomer was found in the isolated peak at 62,877 Da. The PeakIdentifier calculated 124 OA units to 9 Spermine units, which corresponds to a ratio of 93.2% for peak 16 and 75 OA units to 46 Spermine units, which is precisely 62.0% for peak 17. We consider a delta in the estimation and the real ratio of under 5% as successful, which was satisfied for both polymers tested (3.91% for 16 and 0 for 17). Based on this example it was shown that the PeakIdentifier allows for a quite precise estimation of possible polymer fractions within this synthesis.

Another observation that was made was the presence of a side product appearing around 8 ppm in the NMR (Figure S14). However, a correlation between the intensity of the NMR peaks of this impurity and the temperature could be shown. Furthermore did the DoE approach allow us to find the optimal setpoints to avoid the generation of these side products in the first place (Figure S15). This highlights how DoE did not only improve the understanding of the stepgrowth synthesis process but also how the most robust setpoints could be identified to achieve the best results.

Interestingly, within the selected range, reaction time did not show any influence on the readout parameters. This result could be caused by the fact that the equilibrium of the polymerization

process was already in a stable state after a short period of time and was not further influenced by longer reactions. Despite the fact that high temperature led to the mentioned side products and a possible reversibility in Michael addition reaction, it did surprisingly not show any influence on the polymer size parameters.

#### Prediction

After the fitting of the model, a response surface for the entire design space was generated (Figure 5a-e). To validate the model, three different polymers with varying final OA Ratios of 40%, 50% and 60% (Table S1) were predicted. The reasoning behind these setpoints was to spread through the design space as far as possible to validate a wide range. Additionally, the predictions for the molecular weights were validated with the same polymers. Having gained a deeper understanding of the complexity of our polymerization process, it was all the more surprising how well the model did not just fit the already generated data but also predicted the validation data (Figure 6 and Table S1).

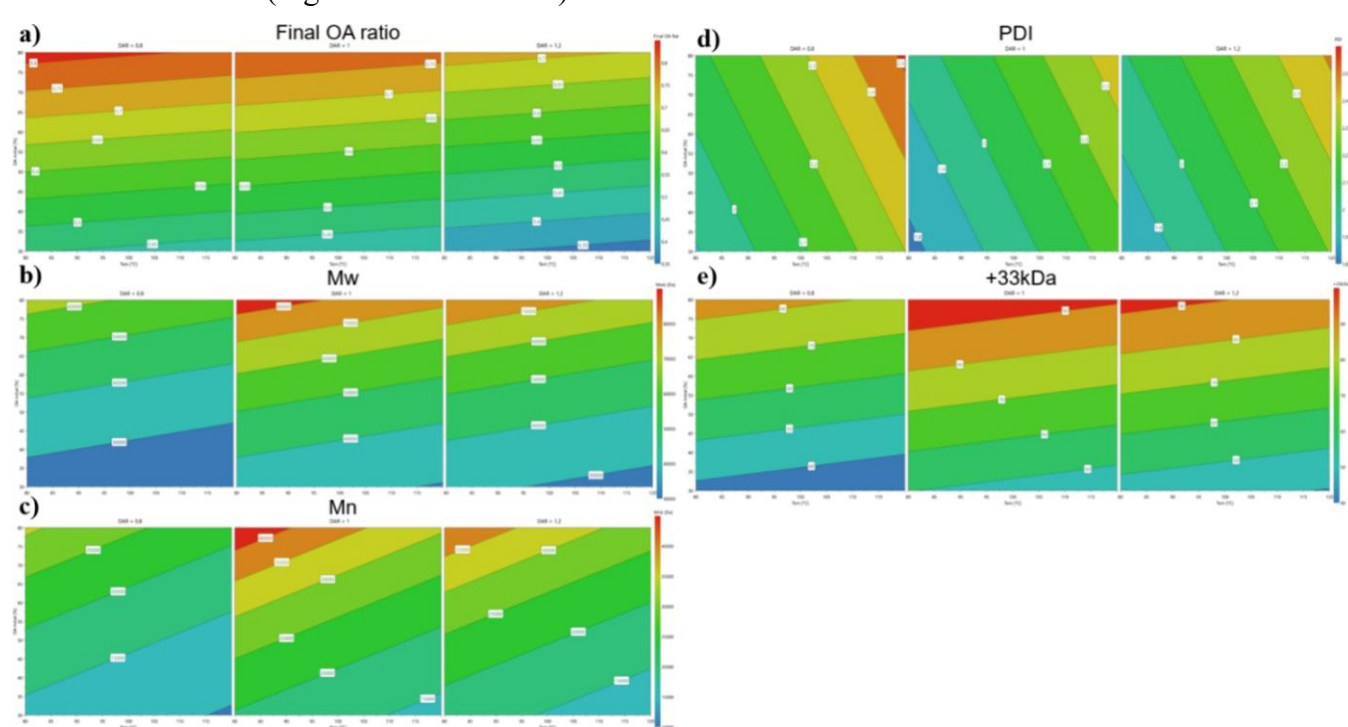
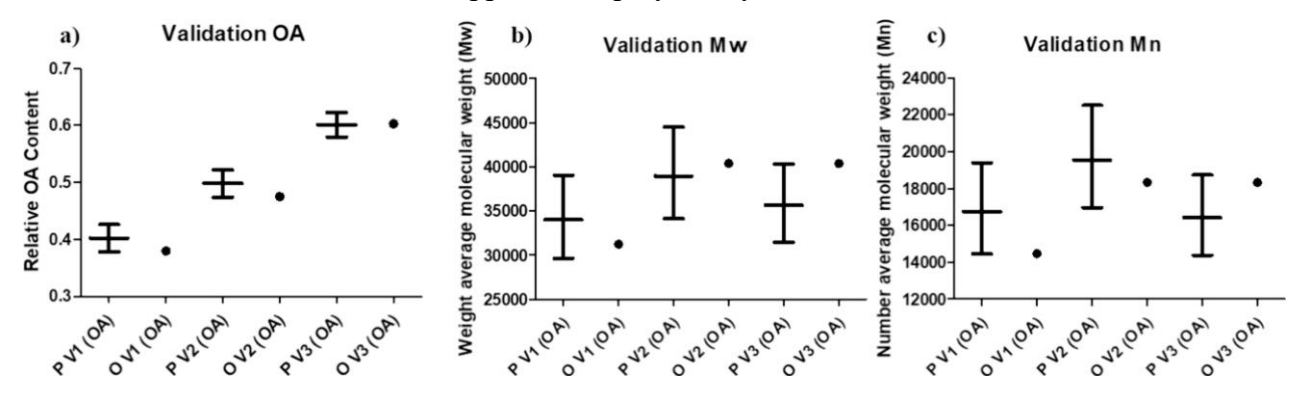


Figure 5. Three-dimensional plot of the response surface of (a) the final OA ratio, (b)  $M_{\rm w}$ , (c)  $M_{\rm n}$ , (d) PDI, and (e) >33 kDa model fitted from the CCO-design of 27 polymers showing the impact of the diacrylate ratio (left, 0.9; center, 1.0; right, 1.2), initial molar OA ratio, and temperature.

The model was capable of accurately predicting the final OA ratio as well as the molecular weight of the respective polymers. This dataset confirmed that with DoE even highly complex mechanisms such as the showcased co-polymerization mechanism can be understood and controlled, allowing a precise manufacturing of new desired polymers. With this approach it is

possible to synthesize any desired polymer in the design space without any further trial and error studies, as it is the common approach in polymer synthesis <sup>86</sup>.



**Figure 6.** Prediction (P, error bars) and observed values (dots) for the validation of (a) the OA ratios, (b)  $M_w$  values, and (c)  $M_n$  values of three validation polymers.

#### **Stability**

As previously shown <sup>75,77</sup>, amphiphilic PBAE-based spermine copolymers can mediate highly effective gene silencing when they are used for siRNA formulation and delivery. To confirm that the entire design space has relevance to subsequent performance tests, it was investigated if all polymers formed nanoparticles, encapsulated and finally released siRNA. As shown in Figure S16 and S17, all polymers were able to form stable particles, which encapsulated the entire amount of the provided siRNA. Through the new stability assay, assumptions about the strength of the intra-particular forces stabilizing the particles were additionally made. This allowed the investigation of which polymers would form the most and least stable particles. Polymer 5 and 6 formed the most stable particles and polymer 16 formed the least stable particles. The strongest correlations for the stability of the particles were found for the synthesis temperature (Figure 7b), DA ratio (Figure 7d), and the PDI of the resulting nanoparticles (Figure 7f). More precisely did a lower DA ratio and a lower temperature during the synthesis lead to more stable nanoparticles. For the synthesis time (Figure 7a) and the initial OA ratio (Figure 7c), no clear trends could be found. Similarly, the hydrodynamic diameter of the nanoparticles did not show a clear trend. Polymer 14 formed much larger particles than all other polymers but showed comparable stability (Figure S16+S17). Additionally, the difference in deviation of the EC 50 values showed a relation to the synthesis parameters (Figure 7b,d), indicating controllability by carefully choosing the proper settings. These parameters can become very important for subsequent in vitro and in vivo studies. Further analysis showed that the stability correlated with the PDI of the nanoparticles, indicating that less homogenous particles are harder to break up (Figure 7f).

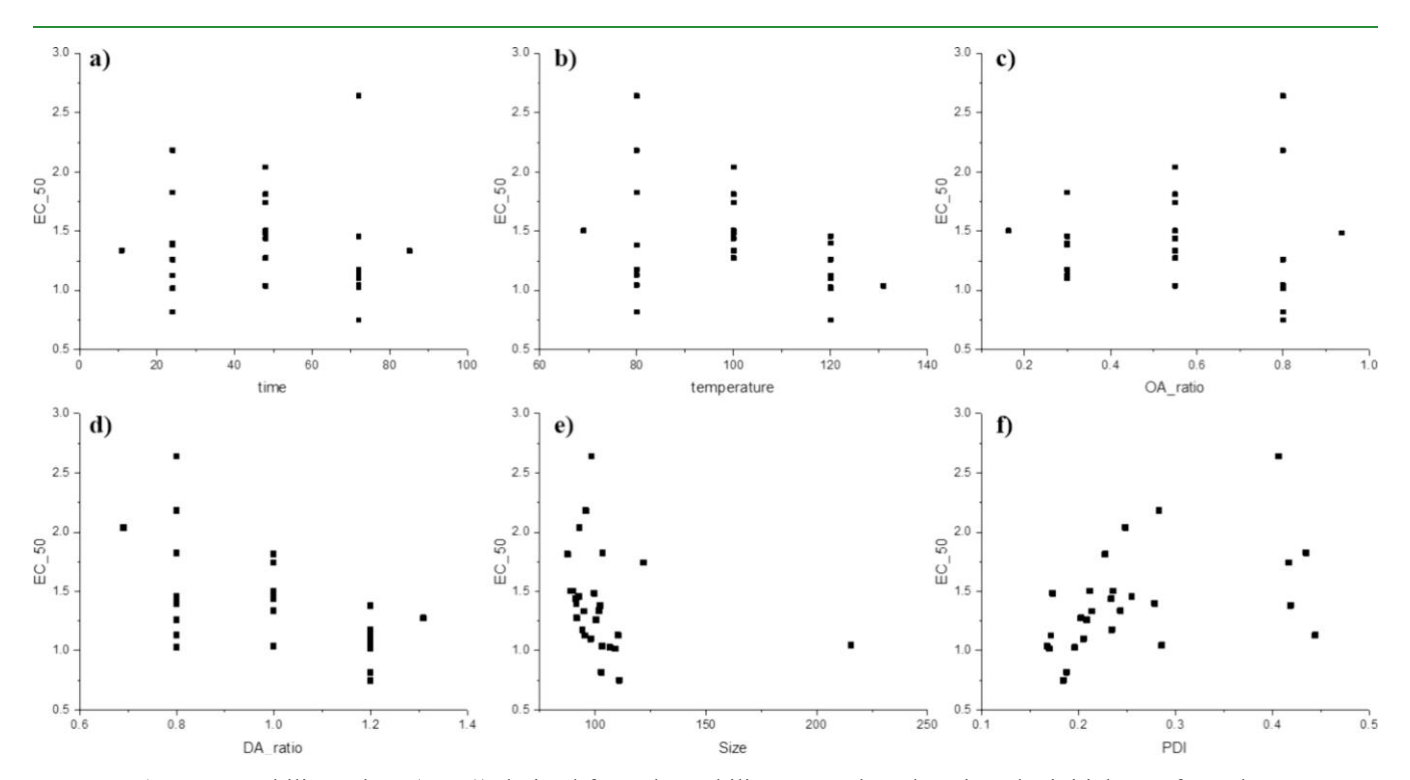


**Figure 7.** Stability values (EC50) derived from the stability assay plotted against the initial CPP from the CCO-design being (a) the time of reaction, (b) the temperature of the reaction, (c) the initial OA ratio, and (d) the DA ratio as well as the DLS data with (e) the hydrodynamic diameter of the tested particles and (f) the PDI of the tested particles.

#### 5. Conclusion

This study highlighted the value of DoE as a tool to gain a deeper mechanistic understanding of PBAE-based copolymer synthesis. Besides the revelation of key parameters controlling the synthesis of P(SpOABAE), a model that accurately predicts the outcome of a synthesis approach was established. According to our knowledge, this is the first report of a model that is capable of predicting the molecular weight as well as building block ratios of copolymers. In combination with PeakIdentifier software, a detailed picture of any synthesized copolymer can be generated. As a deep understanding of the used polymers is the first step for any scientific study, we are confident that these findings will prove valuable for other scientists in the search for more controlled material generation.

## 6. Acknowledgements

This work was supported by ERC-2022-COG-101088587 to O.M.M. and by the German Federal Ministry of Education and Research (BMBF) in the framework of the Cluster4Future program (Cluster for Nucleic Acid Therapeutics Munich, CNATM, Project ID: 03ZU1201AA). Graphics were partially generated using BioRender.

## 7. Supporting Information

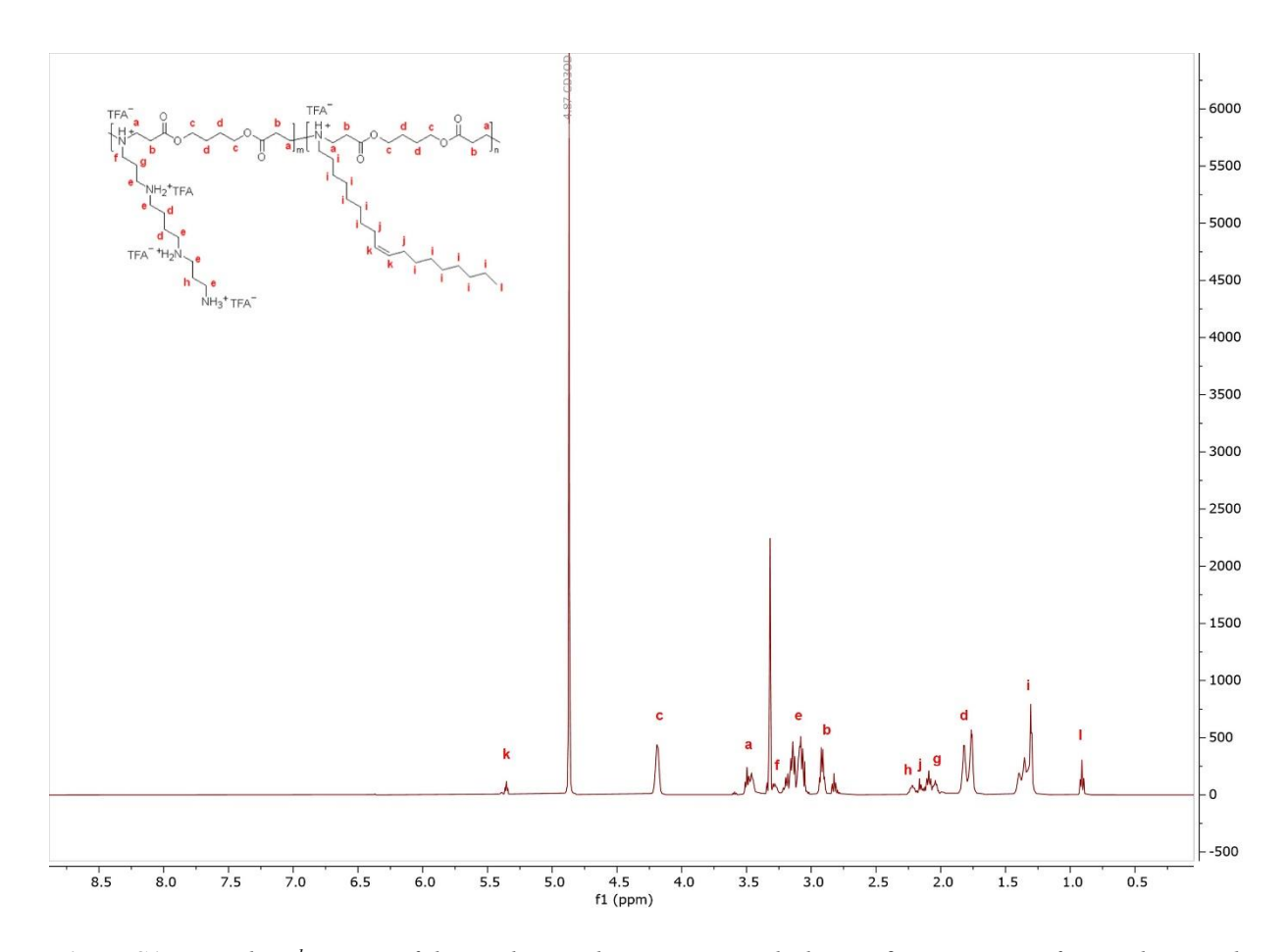


Figure S1. Exemplary <sup>1</sup>H-NMR of the resulting Poly-spermine-co-oleylamine  $\beta$ -aminoesters after synthesis and purification

Final OA Ratio	DF	SS	MS (variance)	F	p	SD
Total	26	9.53312	0.366658			
Constant	1	8.75131	8.75131			
Total corrected	25	0.781813	0.0312725			0.17684
Regression	4	0.757067	0.189267	160.615	0.000	0.435048
Residual	21	0.0247461	0.00117839			0.034327
						6
I I CE:	20	0.0220407	0.00110703	1 40717	0.570	0.024500
Lack of Fit	20	0.0239407	0.00119703	1.48616	0.578	0.034598
(Model error)						
Pure error	1		0.000805451			0.028380
		1				5
(Replicate error)						
,						
	N=26	<i>Q2</i> =	0.948	Cond. no.	2.832	
		_		=		
	DF = 21	<i>R2</i> =	0.968	RSD =	0.0343 3	
	21	R2 adj. =	- 0.062		5	
		K2 aaj. –	· 0.902			

Figure S2. ANOVA table of the final OA Ratio from the CCO-design of 27 polymers.

Final OA Ratio	Coeff. SC	Std. Err.	P	Conf. int(±)
Constant	0.600624	0.0107169	2.34777e-24	0.022287
Tmp	- 0.0141401	0.0075296 2	0.074348	0.0156587
OA Initial	0.183216	0.0075296 1	7.19313e-17	0.0156587
DAR	-0.0481132	0.0075296 2	2.46714e-06	0.0156587
DAR*DAR	- 0.0255963	0.0104307	0.0229448	0.0216919

$$N = 26$$
  $Q2 = 0.948$   $Cond. no. = 2.832$   $DF = 21$   $R2 = 0.968$   $RSD = 0.03433$   $R2 \ adj. = 0.962$   $Confidence 0.95$ 

Figure S3. Coefficient table (Scaled and Centered) for final OA-Ratio model from the fitted CCO-design.

Mwb~	DF	SS	MS (variance)	F	p	SD
Total	27	582.11	21.5596			
Constant	1	581.004	581.004			
Total corrected	26	1.10613	0.0425434			0.206261
Regression	4	0.942607	0.235652	31.7042	0.000	0.48544
Residual	22	0.163522	0.00743283			0.0862139
Lack of Fit	20	0.16349	0.0081745	506.302	0.002	0.0904129
(Model error)						
Pure error	2	3.2291e-	1.61455e-05			0.0040181
		05				5
(Replicate error)						
,						
	N = 27	<i>O2</i> =	0.768	Cond. no.	2.731	
		٤		=		
	DF =	R2 =	0.852	RSD =	0.0862	
	22	na :	0.007		1	
		<i>R2 adj.</i> =	÷ 0.825			

Figure S4. ANOVA table of the Mw from the CCO-design of 27 polymers.

Mnb~	DF	SS	MS (variance)	F	p	SD
Total	27	503.413	18.6449			
Constant	1	502.278	502.278			
Total corrected	26	1.13465	0.0436402			0.208902
Regression	4	0.948579	0.237145	28.0392	0.000	0.486975
Residual	22	0.186067	0.0084576			0.0919652
Lack of Fit	20	0.186026	0.00930132	456.658	0.002	0.0964434
(Model error)						
Pure error	2	4.07365e-	2.03682e-05			0.0045131
		05				2
(Replicate error)						
,						
	N = 27	<i>Q2</i> =	= 0.747	Cond. no.	2.731	
				=		
	DF = 22	<i>R2</i> =	= 0.836	RSD =	0.0919 7	
	22	R2 adj. =	- 0 806		/	
		K2 aaj. =	- 0.000			

Figure S5. ANOVA table of the Mn from the CCO-design of 27 polymers.

PDI~	DF	SS	MS (variance)	F	p	SD
Total	27	2.96082	0.10966			
Constant	1	2.86449	2.86449			
Total corrected	26	0.0963304	0.00370502			0.0608688
Regression	4	0.0515111	0.0128778	6.32118	0.002	0.11348
Residual	22	0.0448193	0.00203724			0.0451358
Lack of Fit	20	0.0447258	0.00223629	47.8424	0.021	0.0472894
(Model error)						
Pure error	2		4.67429e-05			0.0068368
-		05				8
(Replicate error)						
	N = 27	Q2 =	= 0.288	Cond. no.	2.731	
				=		
	DF = 22	<i>R2</i> =	0.535	RSD =	0.0451 4	
	22	R2 adj. =	- 0.450		7	
		<b>κ</b> ∠ aaj. –	- U.43U			

Figure S6. ANOVA table of the PDI from the CCO-design of 27 polymers.

>33 kDa	DF	SS	MS (variance)	F	p	SD		
Total	27	126153	4672.33					
Constant	1	111196	111196					
Total corrected	26	14957.1	575.273			23.9848		
Regression	4	13108.3	3277.08	38.9963	0.00	57.2458		
Residual	22	1848.78	84.0356			9.16709		
Lack of Fit	20	1847.51	92.3754	144.963	<b>0.00</b> 7	9.61121		
(Model error)								
Pure error	2	1.27447	0.637236			0.79827 1		
(Replicate error)								
	N=27	Q2 =	0.806	Cond. no.	2.73			
	DF = 22		0.876	RSD = 9.16				
		R2 adj.						

Figure S7. ANOVA table of the >33 kDa fraction from the CCO-design of 27 polymers.

Mwb~	Coeff. SC	Std. Err.	P	Conf. int(±)
Constant	4.70064	0.025692 5	1.65088e-36	0.0532832
Tem	- 0.0362279	0.018910 6	0.0684845	0.0392185
OA Initial	0.196177	0.018910 6	6.16452e-10	0.0392185
DAR	0.0447507	0.018910 6	0.0271844	0.0392185
DAR*DAR	- 0.0802959	0.025482 8	0.00463685	0.0528483

$$N = 27$$
  $Q2 = 0.768$   $Cond. no. = 2.731$   $DF = 22$   $R2 = 0.852$   $RSD = 0.08621$   $R2 \ adj. = 0.825$   $Confidence 0.95$ 

Figure S8. Coefficient table (Scaled and Centered) for Mw model from the fitted CCO-design.

Mnb~	Coeff. SC	Std. Err.	P	Conf. int(±)
Constant	4.38982	0.027406 4	3.07204e-35	0.0568377
Tem	- 0.0786417	0.020172	0.000772216	0.0418347
OA Initial	0.176359	0.020172 2	1.31122e-08	0.0418347
DAR	0.0536849	0.020172	0.0142611	0.0418347
DAR*DAR	- 0.0996573	0.027182 7	0.00135652	0.0563738

$$N = 27$$
  $Q2 = 0.747$  Cond. no. = 2.731  
 $DF = 22$   $R2 = 0.836$   $RSD = 0.09197$   
 $R2 \ adj. = 0.806$  Confidence 0.95

Figure S9. Coefficient table (Scaled and Centered) for Mn model from the fitted CCO-design.

PDI~	Coeff. SC	Std. Err.	P	Conf. int(±)
Constant	0.310812	0.0134508	6.38448e-17	0.0278955
Tem	0.0424165	0.0099003 5	0.000301253	0.0205322
OA Initial	0.0198192	0.0099003 5	0.0577805	0.0205322
DAR	- 0.00893745	0.0099003 5	0.376442	0.0205322
DAR*DAR	0.0193637	0.0133411	0.160772	0.0276678

$$N = 27$$
  $Q2 = 0.288$   $Cond. no. = 2.731$   $DF = 22$   $R2 = 0.535$   $RSD = 0.04514$   $R2 \ adj. = 0.450$   $Confidence \ 0.95$ 

Figure S10. Coefficient table (Scaled and Centered) for PDI model from the fitted CCO-design.

>33 kDa	Coeff. SC	Std. Err.	P	Conf. int(±)
Constant	70.7029	2.73187	5.74094e-18	5.66558
Tem	-3.29656	2.01076	0.115342	4.17009
OA Initial	23.7096	2.01076	5.56369e-11	4.17009
DAR	4.24879	2.01076	0.0461756	4.17009
DAR*DAR	-8.48071	2.70957	0.00487188	5.61934

$$N = 27$$
  $Q2 = 0.806$   $Cond. no. = 2.731$   $DF = 22$   $R2 = 0.876$   $RSD = 9.167$   $R2 \ adj. = 0.854$   $Confidence \ 0.95$ 

Figure S11. Coefficient table (Scaled and Centered) for >33 kDa model from the fitted CCO-design.

# Pseudocode of the function:

# Algorithm PeadIdentifier

Input: chromatogram\_peaks, mw\_building\_blocks, error\_term, peak\_weights, NMR\_data,end-cap bool

Output: best\_matching\_sequence

- 1. Initialize all sequences as an empty list
- 2. For each peak in chromatogram peaks do:
  - 2.1 Calculate adjusted mw = mw building blocks + error term + end-cap bool
  - 2.2 Generate all possible sequences for the peak using adjusted mw
  - 2.3 Add generated sequences to all sequences
- 3. Initialize best match score as negative infinity
- 4. Initialize best matching sequence as None
- 5. For each sequence in all sequences do:
  - 5.1 Calculate match score for sequence based on peak weights and NMR data
  - 5.2 If match score > best match score then:
    - 5.2.1 Update best match score to match score
    - 5.2.2 Update best matching sequence to sequence

#### Return best matching sequence

**Figure S12.** PeakIdentifier Pseudo code explaining the function of the PeakIdentifier. The code is used to match GPC and NMR data to the chromatogram and is expected to help identifying peaks and peak sequences of stepgrowth polymerization products.

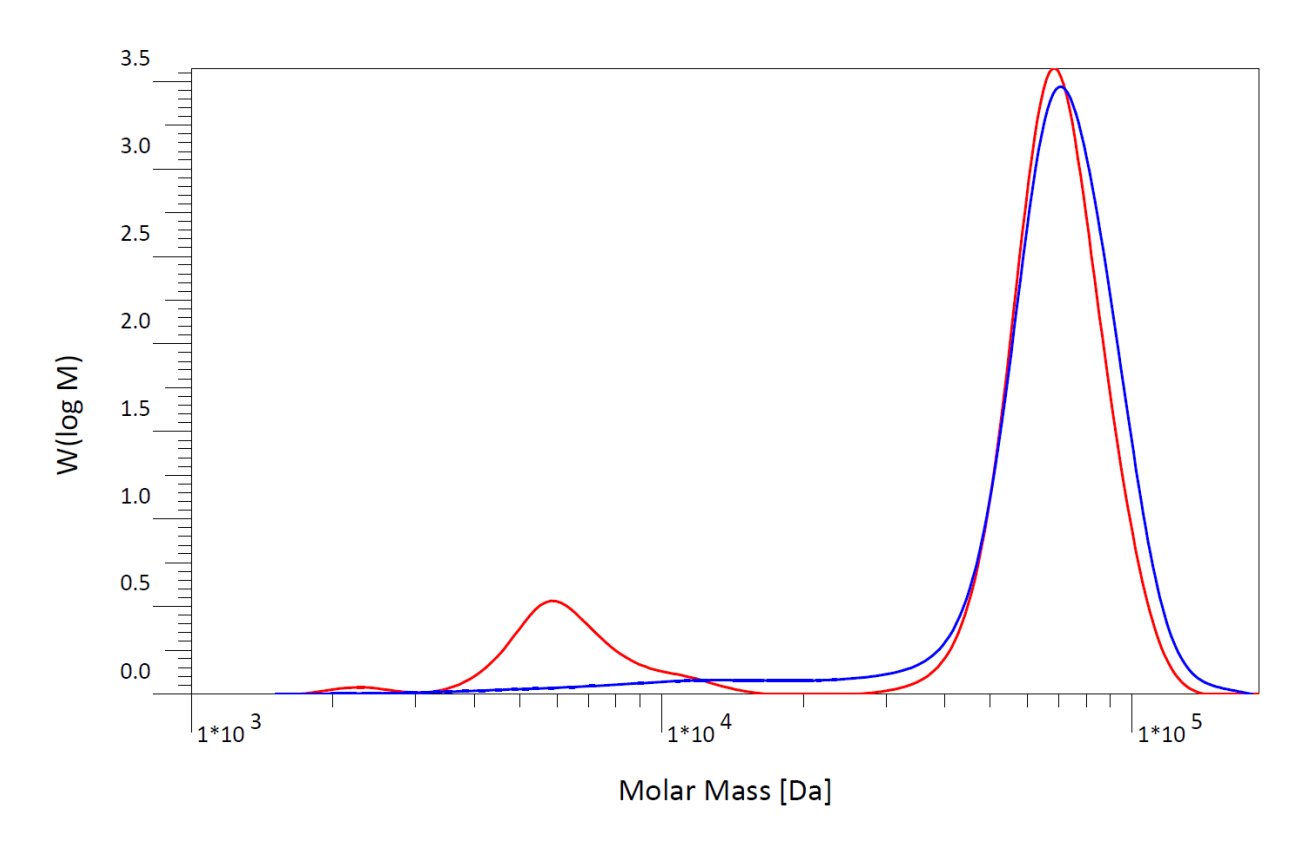


**Figure S13.** Molar mass distribution of Polymer 16 before (red) and after (blue) 3 purification steps in a 30.000 Da MWCO spin column.

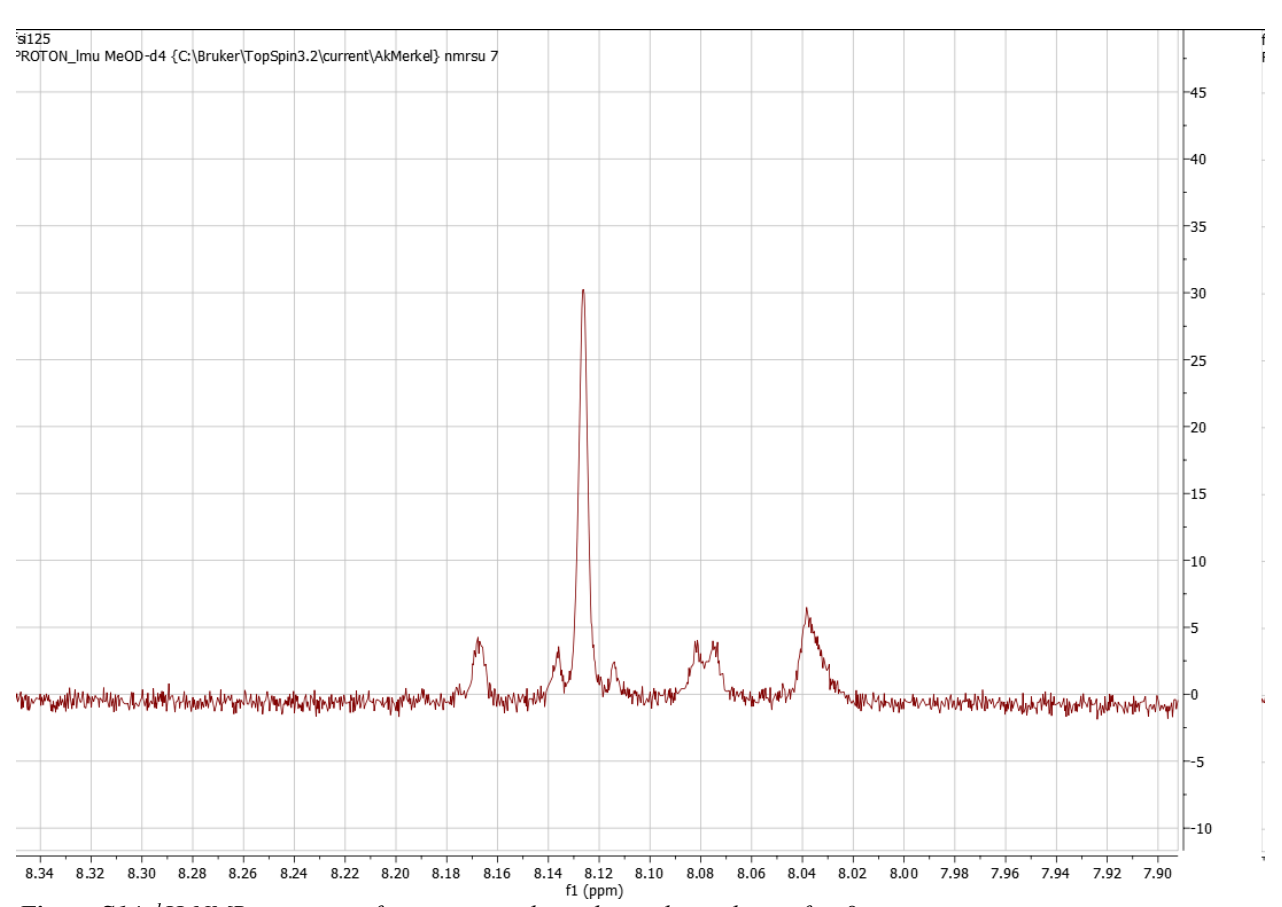


Figure S14. <sup>1</sup>H-NMR spectrum of temperature dependent side products after 8 ppm.

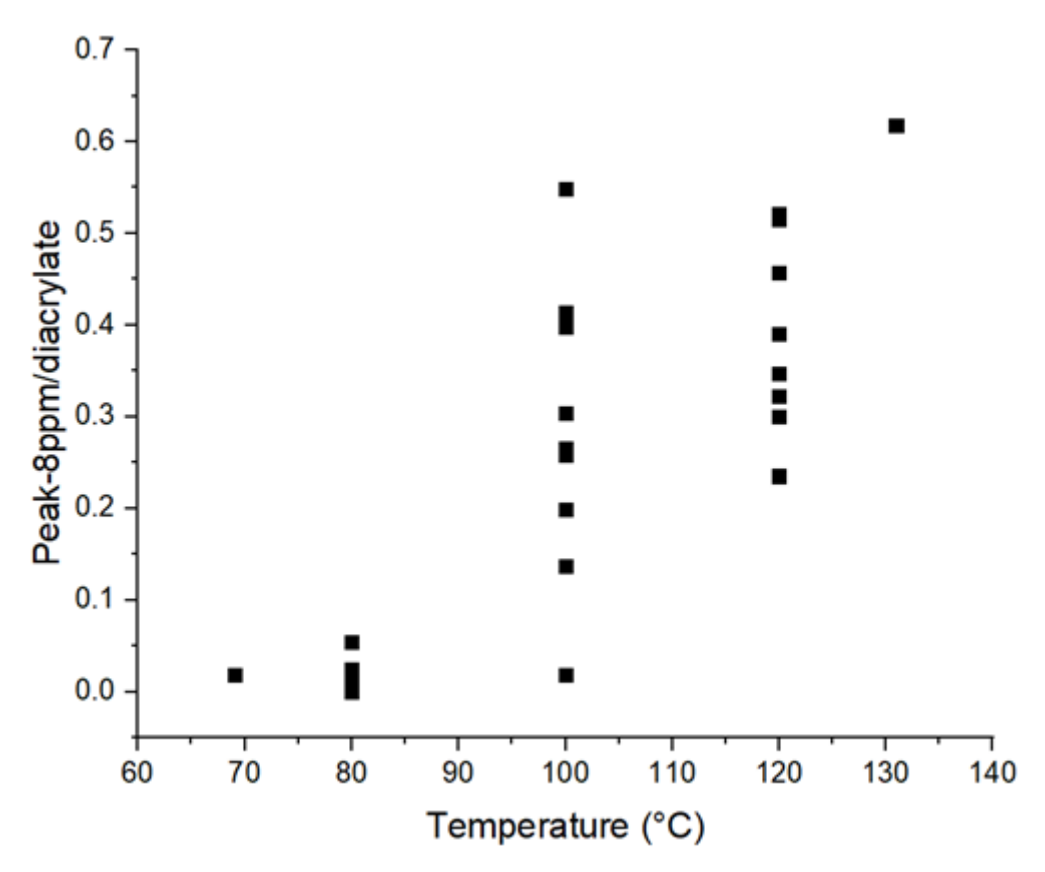
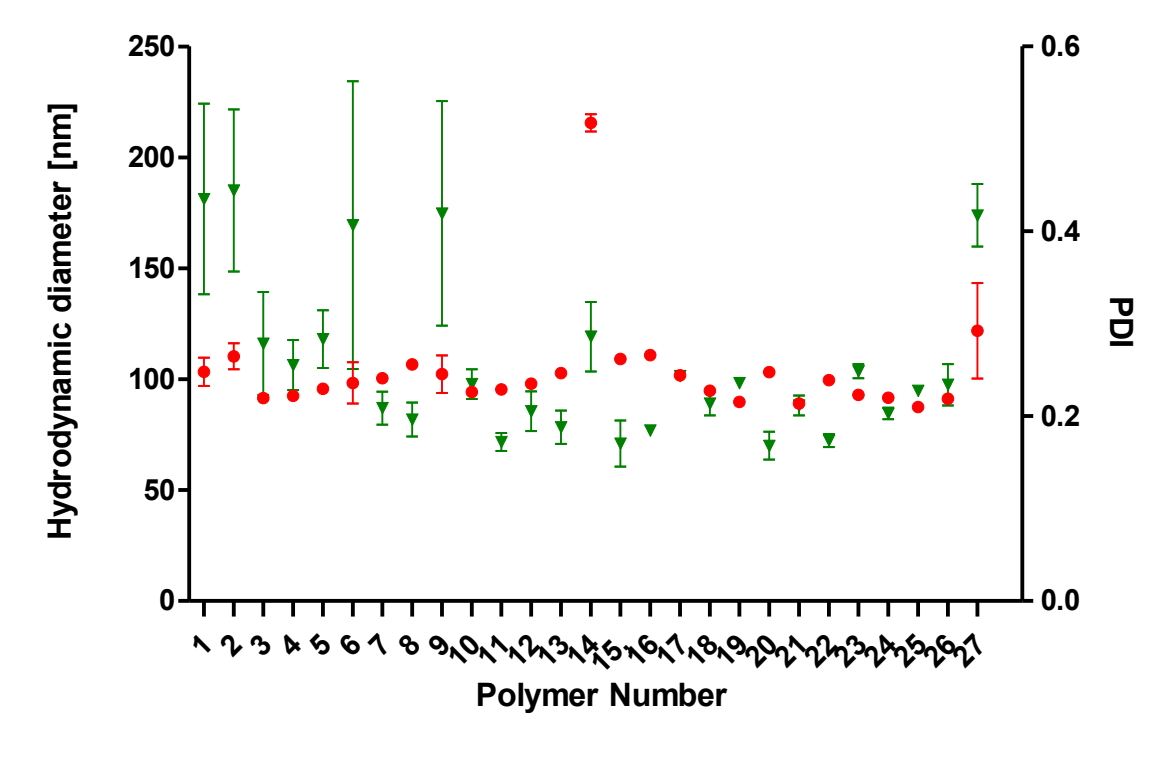
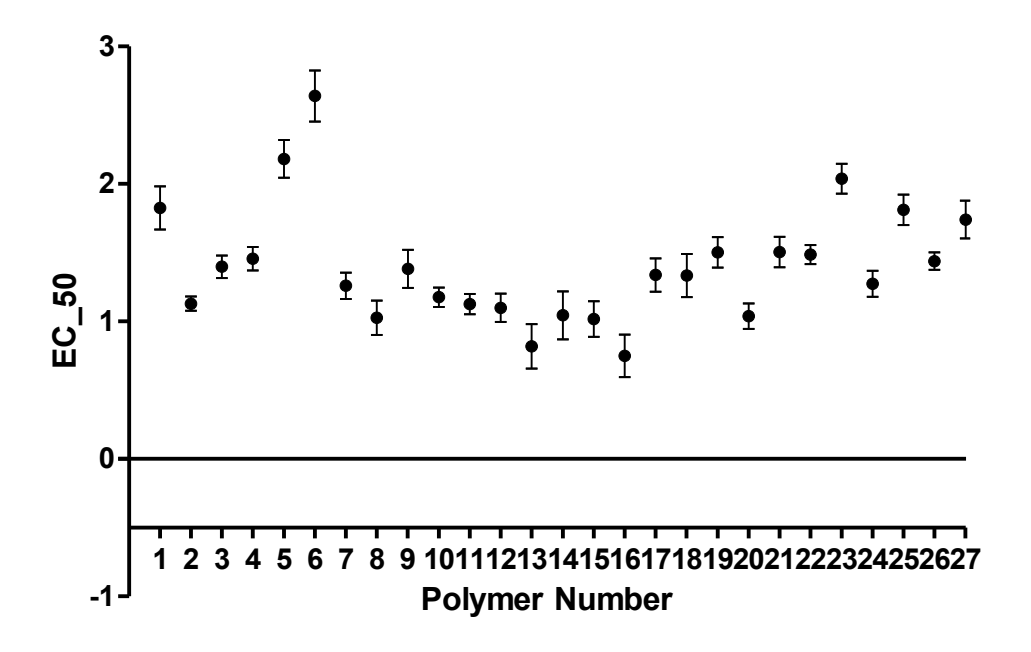


Figure S15. Correlation between side products (NMR species at 8 ppm) and reaction temperature.



**Figure S16.** Dynamic light scattering data of hydrodynamic diameter (red circles) and polydispersity index (green triangle) of siRNA containing particles used for the stability assay.



**Figure S17.**  $EC\_50$  values for siRNA containing nanoparticles generated with different polymers and determined by Heparin and Triton-X competition assay (n=3).

**Table S1.** Validation settings and results for three validation polymers. CQA predictions are shown with 95% confidence intervals from lower (L) to upper (U) limit and results are shown in observed (O) columns.

Polymer	Time	Tem	OA	DAR	OA (L)	OA (U)	OA (O)	Mw (L)	Mw (U)	Mw (O)	Mn (L)	Mn (U)	Mn (O)	PDI (L)	PDI (U)	PDI (O)	+33kDa (L)	+33kDa (U)	+33kDa (O)
V1	48	100	38	1.2	0.378	0.426	0.380	29638	39042	31235	14457	19398	14472	1.89	2.18	2.16	43.99	56.71	46.28
V2	48	100	41	1	0.474	0.522	0.475	34131	44505	40404	16966	22519	18342	1.86	2.14	2.20	51.30	63.55	61.80
V3	48	100	52	0.8	0.580	0.623	0.603	31497	40349	40295	14386	18736	18338	2.04	2.32	2.20	49.41	60.85	61.71

# IV. Machine Learning on an Orthogonal Polymer Library Reveals Governing Factors and Optimizes PBAE Copolymers' Synthesis and Performance

This Chapter was submitted to Biomaterials:

Sieber-Schafer, F.; Kromer, A. P. E.; Molbay, M; Carneiro, S; Jiang, M; Nguyen, A; Müller, J; Farfan Benito, J.; Merkel, O. M. Machine Learning on an Orthogonal Polymer Library Reveals Governing Factors and Optimizes PBAE Copolymers' Synthesis and Performance

The Contribution to this chapter consisted in the synthesis of used polymers, preparation and physicochemical characterization of nanoparticles as well as the *in vitro* and *in vivo* performance evaluation.

# 1. Abstract

Pulmonary siRNA delivery is a promising therapeutic approach for future pandemics and many non-infectious lung diseases. Polymeric nanocarriers, especially poly( $\beta$ -aminoesters) are an easily tunable and versatile delivery system to protect RNA from degradation. To maneuver the vast chemical space and generate control and understanding of synthesis parameters, an orthogonal polymer library of amphiphilic-spermine-based poly( $\beta$ -aminoesters) was investigated for gene knockdown, toxicity and particle stability. Subsequently, a Nested-Leave-One-Out Cross Validation approach was chosen to screen different machine learning models allowing to capture useful information within the limited dataset. Analyzing key manufacturing variables governing the particle performance identified too high intra-particle stability as a disadvantage for successful gene knockdown. This finding facilitated improved model performance through including experimental stability as feature. Leveraging these combined and optimized models, a novel polymer candidate was predicted and subsequently validated in vitro. A superior knockdown and toxicity profile as well as stability trends were confirmed. In vivo experiments, however, highlighted the lack of in-vitro-in-vivo correlation after model optimization for in vitro performance.

# 2. Introduction

RNA-based therapeutics are rapidly transforming modern medicine, demonstrating profound impact across diverse therapeutic areas. The global pandemic highlighted the critical role of mRNA vaccines as a leading-edge biotechnological solution 87,88 for proactive disease prevention. While the success of mRNA vaccines is undeniable, the therapeutic potential of RNA extends considerably beyond prophylactic applications. Harnessing the inherent versatility of RNA's biological functions opens up a wide spectrum of therapeutic possibilities, reflecting their fundamental role in cellular processes. One potential therapeutic approach is the use of short interfering RNA (siRNA) for taget gene silencing. This regulatory RNA is built intracellularly by slicing double stranded RNA (dsRNA) molecules into 20-25 nucleotide long sections and leading to mRNA degradation via an enzyme complex called "RNA induced silencing complex" (RISC). This mechanism could unlock a promising pulmonary antiviral therapeutic strategy for future pandemics<sup>89</sup>. Since RNAs are prone to degradation after injection into a patient due to ubiquitously expressed RNase enzymes, they need to be protected. For this purpose, various nanocarriers, generated from different materials and compositions, are used. Intensively investigated carriers for performing successful delivery are polymeric delivery systems such as PEI<sup>90</sup>, PLGA<sup>91,92</sup> or PBAEs<sup>93,94</sup>. Although all are established materials, only the latter provides high cargo condensation while being biodegradable at the same time<sup>95</sup>, making PBAEs well-suited for RNA delivery.

As the tremendous amount of potential chemical structures enables infinitely many possibilities of tailoring polymers for each individual use case<sup>96</sup>, a strategy is needed, for researchers to design a carrier system that suits their needs faster than with a classical trial-and-error approach. One potential way to do so is rational design using human knowledge <sup>97–99</sup>. While promising, this requires a large amount of expertise and may lead to human errors due to biases and limited capability of extrapolating beyond experience. Another strategy used, is the screening of big libraries <sup>100,101</sup>. This allows for the discovery of a broad chemical space and has already led to the discovery of high-performing carrier systems. However, while being promising on the one hand, this method can only be applied if abundant resources, time and workforce are available which is not applicable for many labs. For this purpose, drug delivery research has started to implement more systematic attempts such as design of experiments (DoE), a method where an a-priori design space is set up, helping in systematically discovering a huge space without performing unnecessary experiments. Even though this method established itself as the gold

standard in industry for most optimization tasks<sup>102</sup>, it provides a rigid scaffold limited by the pre-selected design region and data points.

Machine learning (ML) is a powerful method that can overcome this limitation by allowing for a nearly infinite flexibility in data analysis, optimization and prediction, which makes it an increasingly integral component of modern drug discovery pipelines<sup>103,104</sup>. In recent years, several groups have contributed towards potential applications of ML in designing drug delivery systems<sup>105,106</sup>. However, ML is known to be heavily dependent on both data quantity and quality, which is a problem in the field of polymeric drug delivery, where data is often sparse or too heterogenous to use. Current contributions in the field predominantly focus on either machine learning (ML)-assisted high-throughput screening<sup>107</sup> or the utilization of existing datasets <sup>108</sup>. However, these approaches present inherent limitations, particularly within academic research settings. High-throughput screening infrastructure is often unavailable or impractical for many research questions, while sufficiently large and diverse datasets, capable of enabling robust predictive modeling, remain scarce, especially in comparison to the data abundance available for small molecules.

Here a different method is introduced, where ML is used within a previously synthesized small dataset of spermine-based amphiphilic poly-beta aminoesters (PBAEs)<sup>109</sup>. The data obtained by using an orthogonal DoE design allowed for precise synthesis and a deeper understanding of the process itself. Subsequently, it is used to optimize PBAE capability for successful gene knockdown while maintaining low cytotoxicity. Additionally, a nested leave-one-out crossvalidation loop is employed to design a robust algorithm for predicting synthesis conditions that enable the polymerization of new lead candidates, one of which outperformed the current benchmark. Furthermore, machine learning proved well-suited for integrating additional experimentally determined features, offering flexibility in handling complex and heterogeneous input data. Finally, a deeper understanding of feature-relations was generated, by performing feature ablation studies and investigating SHAPley<sup>110</sup> values for the models. To translate the theoretical work into a practical set-up and to show the strengths but also the limitations of machine learning in this context, subsequently the optimized nanocarrier was initially tested in vitro. Here, the performance of the algorithm was validated and key findings about particle stability were confirmed. Testing the in-vitro-in-vivo-correlation, gene knockdown and toxicity as well as immunogenicity were investigated in mice.

This study highlights the value of applying machine learning to an existing small orthogonal dataset from a previous DoE study, enabling prediction and interpretation of delivery system performance without relying on broad experimental screening.

# 3. Materials and Methods

#### **Materials**

Dicer substrate double-stranded siRNA targeting enhanced green fluorescent protein (eGFP) (siGFP, 25/27mer), and scrambled, negative control siRNA (siNC, 25/27mer) were purchased from IDT (Integrated Technologies, Inc., Leuven, Belgium). Sequences and additional information are provided in the Supporting Information, Table S1. HEPES (4-(2-hydroxyethyl)-1-piperazineethanesulfonic acid), ethyl trifluoroacetate, sodium chloride, Tris-EDTA buffer solution 100×, RPMI 1640 medium, Triton X-100, heparin sodium salt from porcine intestinal mucosa, heat-inactivated fetal bovine serum (FBS), penicillin/streptomycin solution (P/S), geneticin (G418), Dulbecco's phosphate-buffered saline (PBS), cOmplete<sup>TM</sup> Mini EDTA-free protease-inhibitor-cocktail were obtained from Sigma-Aldrich (Darmstadt, Germany). Branched polyethyleneimine (PEI) (5 kDa, Lupasol G100) was a kind gift from BASF (Ludwigshafen, Di-*tert*-butyl decarbonate, Germany). oleylamine, spermine, dimethylformamide (99,5% pure), Lipofectamine 2000, OPTI-MEM serum reduced medium, 0.05% trypsin-EDTA, Alexa Fluor 647 NHS ester, and a SYBR Gold Nucleic Acid Gel Stain 10,000X concentrate in DMSO and siMMP7 were purchased from Thermo Fisher Scientific (Schwerte, Germany). 1,4-Butanendiol diacrylate was obtained from TCI Chemical Industry Co., Ltd. (Tokyo, Japan). Trifluoroacetic acid (99,9%, extra pure) was purchased from Acros Organics (Geel, Belgium). Methanol-d6 was obtained from Deutero (Kastellaun, Germany). Dichloromethane, methanol, ammonia, potassium permanganate, magnesium sulfate, acetone, pentane, and formic acid (>99% pure) were purchased from VWR Chemicals (Ismaning, Germany).

#### **Data Preprocessing**

Experimental data was saved in Excel format and was transformed in a pandas dataframe. The features were defined as Time ("Time"), Temperature("Tem"), initial Oleylamin content ("OA"), Diacrylate ratio ("DAR"). As target values we defined Gene Expression, Toxicity and Stability. Note that stability was included as an additional input feature during model training for the prediction of gene expression and stability, and results were compared to a model trained without this feature. Subsequently data was scaled using a MinMaxScaler. In this complete dataset, no values were missing.

#### **Nested-CV-Loop**

The selection of an appropriate model is a critical step in running a predictive machine-learning pipeline. Because we are dealing with data scarcity, we used only algorithms that are known to

perform well with limited data. Each model was placed in a single scikit-learn pipeline together with a Min–Max scaler to avoid information leakage. We employed a nested cross-validation scheme: first, 15 % of the data was split off as a hold-out set, which was evaluated only after hyper-parameter optimization. To ensure that the hold-out set represented the distribution of the training data, we discretized the continuous target into five equal-frequency (quantile) bins and stratified the train–test split on those bins. In the inner loop, 100 randomly chosen hyper-parameter configurations were assessed for each model using leave-one-out cross-validation (LOOCV). After ten outer-loop repetitions, the model with the lowest mean absolute error (MAE) and its associated optimal hyper-parameters were selected for subsequent optimization.

# Modeling with Stability as Input

To compare whether certain additional experimental data can help in predicting others, we investigated the influence of the experimentally determined intra-particle stability of the nanoparticle suspension. To do so, we included experimental stability values as additional features into the gene expression and toxicity models. Since we experienced a threshold-like behavior of Gene Expression and stability, the stability data was binarized after scaling.

#### **Feature Ablation**

To investigate the influence of the single features and whether they influence the predictive power of the model, feature ablation experiments were executed. For this purpose, we iteratively removed features and compared the performance across all LOOCV splits as absolute mean error with a base model containing all features. When exceeding the error threshold, the feature was assumed to just add noise to the model and was rated irrelevant.

#### **Optimized Model Comparison**

Model evaluation included a comparison of the optimized models against a simple mean predictor baseline, which always predicts the average target value from the training set. The MAE of this baseline was used as a straightforward benchmark and contrasted with that of our machine learning models, both with and without stability included as an input feature.

### **Model Interpretation**

Model interpretation was performed using SHapley Additive exPlanations (SHAP) values to quantify each feature's contribution to the difference between the model's prediction and the expected value, providing insights into model behavior and enabling identification of critical features. Beeswarm plots were used to visualize feature importance for models trained with and without stability as an input feature. Furthermore, waterfall plots were used to illustrate the decision-making process of the models. Finally, feature relationships were investigated using scatter plots of SHAP values against their corresponding feature values.

#### **Prediction Pipeline**

Parameter prediction was performed using a combinatorial approach. Specifically, we generated discrete parameter ranges and combined these ranges to create an exhaustive list of possible parameter settings. Evaluation was performed using models trained without stability as feature. The resulting performance metrics were stored in a data frame and subsequently sorted using a hierarchical sorting strategy. This allowed us to identify parameter configurations that maximized gene knockdown while minimizing toxicity.

# **Triboc-Spermine Synthesis**

Tri*tert*-butyl carbonyl spermine, abbreviated as tri-Boc-spermine (TBS) was synthesized as described elsewhere<sup>111</sup>. Briefly, spermine (1 equiv) was dissolved in methanol and stirred at -78 °C before ethyl trifluoroacetate (1 equiv) was added dropwise. Subsequently, the mixture was stirred at -78 °C for 1 h and then at 0 °C for 1 h. Without isolation, di*tert*-butyl decarbonate (4 equiv) was added dropwise to the solution and stirred at room temperature for 2 days. Finally, the solution was adjusted to a pH above 11 by 25% ammonia and stirred overnight to cleave the trifluoroacetamide protecting group. The solvent in the mixture was then evaporated under vacuum, and the residue was diluted with dichloromethane (DCM) and washed with distilled water and saturated sodium chloride aqueous solution. The DCM phase was finally dried by magnesia sulfate and concentrated to give the crude product. The crude product was purified by column chromatography (CH<sub>2</sub>Cl<sub>2</sub>\MeOH\NH<sub>3</sub>, aq 7:1:0.1, SiO<sub>2</sub>, KMnO<sub>4</sub>;  $R_f$  = 0.413). TBS was isolated and characterized by  $^1$ H nuclear magnetic resonance spectroscopy ( $^1$ H NMR).

# **Polymer Synthesis and Characterization**

Poly-spermine-*co*-oleylamine β-aminoesters (P(SpOABAE)) were synthesized based on a previously described approach <sup>90</sup>. Briefly, TBS as a hydrophilic monomer, oleylamine (OA) as a hydrophobic monomer, and 1,4-butanendiol diacrylate (DA) as backbone were mixed in different molar ratios in dimethylformamide (DMF), resulting in total concentrations of 300 mg/mL. After the respective reaction time, mixtures were transferred to Petri dishes to evaporate the solvent. The subsequent deprotection of the polymer was carried out in a mixture of 20 mL of dichloromethane (DCM) and 1 mL of trifluoroacetic acid (TFA) for 100 mg of polymer, followed by stirring for 2 h at room temperature. In the following, DCM/TFA was evaporated and the dry deprotected product was precipitated 3 times in pentane using acetone to dissolve the precipitate. Supernatants were discarded, and the final precipitate was dried for 2 days under vacuum (room temperature, 20 mbar). The synthesis process is depicted in Figure 1A. Final polymers were characterized by <sup>1</sup>H NMR and GPC. Measurements were performed with an Agilent aqueous GPC using a PSS Novema Max Lux 100A followed by two PSS

Novema Max Lux 3000A columns. The chromatographic system and calibration standards were set up according to preanalysis from Agilent Technologies on P(SpOABAE) polymers. Measurements were performed at 40 °C in a 0.1 M sodium chloride solution supplemented with 0.3% formic acid. Samples were prepared at 4 g/L and measured at a flow rate of 1 mL/min. Molar mass distributions were obtained through the Agilent WinGPC software against pullulan calibration standards in the range of 180 Da to 1450 kDa. A daisy-chain detector setup of an Agilent 1260 VWD was used, followed by an Agilent 1260 GPC/SEC MDS and ending with an Agilent 1260 RID.

#### Gene Knockdown

H1299 stably expressing eGFP were seeded on 48-well or 24-well plates at a density of 5,000 or 10,000 cells per well in 1640 RPMI supplemented with 10% FCS and 1% Penicilin/Streptomycin, respectively. Nanoparticles were prepared at N/P ratio 10 encapsulating either siGFP or siNC RNA, and cells were transfected 24h after seeding in triplicates with 10 or 20 pmol siRNA per well. After 48 hours, median fluorescence intensity (MFI) was recorded using a BD LSR Fortessa using the BD FACSDivaTM Software and counting 10,000 events. Gene knockdown was calculated as the ratio between MFI of cells treated with siGFP NPs and siNC NPs.

#### **Cell Viability**

Cell viability and toxicity were tested simultaneously using a CellTiter Blue (CTB) and Lactate dehydrogenase (LDH) assay. In 96-well plates, 5,000 16HBE14o- cells were seeded. After 24 hours, the polymer library was tested in triplicates. Each polymer was tested at 8 different concentrations between 1 and 500  $\mu$ g/mL. After 48 hours of incubation, 50  $\mu$ L supernatant of each well was transferred to a fresh plate and LDH was quantified following the manufacturers protocol. Briefly, to each well 50  $\mu$ L of freshly resuspended reagent mix was added, and the plates were incubated in the dark for 30 min. Afterwards, 50  $\mu$ L stop solution was added into each well and absorbance was measured.

For the CTB assays, the cell containing wells were filled up with 30  $\mu$ L of fresh media and 20  $\mu$ L CTB and incubated for 4h. Afterwards, absorbance was measured at 570 and 600 nm.

Using JMP 17 pro, sigmoidal curve fits were generated through all concentrations and repetitions of the CTB and LDH assays, and turning points were calculated and defined as IC50 values.

#### **Determination of attractive forces between siRNA and polymers**

A previously reported stability assay was used to determine the attractive forces between siRNA and polymers. The stability values for the input library were reported in the same publication <sup>109</sup>. Following this protocol, nanoparticle stability was investigated using heparin and triton-X. Briefly, 10 μL nanoparticle suspension was treated with 20 μL of 8 different concentrations of a mixture of heparin and triton-X in a black 384-well plate (Greiner Bio-One, Frickenhausen, Germany). As reference, siRNA solutions resembling the concentrations of NPs were treated with the same concentrations of heparin and triton-X. Plates were sealed and incubated for 1h at 37°C at 250 rpm. Afterwards 5 μL of a 4x SYBR Gold solution were added to each well and mixed by pipetting. After 5 minutes of incubation fluorescence was measured at 492/20 nm excitation wavelength and 537/20 nm emission wavelength. Comparing the fluorescence intensity of the treated nanoparticle solution to the respective siRNA solutions' intensity, a release percentage was calculated. Fitting the released percentage against the used concentration of heparin and triton-X, using Prism5 software, an EC50 value was calculated. This value was defined as the concentration at which half of all siRNA is released from the nanoparticle suspension.

#### **Animal Treatment Protocol**

Female BALB/c mice, aged 6-8 weeks, were purchased from Charles River Laboratories. The mice were housed in a controlled facility for 14 days to acclimatize, with a 12-hour light/dark cycle. All animal procedures were approved by the Government of Upper Bavaria and conducted in accordance with approved protocols.

Mice were intratracheally instilled with 1 nmol of siRNA encapsulated at N/P 10 with either the previous lead candidate or the new ML-2 polymer, administered through intratracheal instillation under ketamine/xylazine anesthesia. As control, equivalent volume of 25kDa hyperbranched PEI polyplexes encapsulating the same amount of siRNA was applied as well as unencapsulated siRNA or pure formulation buffer. All formulations were tested with either siRNA targeted against murine Glyceraldehyde 3-phosphate dehydrogenase (GAPDH) or negative control (NC). Mice were euthanized 24 hours after application mice through cardiac blood collection.

Lungs were flushed twice with 500 μL of PBS buffer containing 2 mM EDTA and one cOmplete<sup>TM</sup>, Mini, EDTA-free protease-inhibitor-cocktail tablet per 10 mL to collect the bronchoalveolar lavage fluid (BALF). Briefly, solutions were injected into the trachea and subsequently recollected. A second 500 μL of the same PBS solution was instilled and

recollected. The collected BALF was centrifuged for 5 minutes at 500 g. The supernatant was frozen at -20°C and stored at -80°C until further analysis.

Lungs were subsequently perfused with 20 mL of 0.9% sterile sodium chloride. To do so, the vena cava inferior was cut and the solution injected into the left ventricle. After sufficient perfusion, one lung lobe from each treatment group was dissected, fixed in 4% paraformaldehyde (PFA) for at least 24 hours, and then embedded in paraffin for histological analysis via H&E staining.

The remaining lung lobes and undissected lungs were stored at 1 mL RNAlater<sup>TM</sup> Stabilization Solution, frozen and stored at -20°C until further analysis.

#### In Vivo Gene Knockdown

GAPDH gene knockdown in mouse lungs was determined through qPCR. RNA was isolated from mouse lungs using Lysing Matrix D tubes containing 1.4 mm Zirconium-Silicate spheres from MP Biomedicals and a TRIzol/chloroform isolation protocol. Briefly, mouse lungs were thawed on ice and transferred to the lysing tubes. After the transfer, 1 mL of TRIzol was added to each tube. Using a Tissue Lyzer the samples were homogenized. The RNA was isolated through chloroform precipitation. After centrifugation, the aqueous phase was washed with molecular grade isopropanol followed by ethanol. The final RNA pellets were dissolved in RNase free water and concentrations were determined. Using a high-capacity cDNA reverse transcription kit (Thermo Fisher Scientific), complementary DNA (cDNA) was prepared. Finally, quantitative real-time PCR (qRT-PCR) was performed applying an iTaq Universal SYBR Green Supermix (Bio-Rad, Feldkirchen, Germany) on a StepOnePlus system (Thermo Fisher Scientific). Beta-Actin was used as the reference gene with Mm\_GAPDH\_3\_SG primers (Qiagen) for GAPDH and Mm\_ACTB\_2\_SG (Qiagen) primers specific for mouse β-actin. For normalization of GAPDH levels, the ΔΔCt method was applied.

#### In Vivo Biodistribution and Cell Uptake

To investigate the biodistribution and cellular uptake 6–8-week-old BALB/c mice were treated with 1 nmol of siRNA fluorescently labeled with a AF647 label as described previously. siRNA was either applied unformulated or encapsulated into the previous lead candidate or ML-2 polymer. After 24 hours, mice were sacrificed, and bladders, lungs, livers, kidneys, spleens, and the hearts were collected. Using an IVIS Lumina III (PerkinElmer, Shelton, CT, USA) fluorescence intensity in these organs was measured.

For further analysis, lungs were dissociated using a gentleMACS tissue Dissociator (Miltenyi Biotec, Bergisch Gladbach, Germany) together with gentleMACS C (Miltenyi Biotec, Bergisch Gladbach, Germany) tubes following the manufacturers protocol. Cell suspensions were

incubated with PBS solution containing Zombie UV<sup>TM</sup> and afterwards stained with FITC antimouse CD45, BUV395 anti-mouse CD3, Vioblue anti-mouse CD4, APC-Cyanine7 anti-mouse CD8, PE-Cyanine7 anti-mouse F4/80, BUV605 anti-mouse CD11c, BV785 anti-mouse CD326, PE/Dazzle<sup>TM</sup>594 anti-mouse CD170 and PerCP/Cyanine5.5 anti-mouse CD19 for 30 min at 4°C. The stained cells were measured using a Cytek® Aurora (San Diego, California, USA) implemented with autofluorescence extraction for the detection of cellular uptake (Figure S1).

# **BALF Cytokine Measurements**

Cytokines from collected BALF solutions were quantified using a LEGNEDplex<sup>TM</sup> Mouse Inflammation Panel (Biolegend, San Diego, California, USA) following the manufacturers protocol and an Attune NxT flow cytometer (ThermoFisher Scientific, Waltham, MA USA). Results are reported as total detected concentration and as relative induction compared to the highest induction for each individual cytokine.

# 4. Results and Discussion

# **Library Performance Evaluation**

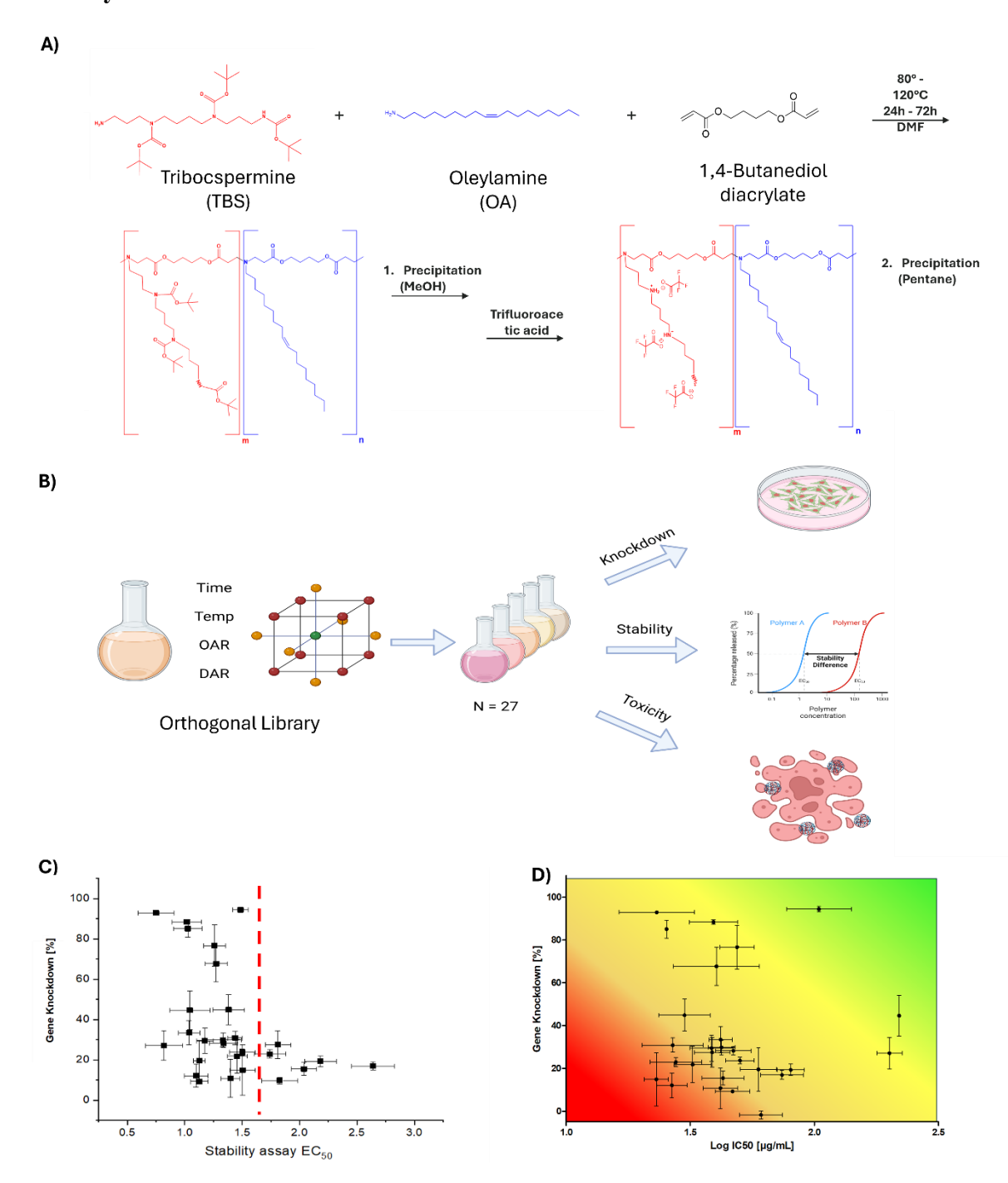


**Figure 1.** Workflow of the screening process applied in this study. A) Synthesis approach of the applied PBAE polymers B) A previously reported library generated through DoE and varying key synthesis parameters was tested for knockdown efficiency, stability and toxicity. C) Gene Knockdown correlated against previously reported stability of particles and D) against cell viability determined via CTB. Error bars depict SD for gene knockdown and SD of the fit for  $EC_{50}$  and  $IC_{50}$  with n=3.

The aim of this work was the investigation and optimization of synthesis parameters governing the performance of PBAE polymers as siRNA delivery vehicles *in vitro* and *in vivo* for pulmonary therapy. We therefore utilized a previously reported library of 27 differently synthesized PBAE polymers (Figure 1A)<sup>109</sup>. The library was generated through a Central Composite Orthogonal design optimizing the synthesis parameters of total synthesis time, synthesis temperature, oleyl amine ratio, being the ratio of the two sidechains, and diacrylate ratio, being the ratio of the sidechains to the backbone (Figure 1B). All factors were investigated over 5 levels and with all resulting polymers, nanoparticles were successfully formulated. Nanoparticle stability was already reported<sup>23</sup>.

To complement the previously reported data set, nanoparticles were tested for gene knockdown in an H1299 eGFP-expressing lung cell line by encapsulating and delivering siRNA against eGFP. The results were plotted against the previously reported stability values (Figure 1C). Interestingly, an apparent division threshold was found within the data set. Above this threshold, the particles appeared to lose their functionality in vitro. This was unexpected since the common consensus suggests that particles need a certain stability to not lose their integrity before reaching the endosome. In contrast, the data presented here suggest that the major bottleneck for the investigated PBAE nanoparticles was not premature particle disintegration but rather excessively strong intraparticular stabilizing forces. Since only below the found threshold a successful gene knockdown above 90% was observed, it was hypothesized that at too high EC50 values, particles did not disintegrate within the endolysosomal pathway to release their siRNA cargo and mitigate gene knockdown. This hypothesis was underscored by the observation that above the identified threshold, the highest achieved gene knockdown effects were below 30%. A previous study reported similar observations, implying that polyplexes lose potency if the intraparticular stabilizing forces become too strong to release the cargo 112. On the other hand, weakening the intraparticular forces can increase the nanoparticles performance<sup>113</sup>. Therefore, a clear design criterion for next generation polymers was stated. The criterion was that nanoparticle stability needed to be lower than an EC<sub>50</sub> value of 1.6, in order to successfully release the siRNA within the endosome.

In the next step, cytotoxicity and cell viability of the polymers from the library were investigated in pulmonary epithelial cells by the means of CTB and LDH assays (Figure S2). A correlation comparison between both IC50 results showed that the tested polymers were well tolerated in a range from 25 to 175 mg/mL and the results from CTB and LDH correlated strongly with each other (Figure S3+S4). As expected, polymers exhibiting higher toxicity also showed a greater negative impact on cell viability, and vice versa. Furthermore, this finding

enabled a reduction in experimental workload and cost since a single assay was sufficient to reliably assess polymer safety. CTB assays resulted in a slightly lower IC50 value than LDH assays (Figure S3). Moving forward, for these reasons CTB was chosen as main readout.

To finally evaluate the performance of the polymer library, gene knockdown was plotted against the IC50 values determined via CTB (Figure 1D). This showed another surprising finding, which was the successful decoupling of toxicity from efficiency of the nanoparticle system. One of the biggest challenges for RNA delivery is the "*efficiency/safety dilemma*", where higher transfection efficiency is often associated with increased cytotoxicity. The root cause is most likely associated to the membrane disruptive potential of the carrier system. A certain membrane fusogenicity is necessary for endosomal escape, while excessive disruption of endolysosomal compartments or cellular membranes can trigger immunogenicity, apoptosis and toxicity<sup>114–116</sup>. It was therefore a remarkable finding that the investigated library contained a polymer with exceptional gene knockdown as well as superior safety profiles (Figure 1D, green area).

#### **Nested CV Approach**

Using the previously reported dataset, we aimed to demonstrate the power and flexibility of machine learning algorithms in leveraging orthogonally designed input data. Building upon the nested cross-validation framework described before<sup>117</sup>, we implemented a similar approach with specific modifications tailored to our low-data context (Figure 2A). First, recognizing the limitations of complex models in data-scarce settings, we opted to exclude the neuronal network component present in the referenced methodology. Second, to ensure the hold-out set was representative of the training data distribution, we stratified the dataset based on the target variable, dividing the data into five bins prior to splitting. Furthermore, within the inner crossvalidation loop, we employed LOOCV, which was chosen to maximize the training data available for each inner fold, which is particularly advantageous when working with limited datasets. In our experiments, we trained models to predict two distinct target variables: Gene Expression post-treatment and Toxicity, quantified as IC50 (see Methods section for details). We also investigated the potential benefit of incorporating additional nanoparticle characteristics, specifically stability, as input features. While we observed improved results for the stability-included approach for all Gene Expression models (Figure 2B), addition of stability did not seem to have a big impact on the IC50 value (Figure 2C). The only model that slightly improved was the DecisionTree (DT). However, its performance was still poorer than that of the best model without stability included, which was the RandomForest (RF) with an MAE of 0.3673. For the Gene Expression model, XGBoost outperformed other models (MAE of 14.18). However, when including stability, the Support Vector Regressor (SVR) was slightly better.

Good performance of an SVR with low data and non-linear interactions was already seen previously<sup>118</sup>. Among the best performing model class, we picked the best hyperparameter-setting for the most robust models (Figure S5), which were further optimized in the next steps.

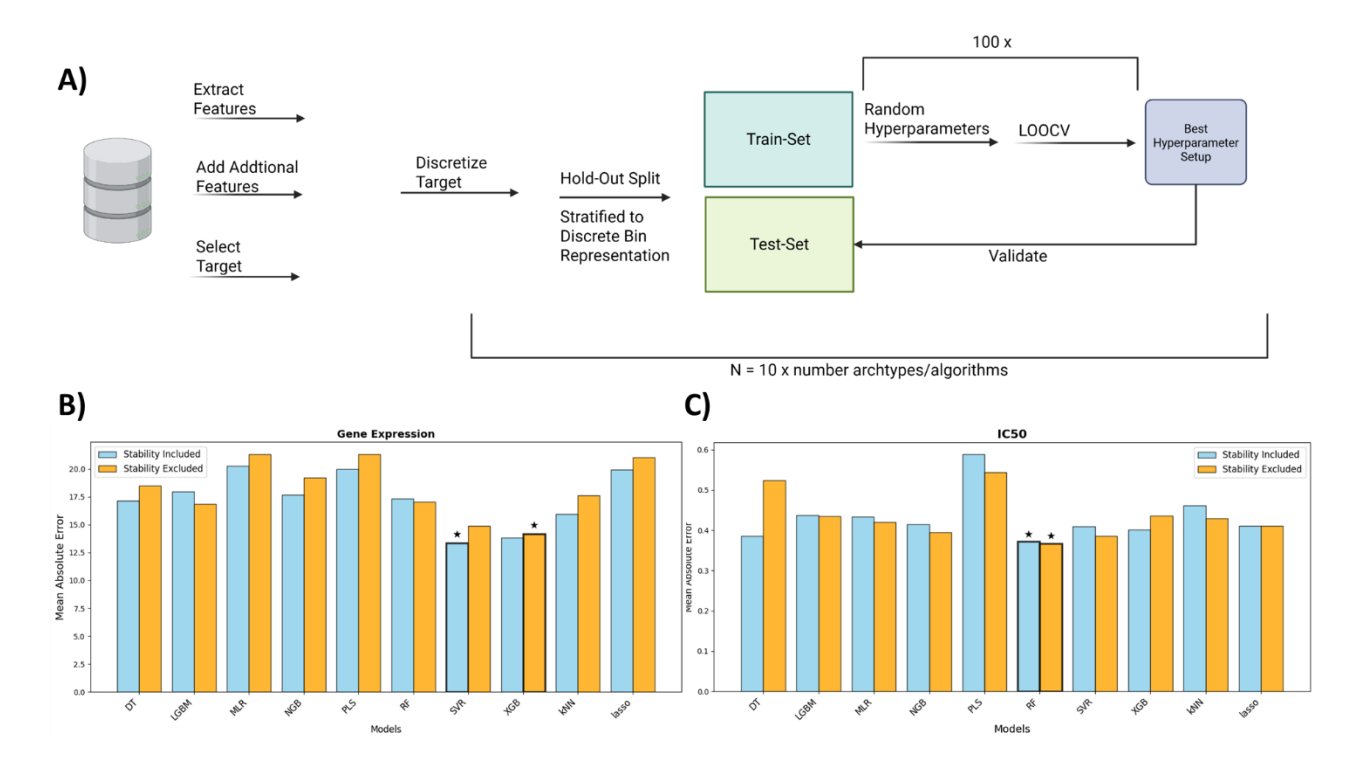


Figure 2. Nested-Leave-One-Out Cross-Validation Approach A) Machine learning pipeline where data is preprocessed and subsequently categorized to allow for stratified splitting of holdout data. The train set is used to tune each algorithm with a random hyperparameter search and leave-one-out validation. The process is repeated ten times and the mean absolute error is calculated to obtain the most robust model. B) Mean Absolute Error of multiple models tested for Gene Expression with the ML pipeline. Models with stability measurements of nanoparticles included (blue). The models marked with an asterisk and a bold frame are the most robust models selected for optimization. C) Mean Absolute Error of multiple models tested for IC50 with the ML pipeline. Models with stability measurements of nanoparticles included (blue). The models marked with an asterisk and a bold frame are the most robust models selected for optimization.

# **Feature Ablation Experiment**

To further optimize model performance and enhance process understanding, we conducted a feature ablation experiment (Figure S6). In this experiment, we evaluated the performance of each model, assessed via LOOCV, by iteratively removing individual features. Feature ablation for the Toxicity model showed no significant impact on performance, which may reflect the model's limited predictive accuracy and reduced sensitivity to input feature contributions. Conversely, for the Gene Expression model, we observed that ablating Time and Diacrylate-

Ratio (DAR) improved stability-excluded model performance. In contrast, DAR remained important for the stability-included model. These findings align with our prior work, which indicated a limited impact of reaction time on polymer characteristics.

### **SHAP Analysis**

To gain deeper insights into model decision-making, we calculated SHAP values for all models (see Figure 3A and 3B). The SHAP analysis generally corroborated the findings from the feature ablation experiment. Furthermore, it elucidated feature importance for predicting high knockdown/low gene expression, suggesting a requirement for high oleylamine content (OA Initial) and elevated Temperature (Tem) in the stability-excluded model. In contrast, the stability-included model's SHAP values reflected the stability threshold identified previously. For the IC50 prediction, Temperature emerged as a significant parameter, with lower temperatures associated with reduced toxicity, while higher OA Initial concentrations appeared favorable. This observation may be attributed to the potential formation of a side-product at elevated temperatures, as documented in our earlier publication<sup>109</sup>. Stability, however, exhibited no influence on predicted toxicity (Figure 3B). It is important to note that SHAP values represent model interpretations rather than ground truth. Given the weaker predictive performance of the IC50 model, these results require cautious interpretation. Detailed SHAP plots for all models and features and correlation plots between SHAP values and features are provided in the Supplementary Information (Figure S7 and S8).

#### Final Model Performance and Baseline Comparison

To demonstrate the final model performance, we benchmarked all trained and optimized models against a dummy baseline model (see Methods section). Additionally, we visualized the results in predicted-versus-real plots (Figure S9). The Gene Expression stability-excluded model exhibited promising performance, achieving a MAE of 10.59 and a Pearson correlation coefficient (r) of 0.8494 in the predicted-versus-real plot (Figure 3A and Figure S9A). The incorporation of stability as a feature further enhanced predictive performance (MAE= 7.605, r=0.9078), underscoring the existence of a stability threshold above which particle stability is too high to release the cargo into the cytosol (Figure 3A and Figure S9B). For the Toxicity model, performance improvements over the baseline (MAE of 0.2816 versus MAE of 0.3476) were observed, and a correlation between predicted and experimental values was evident for the stability-excluded model (r= 0.3605, Figure 3B and Figure S9C). However, no significant difference was found between the two different models (Figure 3B and Figure S9D), further supporting the conclusion that stability does not substantially influence the toxicity of the nanocarrier system.

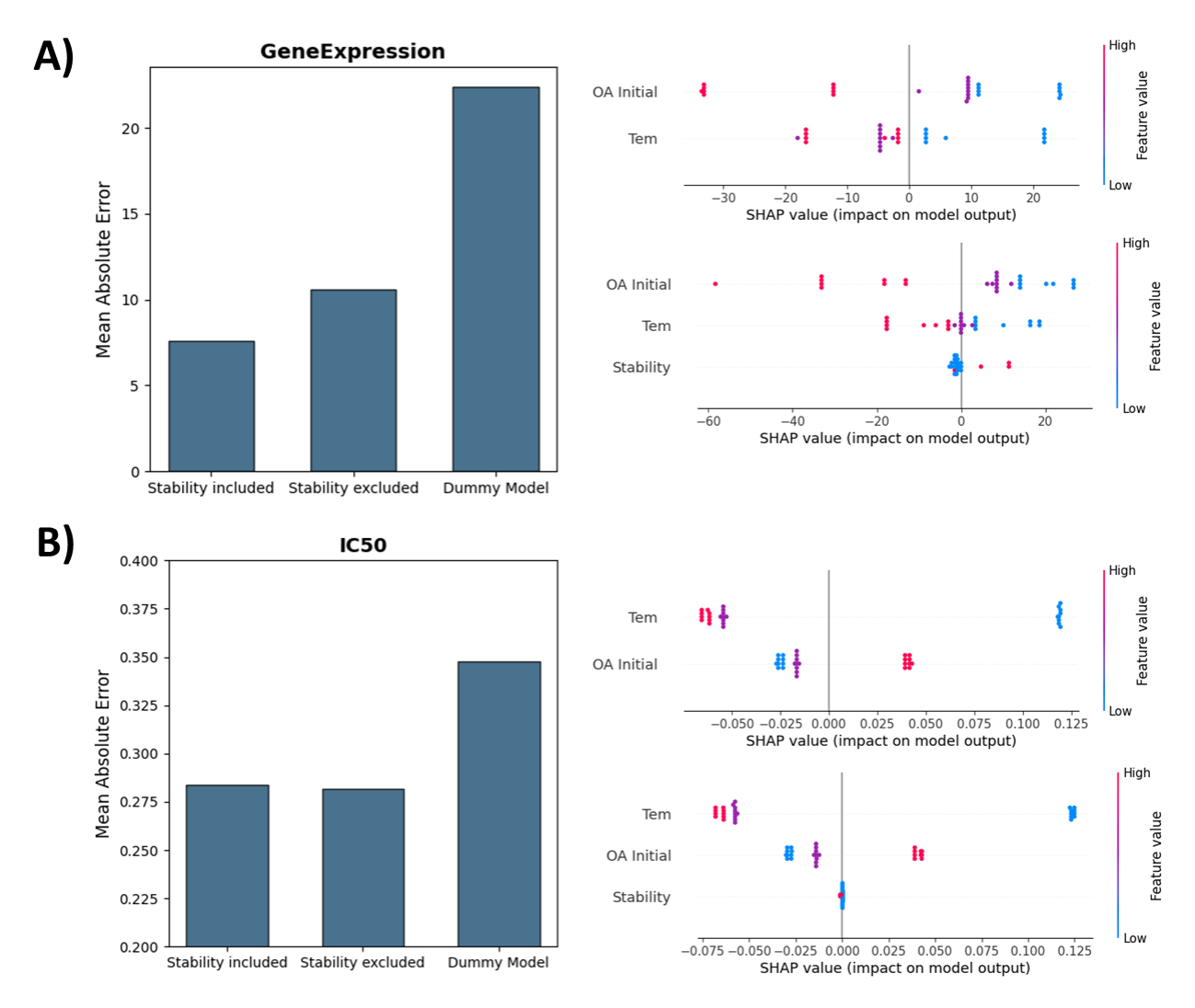


**Figure 3.** Optimized Model Characteristics A) Gene Expression MAE Comparison of optimized *Stability-included* and *excluded* Models with a Dummy-Baseline Model evaluated with LOOCV *above:* SHAP values of *Stability-included Model* B) IC50 MAE Comparison of optimized *Stability-included* and *excluded* Models with a Dummy-Baseline Model evaluated with LOOCV *above:* SHAP values of *Stability-excluded Model* and below: *Stability-included Model*.

#### **End-to-End Prediction Pipeline and Validation**

To ultimately validate the utility of machine learning with limited data, for predicting novel formulations, we constructed an end-to-end prediction pipeline (Figure 4A). This pipeline involved generating all feasible combinations within physically plausible feature ranges and employing our stability-excluded model as an independent multi-output model to predict Gene Expression/Knockdown and Toxicity. Given the superior predictive power of the Gene Expression model, we implemented a hierarchical sorting strategy, prioritizing high knockdown followed by low toxicity. The model-predicted optimal polymer, termed ML-2 and

characterized by 95% OA Initial and synthesis at a Temperature of 130°C, was subsequently synthesized (see Methods section), analyzed (see Figure S10 and Figure S11), and experimentally validated. To further highlight the model's decision path, we added additional SHAP waterfall plots (see Figure S12 and Figure S13), confirming the results from the full model's beeswarm plot.

# Machine Learning-Derived Polymer Evaluation in vitro

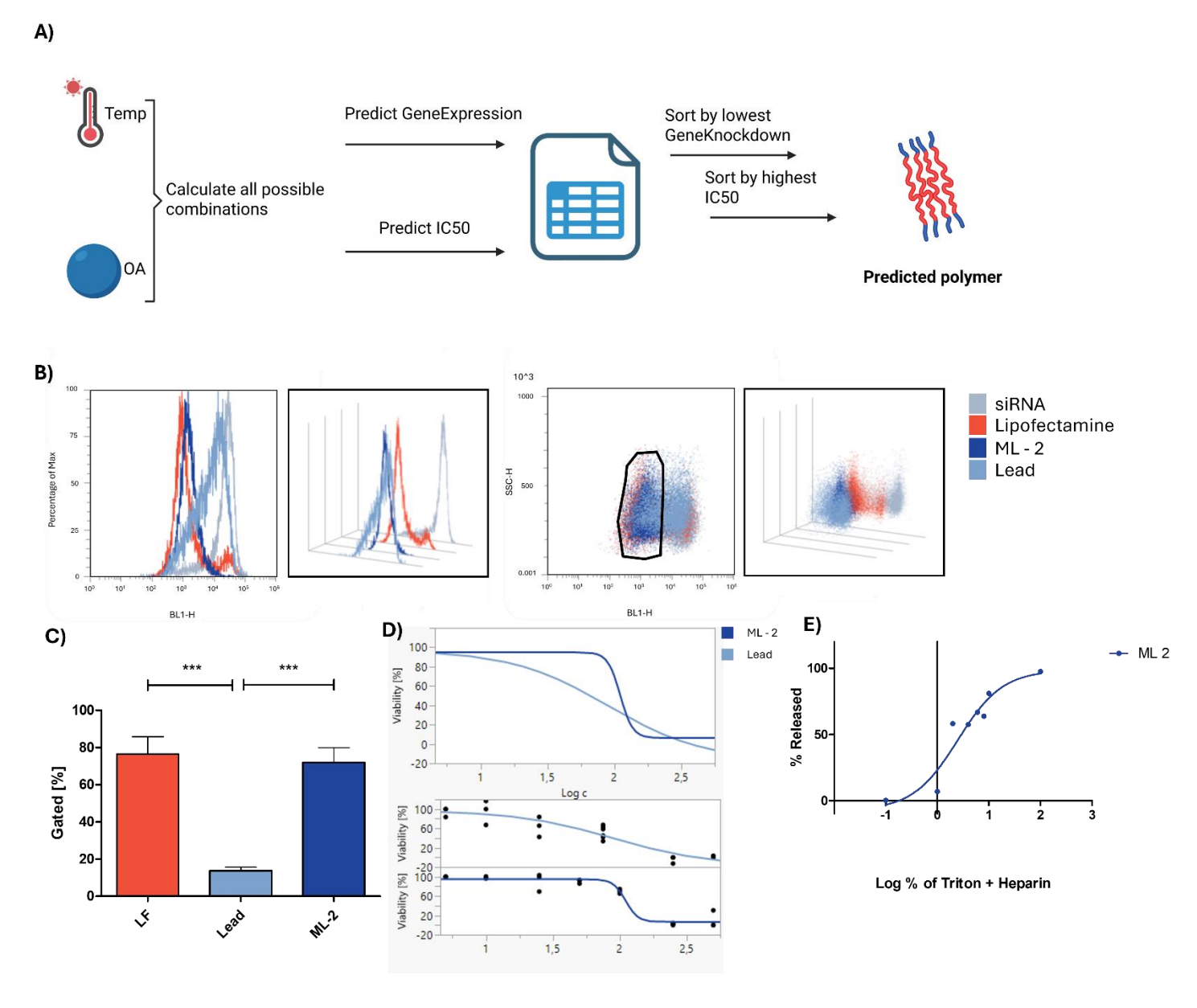


Figure 4. In vitro performance evaluation and comparison of optimized PBAEs. A) Overview of the prediction pipeline for the optimized polymer, B) Histogram and Dot plot of H1299 eGFP cells treated with Lipofectamine 2000, ML-2 or the previous lead candidate encapsulating siGFP siRNA, and C) percentage of gated cells with nearly complete knockdown of eGFP with N=3 (\*\*\* depicting a  $p \le 0.001$ ). D) Toxicity of ML-2 and lead

candidate determined via CTB assay with n=3, and E) stability of ML-2 determined through Heparin and Triton-x competition. Dots depict mean of n=3.

To validate the performance of the new ML-2 polymer as pulmonary delivery agent, it was compared against a previously reported lead candidate 113 derived from classical trial and error synthesis optimization. In the following this polymer will be referred to as "Lead" candidate. Besides different synthesis settings, these two polymers mainly differ in their OA ratio, with the predicted ML-2 having a higher ratio at 93% and the previous Lead polymer a lower at 75%. To investigate if the new ML-2 polymer was indeed superior in performance, a gene knockdown experiment in H1299 eGFP cells was conducted. As shown in Figure 4 B) ML-2 did indeed mediate a more potent gene knockdown than the Lead polymer and seemingly a more complete downregulation than Lipofectamine 2000 (Figure 4 B). The median fluorescence intensity did not differ significantly between Lipofectamine 2000 and ML-2 (Figure S14). To get a more detailed view on the differences on the polymers' performances, the dot plots of the cell populations were compared via the gated percentage (Figure 4 B +C). ML-2 was clearly superior to the Lead polymer but showed again no statistical difference compared to Lipofectamine 2000. The Lead polymer on the other hand showed a large cell population with a non-complete gene knockdown. This indicates that the lead polymer does not reach saturation of cytosolic siRNA delivery unlike ML-2. This difference of saturation is also depicted in the gated percentage (Figure 4 C) and clearly shows the superior efficiency of ML-2 compared to the Lead polymer.

A major downside of the previous Lead candidate is the early onset of toxicity as can be seen from the CTB curve (Figure 4 D). Even though the IC $_{50}$  value of the Lead polymer is in an excellent range with 89  $\mu$ g/mL, the early onset of the curve decline indicates that toxicity can already occur at much lower concentrations. ML-2 showed a superior IC $_{50}$  value, although in a comparable range with an IC $_{50}$  value of 109  $\mu$ g/mL. However, additionally to a higher IC $_{50}$  value, the curve decline was also much steeper indicating a much later "onset of toxicity" at higher concentrations. This finding confirmed the potential of the machine learning approach since ML-2 showed to have better efficiency and safety profiles than the previous lead candidate.

Finally, to prove our previous findings, we determined the stability of the ML-2 nanoparticles (Figure 4 E), which was in the expected range, below the above-described threshold necessary for successful gene delivery.

# Machine Learning-Derived Polymer Evaluation in vivo

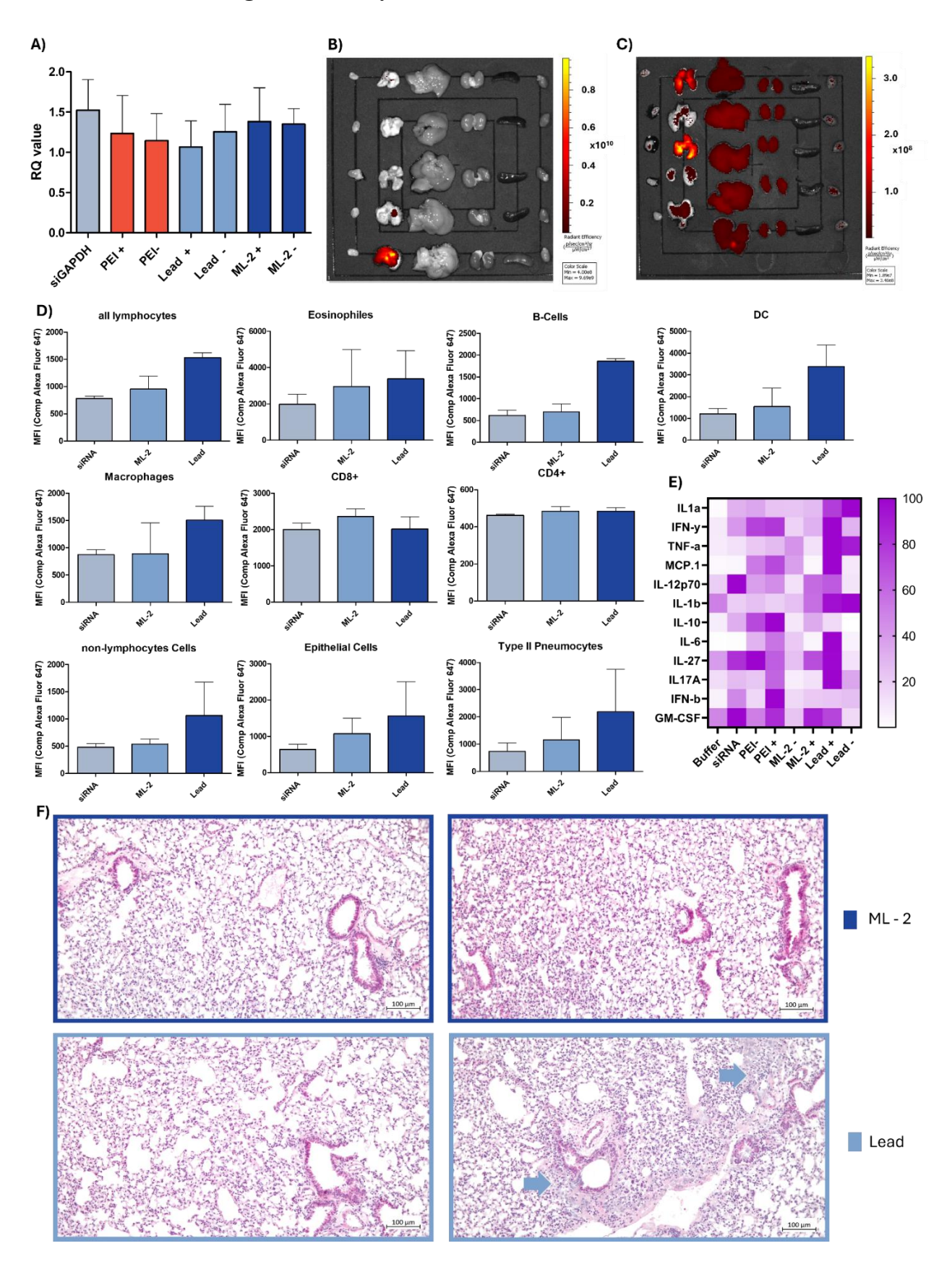


**Figure 5.** *In vivo* results of the lead and ML-2 comparison. A) Fold-change of GAPDH against β-actin determined by ΔΔCt method with buffer only as reference standard. B) Fluorescence intensity measurements of bladder, lungs, liver, kidneys, spleen, and heart (from left to right) 24 hours after intratracheal instillation of 1 nmol siRNA encapsulated into lead (top three) and ML-2 (bottom two) polymer, or C) 1 nmol of pure siRNA. D) Flow cytometric analysis of cell suspension generated from mouse lungs through tissue grinders. E) Cytokine expression measured in BALF samples, normalized to the respective maximum value. F) Tissue slices from mouse lungs treated with ML-2 (top) encapsulating siGAPDH (left) and siNC (right) and lead polymer (bottom) encapsulating siGAPDH (left) and siNC (right).

In order to investigate if the superior properties of ML-2 would translate into an *in vivo* model both polymers were applied to female BALB/c mice intratracheally. Unfortunately, no clear gene knockdown for ML-2 was observed as well as just a slight reduction in gene expression for the Lead polymer (Figure 5. A). This could be associated with the GAPDH housekeeping gene, which plays a crucial role in cell metabolism. A forced downregulation via e.g. siRNA can lead to upregulation of the gene translation as compensation, which is reflected by the observation, that PEI did not mediate a gene downregulation either. Additionally, the loss of efficacy moving from in vitro to in vivo models is not unprecedented. Another reason for this poor in-vitro-in-vivo correlation could be the challenging barriers in intratracheal applications such as the presence of respiratory mucus and the bronchoalveolar architecture. To investigate this hypothesis, we tested the Lead polymer in an air-liquid- interface (ALI) cell culture model of mucus producing CALU-3 cells where a similar loss in efficacy was observed (Figure S15.). This shows that the bronchial mucus forms a major barrier neglected by the machine learning algorithm utilized here. Although the mucus hampers the delivery of the nanoparticles to the lung cells, a considerable retention within the lungs (Figure 4 B) was still observed compared to blank siRNA (Figure 4 C), which was rapidly distributed throughout the entire body. A deeper investigation of the uptake into lung cells through flow cytometry showed that especially the Lead polymer mediates a considerable uptake in most cell types (Figure 4D and Figure S16). For a therapeutic effect, uptake into epithelial and type II pneumocytes, the most relevant and most prevalent cell types, is commonly aimed for. In both cell types, the Lead polymer enabled a superior uptake compared to the ML-2 polymer, but both were increased compared to pure siRNA. A negative correlation between polymer hydrophobicity and mucus penetration might be the reason for the superior uptake for the Lead compared to ML-2 polymer. Since the second optimization task of the algorithm was the toxicity, the in vivo compatibility was investigated next. To exclude false positive results, polymers were tested for endotoxins and confirmed to

be endotoxin free (Figure S17). BALF Cytokines showed partially higher levels after treatment with the Lead polymer than after administration of PEI polyplexes (Figure 4. E and Figure S18). Treatment with the ML-2 polyplexes, on the other side, resulted in comparable cytokine levels as measured after administration of free siRNA or Buffer alone, indicating high biocompatibility. These findings were complemented by the tissue slices prepared from treated lungs, where only for the Lead polymer immune cell invasions were observed, whilst ML-2 was comparable to pure siRNA application (Figure 4 F and Figure S19). These results show the successful improvement of safety and tolerability of the predicted PBAE. One reason could be the more stealth-like properties mediated through the higher hydrophobicity. Especially in macrophages and DCs, the uptake of ML2 was comparable to pure siRNA indicating an evasion of immune recognition, which can also be seen in the low levels of TNF-α, IL-6 and IL-27 (Figure 4 E and F).

## 5. Conclusion

This study demonstrates that machine learning algorithms effectively support optimizing synthesis conditions using well-structured experimental data, even with limited datasets. The successful synthesis of an optimized nanocarrier using model-predicted conditions highlights the value of the Nested-Leave-One-Out Cross Validation approach in guiding experimental design and enabling robust predictions within the defined feature space. Feature analysis was instrumental in enhancing the understanding of the underlying processes. In particular, incorporating stability as an input feature led to improved predictive performance in the GeneExpression model. However, the model's exclusive reliance on *in vitro* data resulted in predictions that did not fully translate to the complexities of *in vivo* environments. Therefore, future research incorporating *in vivo* data from the early stages of optimization is essential to develop more robust and clinically translatable predictive models, ultimately leading to improved therapeutic outcomes.

## 6. Data Availability

All experimental data and the Python code used are available upon request. The data used to fit and validate the Machine Learning models are shown in Figure S20.

## 7. Acknowledgements

This work was supported by ERC-2022-COG-101088587 to O.M.M. and by the German Federal Ministry of Education and Research (BMBF) in the framework of the Cluster4Future program (Cluster for Nucleic Acid Therapeutics Munich, CNATM, Project ID: 03ZU1201AA). Graphics were partially generated using BioRender.

## 8. Supporting Information

**Table S1** adjusted from Zimmermann et al, doi:  $\underline{10.1016/j.jconrel.2022.09.021}$ . Sequences of siRNAs used in the study. Nt = nucleotides; GFP = green fluorescence protein; NC = negative control; GAPDH = housekeeping gene GAPDH; A = Adenine; C = Cytosine; G = Guanine; U = Uracil; T = Thymine; p = phosphate residue; lower case bold letters = 2'-deoxyribonucleotides; capital letters = ribonucleotides; underlined capital letters = 2'-O-methylribonucleotides.

Name	Sense strand (5'-3')	Sense strand (5'-3') Antisense strand (3'-5')		Length (nt)	
			Sense	Antisense	
siGFP	pACCCUGAAGUUCAUCUG	<u>ACU</u> G <u>G</u> G <u>A</u> C <u>U</u> U <u>C</u> A <u>A</u> G <u>U</u> A <u>G</u> A <u>C</u>	25	27	
	CACCACcg	GUGGUGGC			
siNC	pCGUUAAUCGCGUAUAAU	<u>CAGCA</u> A <u>U</u> U <u>A</u> G <u>C</u> G <u>C</u> A <u>U</u> A <u>U</u> U <u>A</u>	25	27	
	ACGCGUat	UGCGCAUAp			
siGAPDH	pGGUCGGAGUCAACGGAU	<u>UUC</u> C <u>A</u> G <u>C</u> C <u>U</u> C <u>A</u> G <u>U</u> U <u>G</u> C <u>C</u> U <u>A</u>	25	27	
	UUGGUCgt	AACCAGCA			
siGAPDH	pAGCAUCUCCCUCACAAU	<u>ACUCGUAGAGGGAGUGUUA</u>	25	27	
(MM)	UUCCAU <b>cc</b> ]	AAGGUAGG			

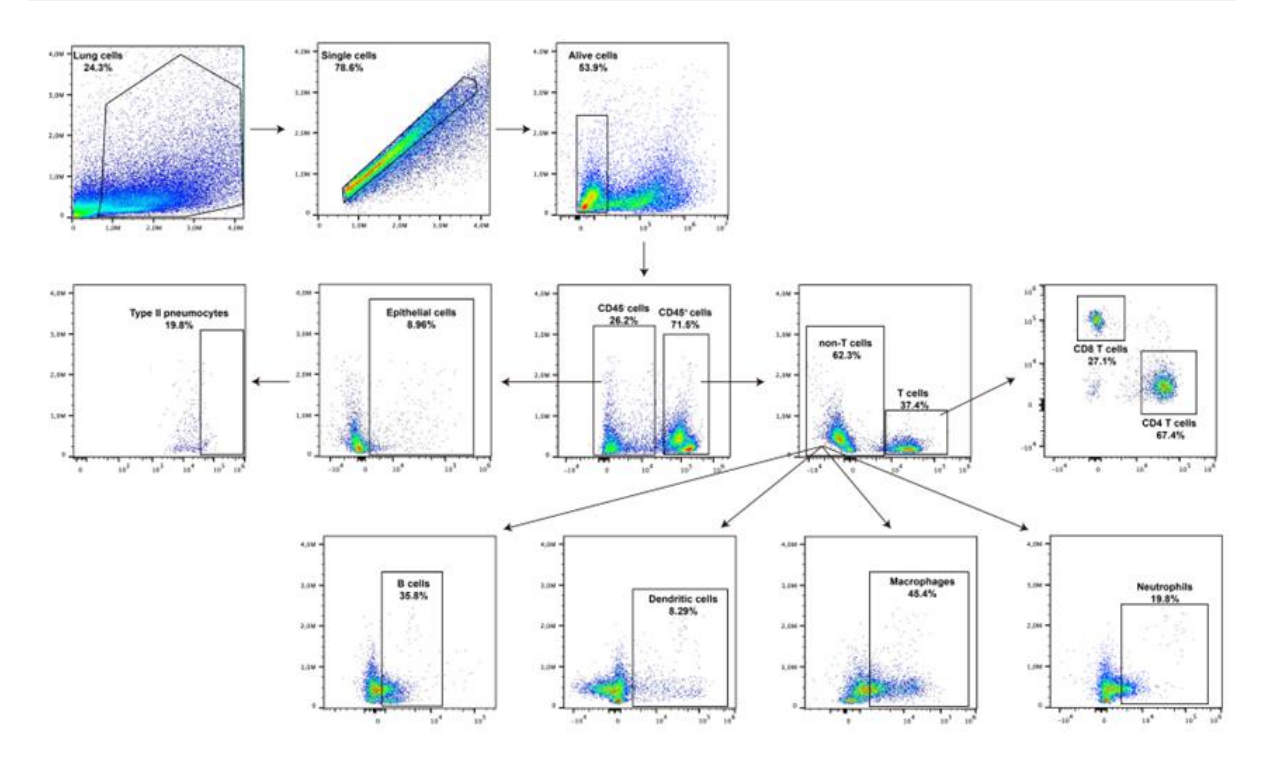


Figure S1. Gating strategy for flow cytometric analysis of single cell suspensions obtained from mouse lungs.

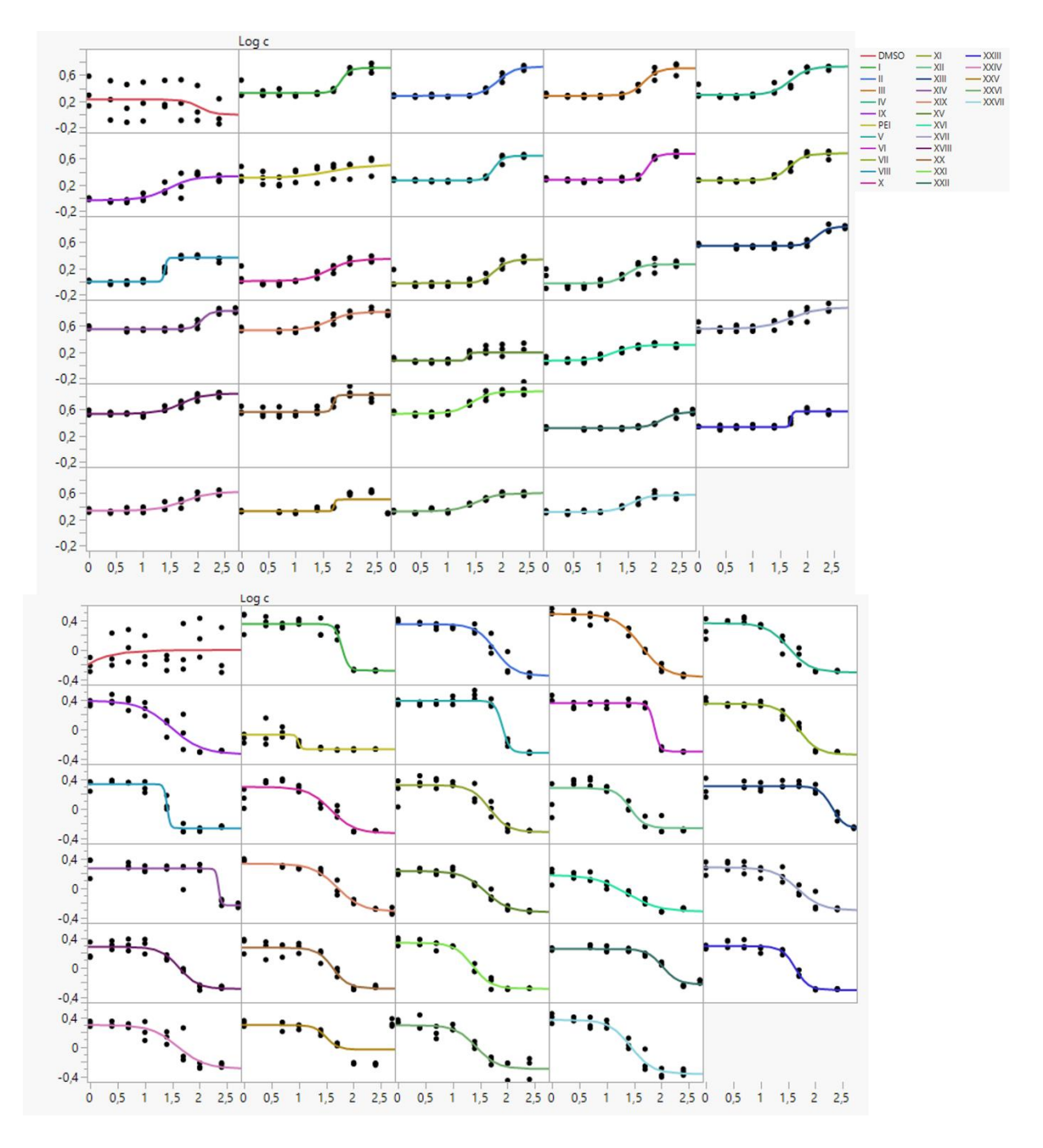


Figure S2. LDH (top) and CTB (bottom) curve fits for polymer library. X-axes depict logarithmic polymer concentration in µg/mL. Each concentration was measured in triplicates.

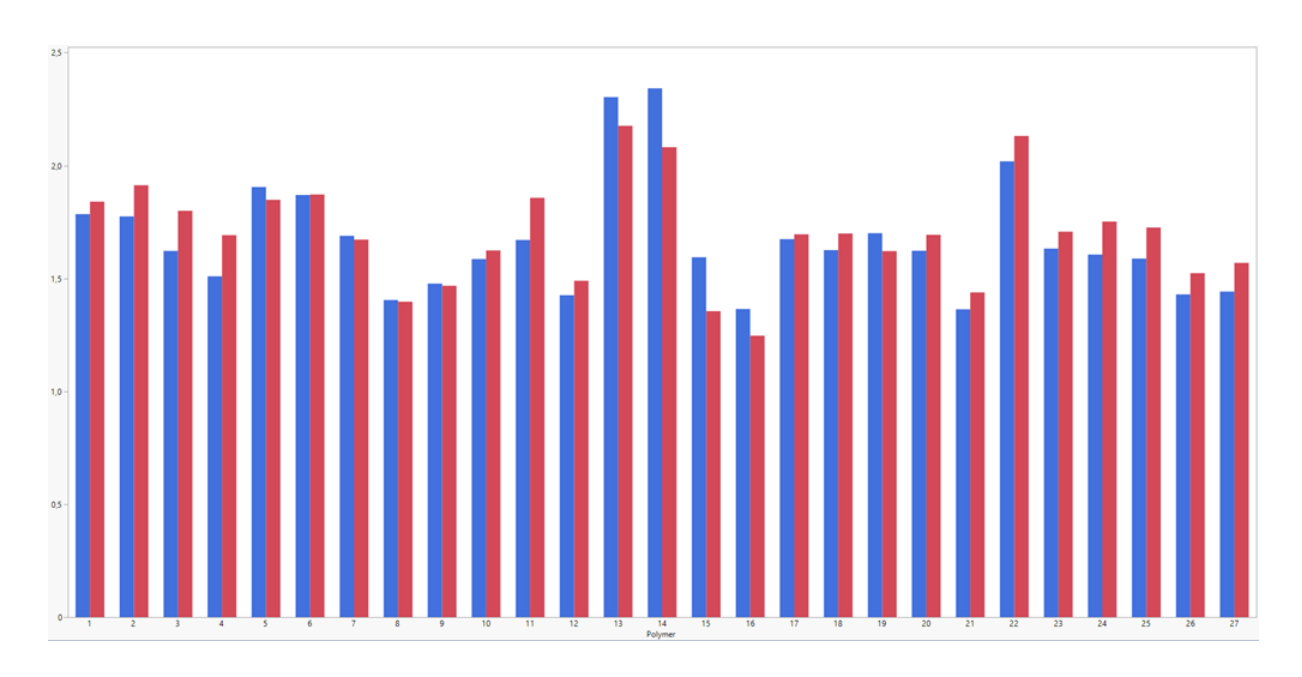
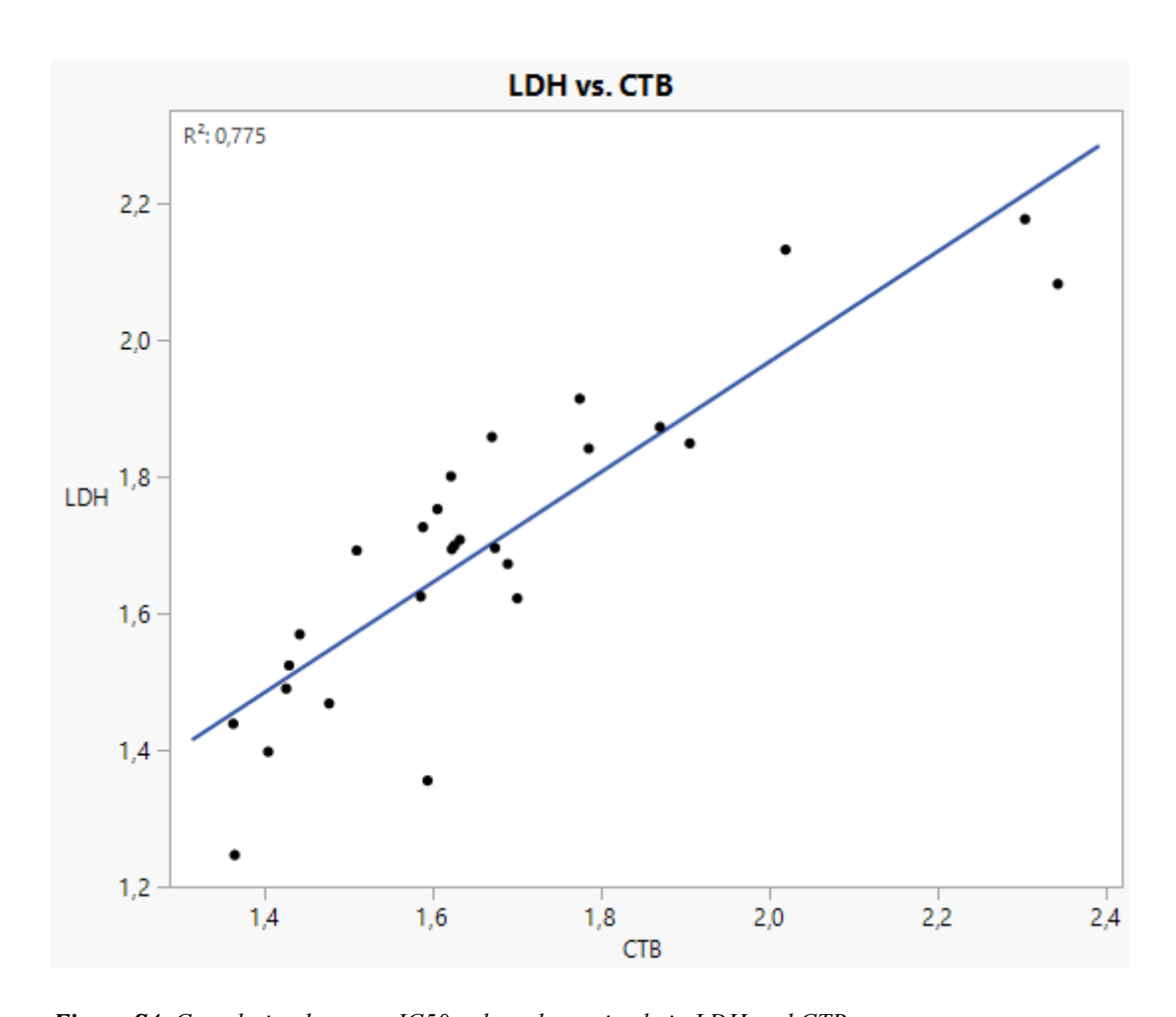


Figure S3. Comparison of CTB (blue) and LDH (red) IC50 values for polymer library.



*Figure S4.* Correlation between IC50 values determined via LDH and CTB.

#### **GeneExpression ZeroShot:**

XGBRegressor( learning\_rate=0.2, max\_bin=None, max\_cat\_threshold=None, max\_cat\_to\_onehot=None, max\_delta\_step=4, max\_depth=4, max\_leaves=None, min\_child\_weight=2.0, missing=nan, monotone constraints=None, n estimators=100)

#### **GeneExpression FewShot:**

SVR(C=1, degree=4, epsilon=0.2, kernel='poly', shrinking=False)

#### IC50 ZeroShot:

RandomForestRegressor(ccp\_alpha=0.005, criterion='absolute\_error', min samples leaf=4, oob score=True)

#### **IC50 FewShot:**

RandomForestRegressor(ccp\_alpha=0, criterion='absolute\_error', min\_samples\_leaf=4, min\_samples\_split=8, oob\_score=True)

Figure S5. Model and Hyperparameter Settings after evaluation



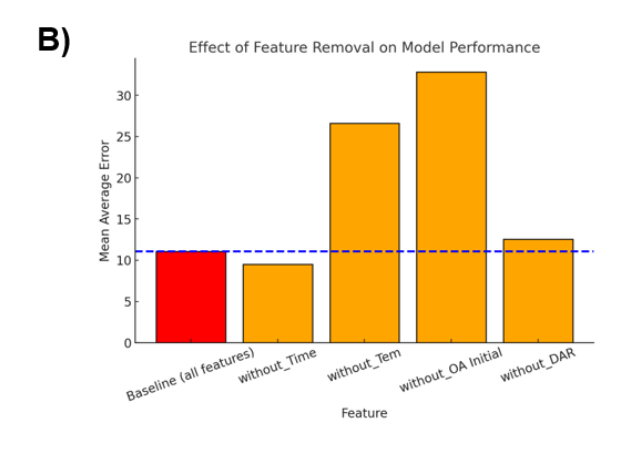






**Figure S6.** Feature ablation study for A) Stability-excluded Gene Expression B) Stability-included Gene Expression C) Stability-excluded IC50 D) Stability-included IC50.

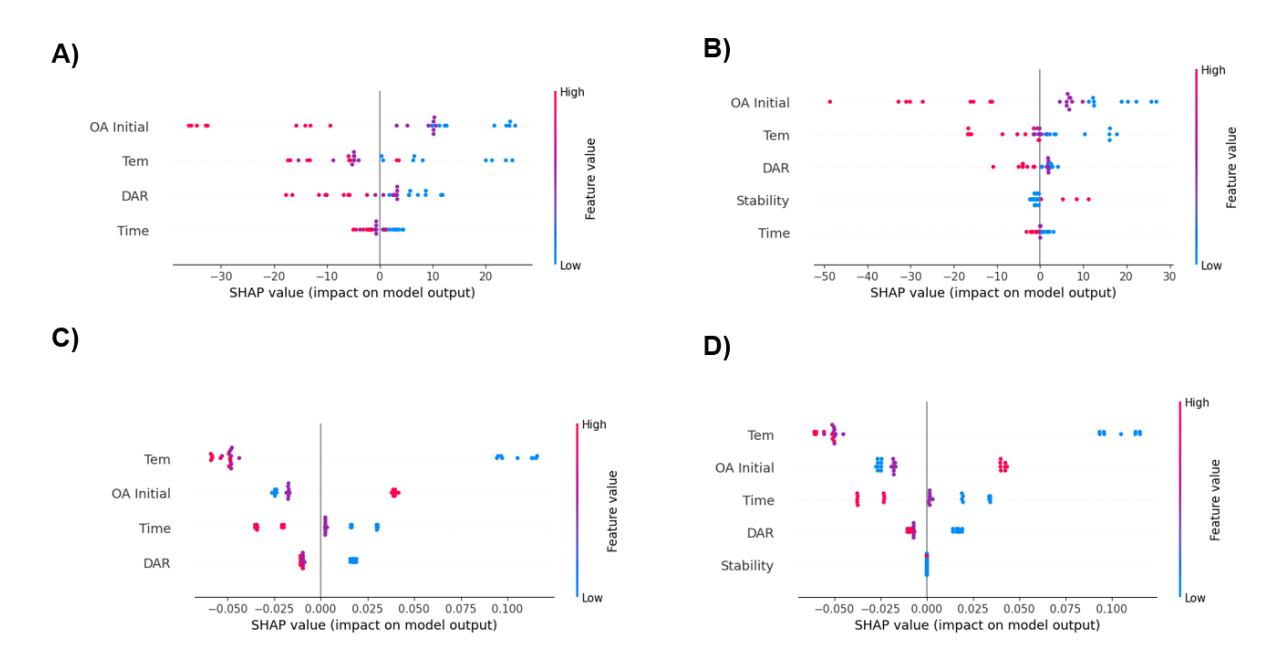


Figure S7. SHAP results with all features A) Stability-excluded Gene Expression B) Stability-included Gene Expression C) Stability-excluded IC50 D) Stability-included IC50.

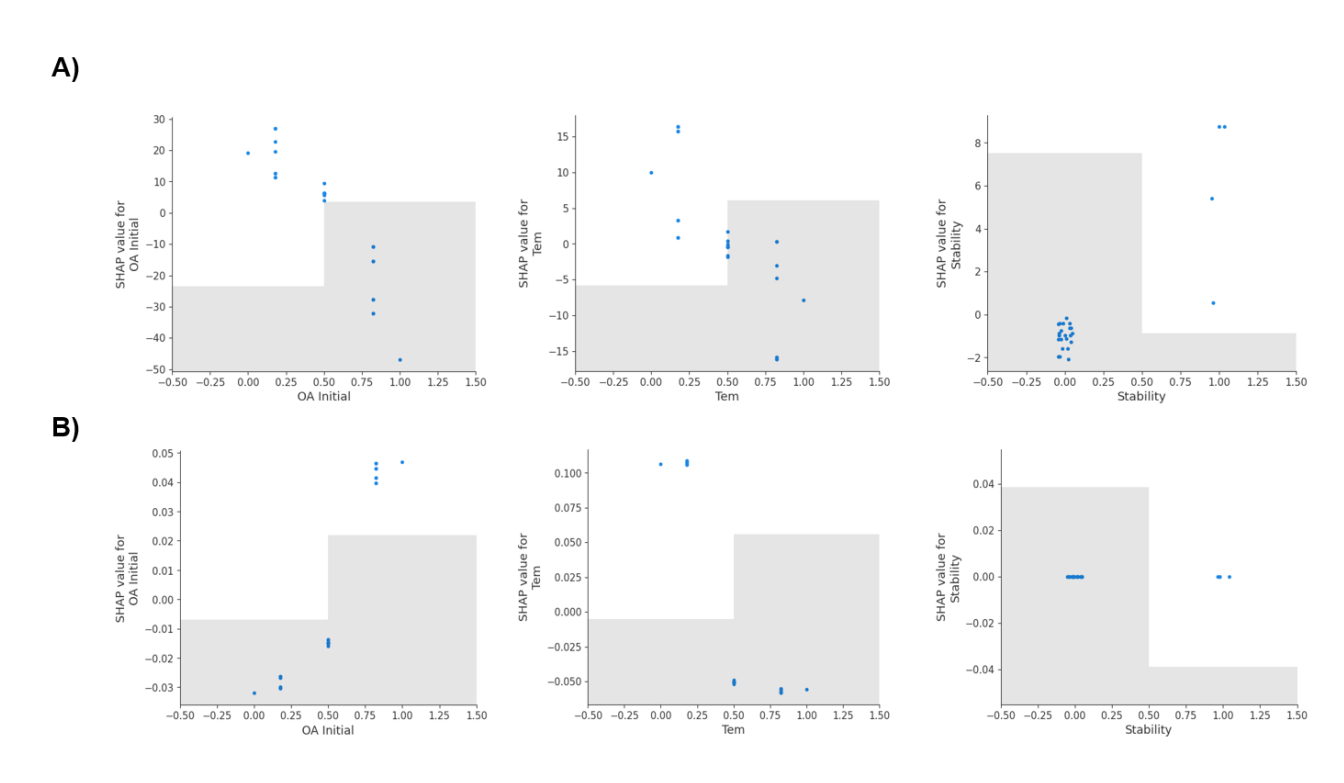


Figure S8. Scatter plots of SHAP values and used features after the feature ablation study for the Stability-excluded model for A) the Gene Expression Model and B) the IC50 Model.

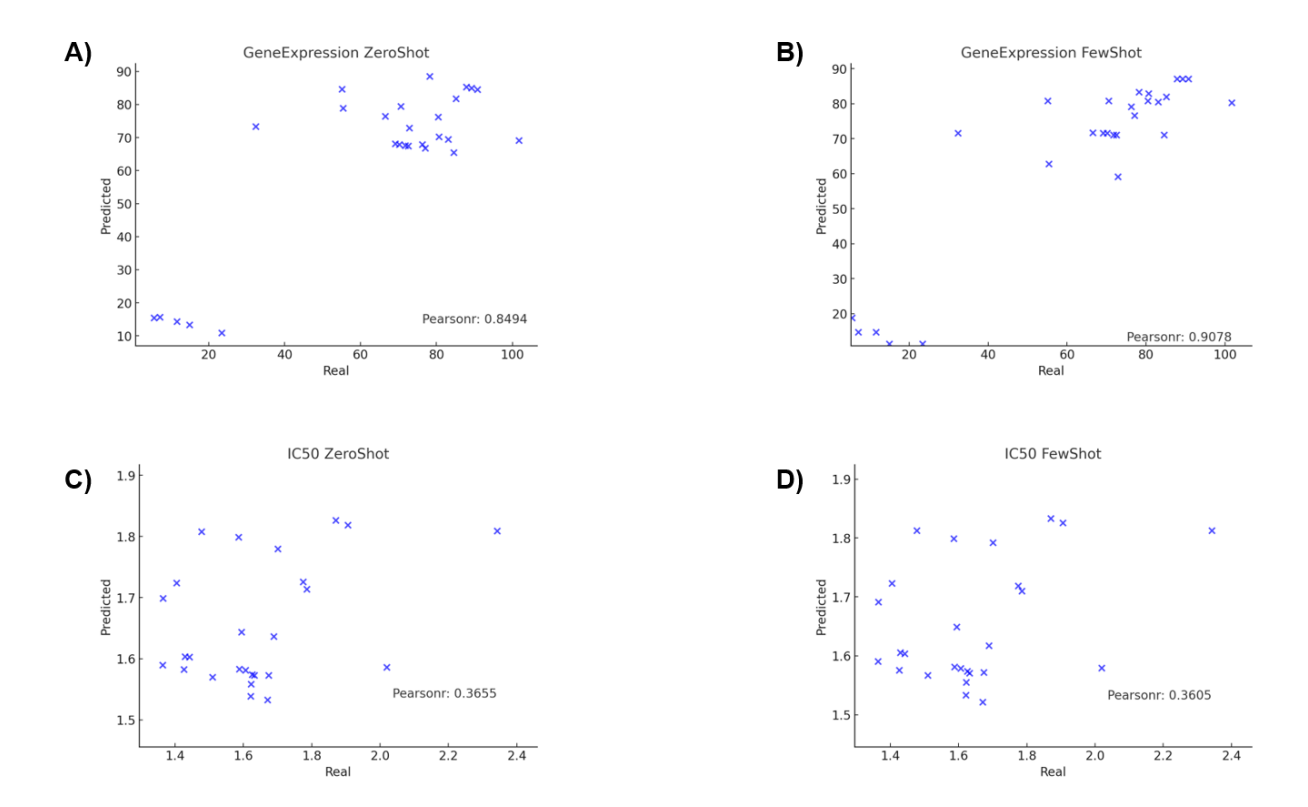
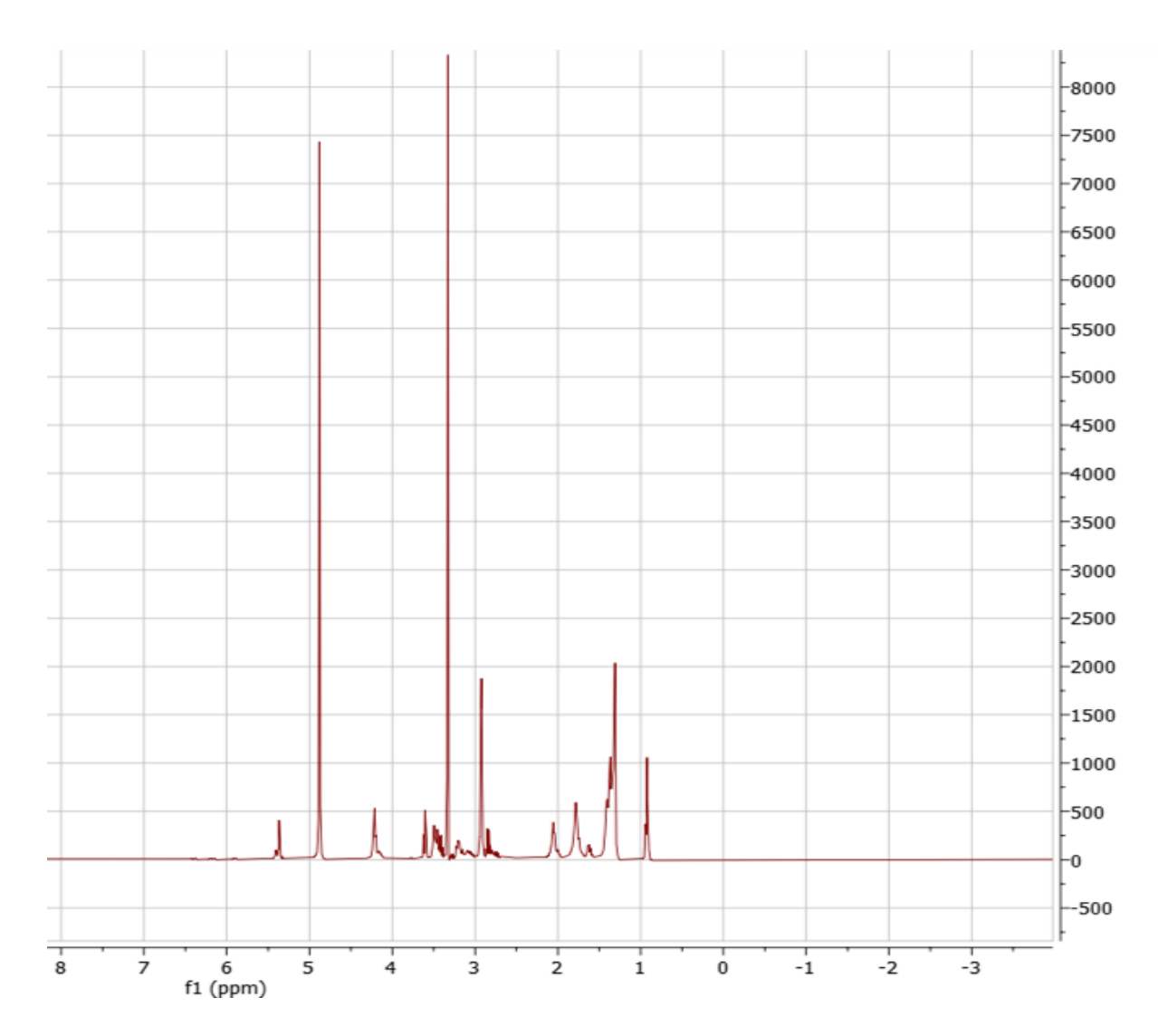


Figure S9. Scatter plots of SHAP values and used features after the feature ablation study for the Stability-excluded model for A) the Gene Expression Model and B) the IC50 Model.



**Figure S10.:** 1H-NMR of the ML-optimized polymer ML-2.

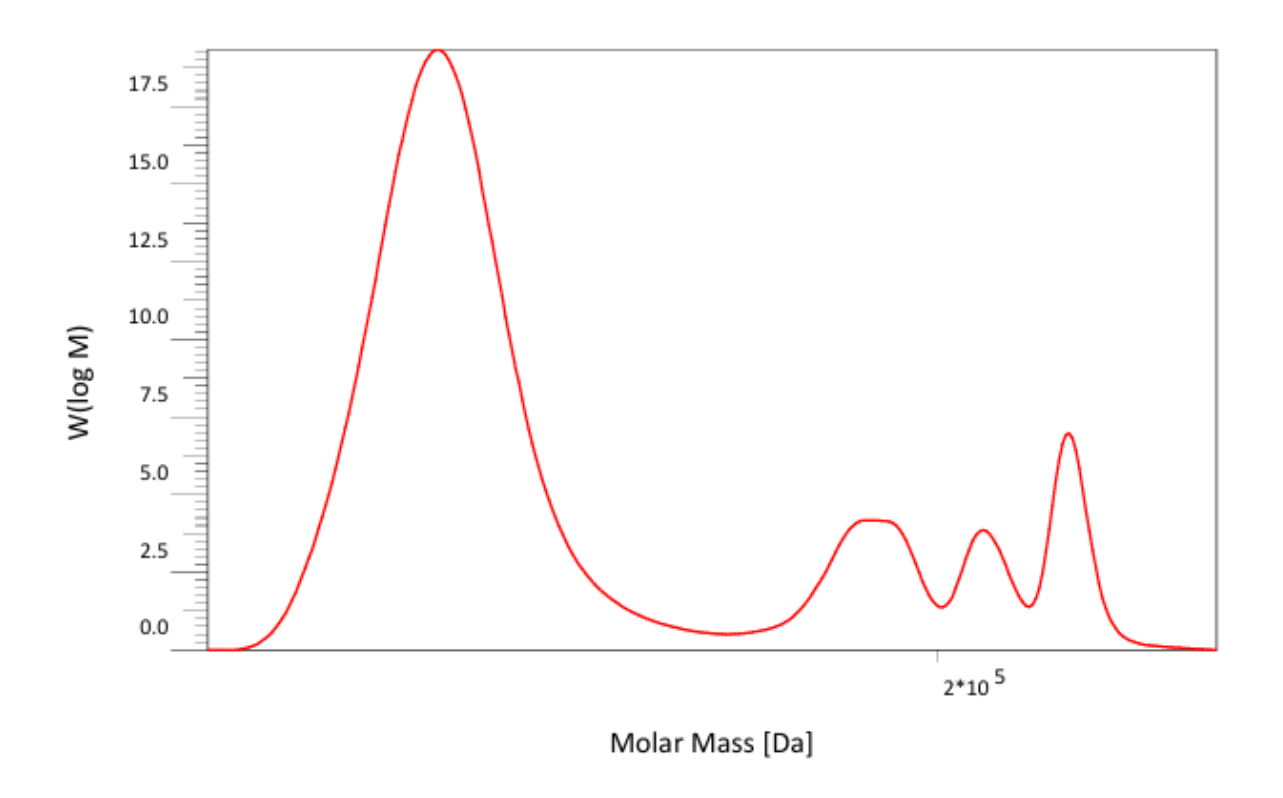


Figure S11. GPC measurement of the ML-optimized polymer ML-2.

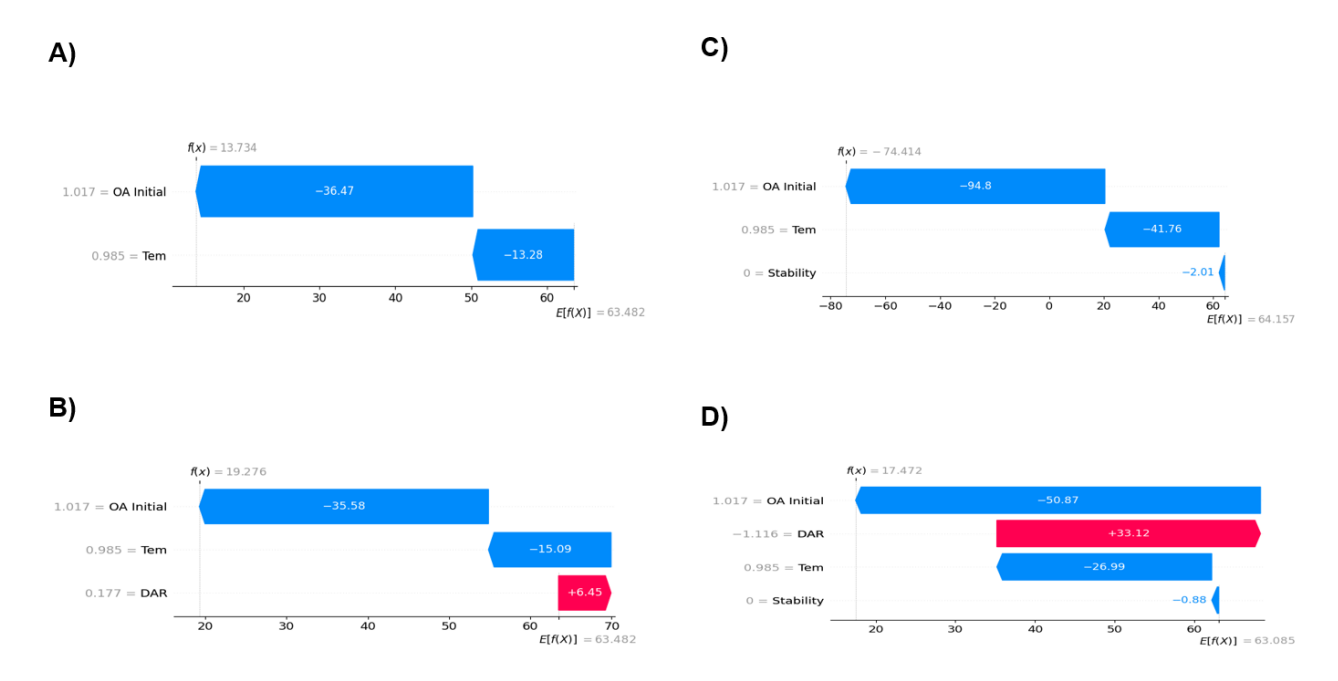
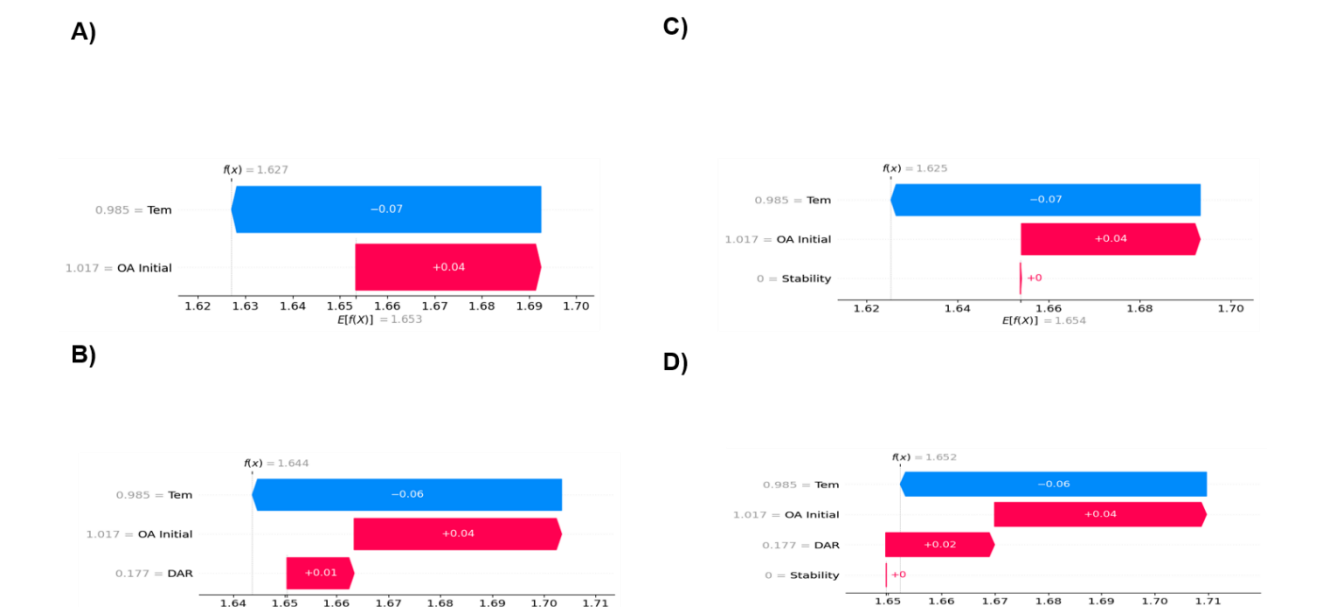


Figure S12. Single Point Prediction of optimized polymer for the Gene Expression Models with A) Stability-excluded after feature ablation B) Stability-excluded before feature ablation C) Stability-included after feature ablation D) Stability-included before feature ablation.



**Figure S13.** Single Point Prediction of optimized polymer for the IC50 Models with A) Stability-excluded after feature ablation B) Stability-excluded before feature ablation C) Stability-included after feature-ablation D) Stability-included before feature ablation.

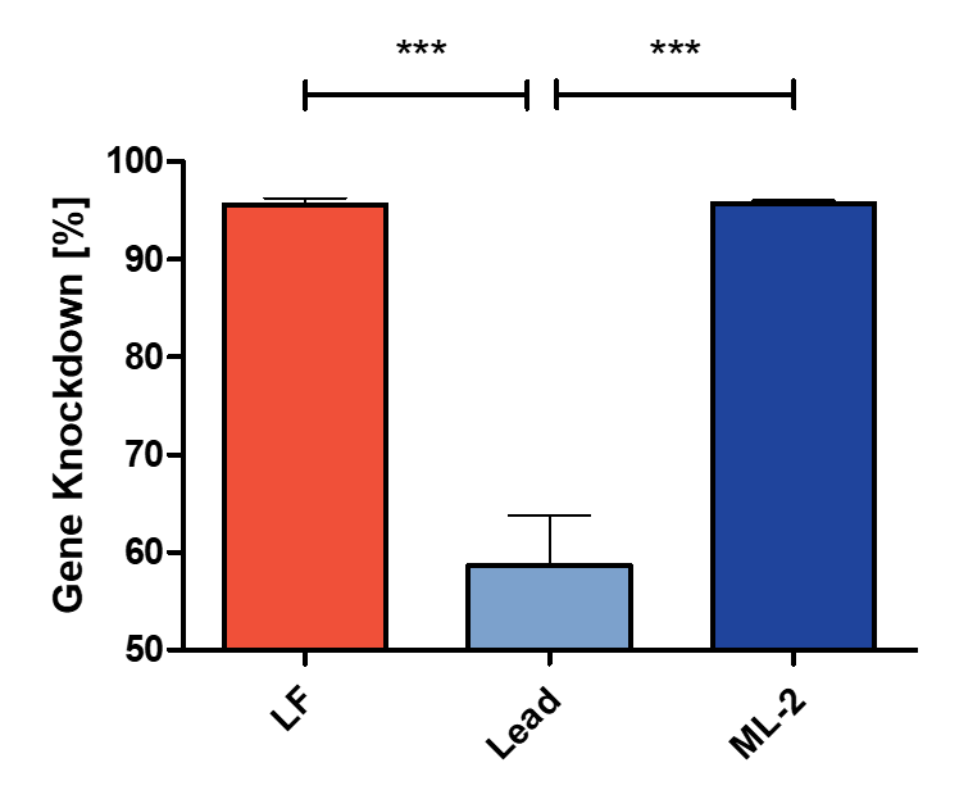


Figure S14. Gene Knockdown calculated from the median fluorescence intensity comparing H1299 eGFP cells treated with pure siGFP (for LF) or nanoparticles encapsulating siNC against siGFP with N=3 (\*\*\* depicting a  $p \le 0.001$ ).

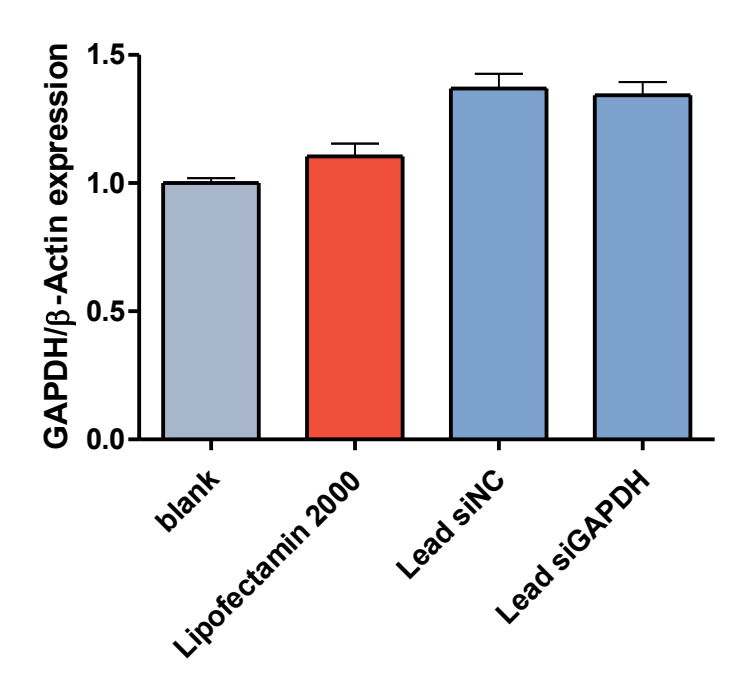


Figure S15. GAPDH gene expression determined via qPCR in air-liquid-interface-cultured CALU-3 cells<sup>27</sup> after treatment with Lipofectamine or Lead polymer encapsulating siNC or siGAPDH. No sequence-dependent significant difference was found (n=3).

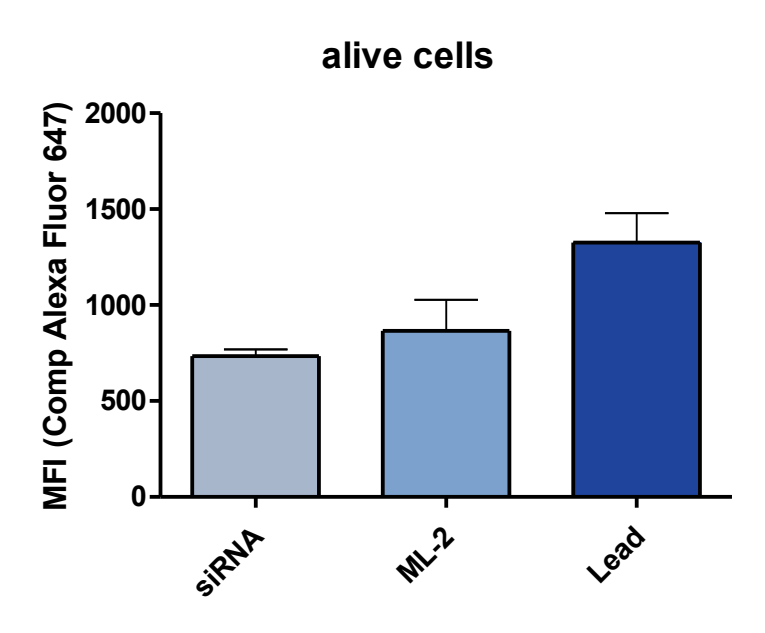
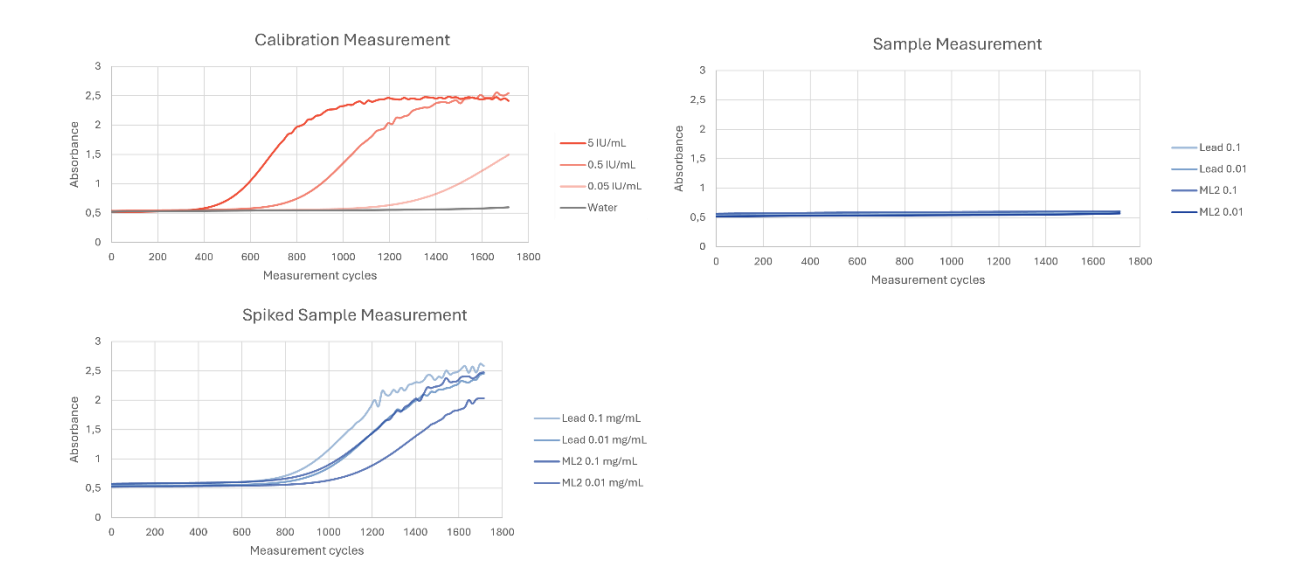


Figure S16. MFI of all alive cells measured from mouse lung single cell suspensions.

#### **Endotoxin test using an LAL-reaction (S)**

To ensure an endotoxin free synthesis product polymers were investigated using the Endosafe® Endochrome-K<sup>TM</sup> Kinetic Chromogenic (KCA) LAL Endotoxin Detection Reagent (Charles River, Sulzfeld, Germany). Briefly, A calibration curve was prepared from the kits reference sample in duplicates in a range from 0.05 to 5 IU/mL. Polymer samples of the lead candidate and ML-2 were prepared in two concentrations of 0.1 and 0.01 mg/mL in duplicates. One sample of each polymer concentration was spiked with endotoxin references to a final concentration of 0.5 I.U./mL, while the other sample was used without any further modification. To 100 mL of the respective samples, 100 μL of freshly resuspended LAL-reagent was added. After 5 minutes of incubation at 37°C, sample absorbance was measured with a plate reader at 374 nm (TECAN Spark, TECAN, Männedorf, Switzerland. At 37°C all samples were measured every 15 seconds at the same seconds for 30 minutes. No increase above an absorbance value of 1 after 30 minutes was interpretated as an Endotoxin Concentration below the LoD for the kit and stated as "Endotoxin-free".



**Figure 17.** LAL Endotoxin Detection results showing the calibration measurement of pure endotoxin standards (left, top), samples spiked with 0.5 IU/mL endotoxin standard (left, bottom) and samples without any modification (right).

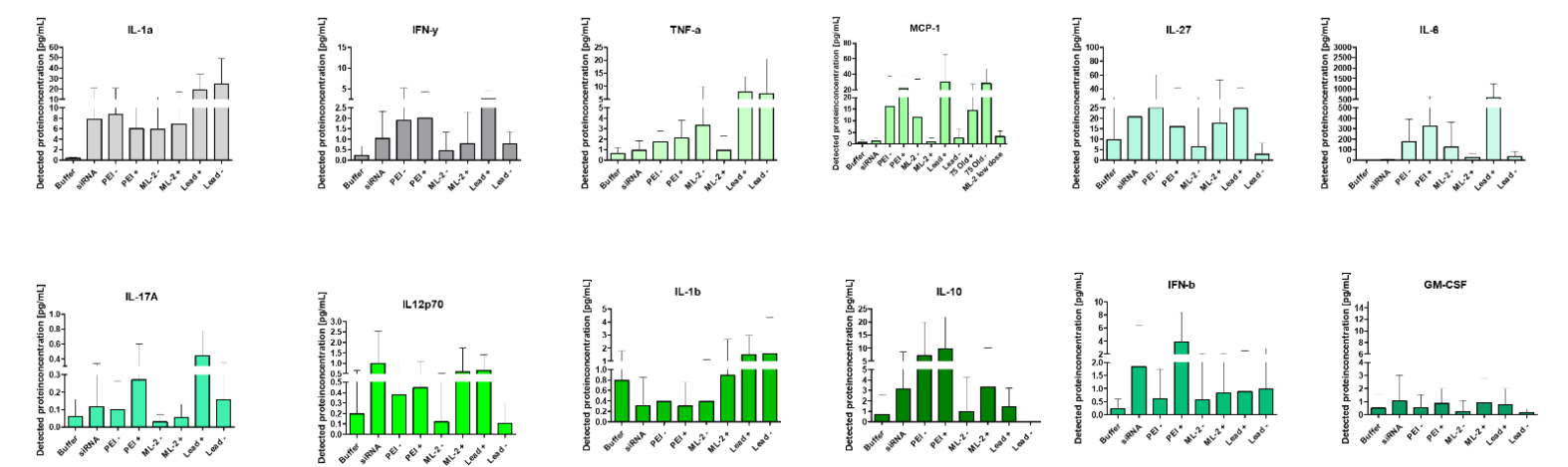


Figure S18. Cytokine quantification from BALF samples using the ELISA Inflammation Panel, reported as pg/mL.

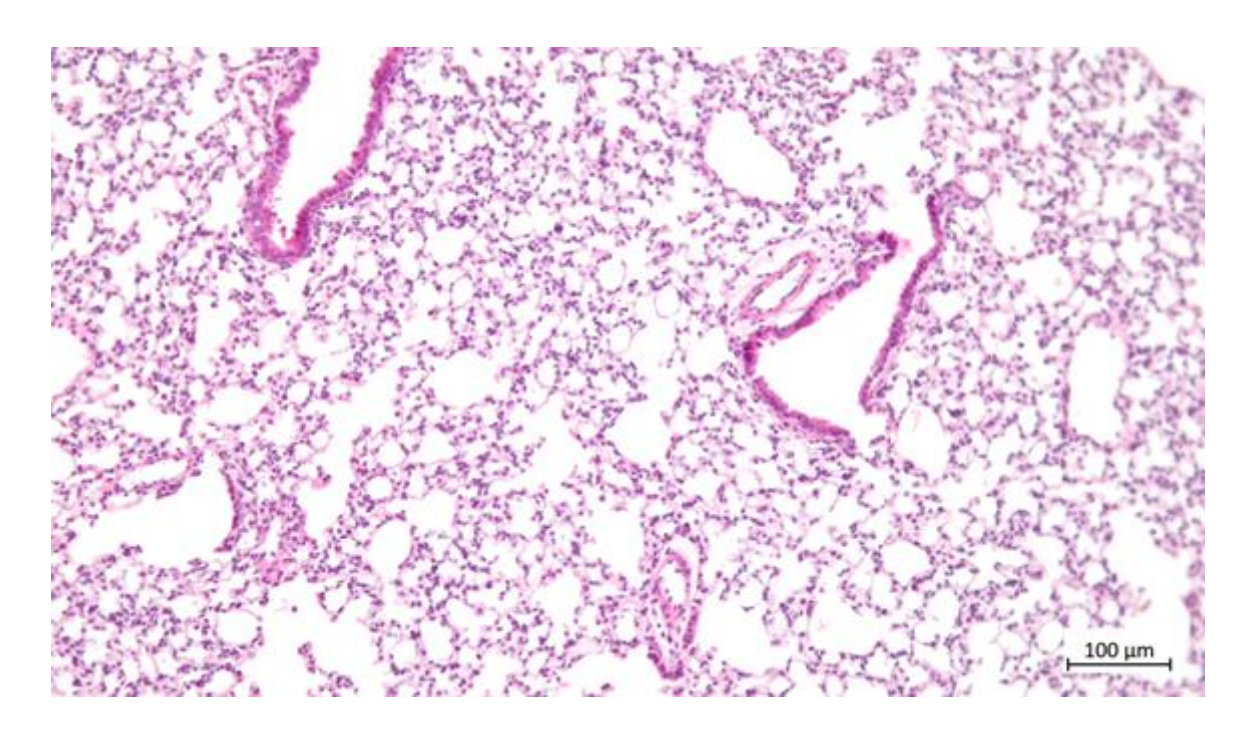


Figure S19. H&E staining of tissue slice obtained from a mouse lung treated with buffer containing only siRNA.

	IC50	Gene Expression	Time	Tem	OA Initial	DAR	Stability
1	1.7852382	101.7104356	24	80	30	0.8	3.081
2	1.7746021	80.44038087	72	80	30	0.8	1.658
3	1.6217206	89.2651216	24	120	30	0.8	2.472
4	1.5098928	78.19409178	72	120	30	0.8	4.54
5	1.9051339	80.67310824	24	80	80	8.0	6.334
6	1.8697649	83.09023816	72	80	80	0.8	5.082
7	1.6891918	23.39141521	24	120	80	0.8	2.077
8	1.4047717	14.92241948	72	120	80	0.8	1.297
9	1.4772239	55.13546155	24	80	30	1.2	2.865
10	1.58588	70.55560858	72	80	30	1.2	1.541
11	1.6703613	90.77038652	24	120	30	1.2	2.091
12	1.426162	87.88885654	72	120	30	1.2	1.166
13	5.4845021	72.88009587	24	80	80	1.2	0.8386
14	2.3420749	55.38145585	72	80	80	1.2	0.6683
15	1.5939827	11.59752057	24	120	80	1.2	0.9769
16	1.365078	7.089913749	72	120	80	1.2	0.777
17	1.6740007	71.7624657	10.879	100	55	1	1.53
18	1.6260081	70.18627262	85.121	100	55	1	2.577
19	1.7004153	76.28641928	48	69.0658	55	1	1.653
20	1.6227475	66.53691612	48	130.934	55	1	1.309
21	1.3633572	85.11179583	48	100	16.3323	1	1.988
22	2.0188706	5.542691159	48	100	93.6677	1	1.476
23	1.6323142	84.54612458	48	100	55	0.690658	2.992
24	1.6056775	32.33477785	48	100	55	1.30934	1.847
25	1.5884922	72.50527997	48	100	55	1	1.763
26	1.429609	69.13573695	48	100	55	1	1.775
27	1.4422226	77.07529989	48	100	55	1	7.58

Figure S20. Data for Machine Learning Model fitting and validation: Labels (green); synthesis parameters (light blue, features); and stability data (dark blue).

# V. Nebulization of RNA-Loaded Micelle-Embedded Polyplexes as a Potential Treatment of Idiopathic Pulmonary Fibrosis

This Chapter was published in ACS Applied Materials & Interfaces:

Müller, J.T.; Kromer, A. P. E.; Ezaddoustdar, A.; Alexopoulos, I.; Katharina M. Steinegger, K.M.; Porras-Gonzalez, D.L.; Berninghausen, O.; Beckmann, R.; Braubach, P.; Burgstaller, G.; Wygrecka, M.; Merkel, O.M. Nebulization of RNA-Loaded Micelle-Embedded Polyplexes as a Potential Treatment of Idiopathic Pulmonary Fibrosis ACS Appl. Mater. Interfaces 2025, 17, 8, 11861–11872

The Contribution to this chapter consisted in the synthesis of used polymers, preparation and physicochemical characterization of nanoparticles as well as the *in vitro* performance evaluation.

## 1. Abstract

Biodegradable poly( $\beta$ -aminoesters) (PBAEs) have been a focus of interest for delivering therapeutic siRNA for several years. While no approved therapies are on the market yet, our study aims to advance PBAE-based treatments for currently "undruggable" diseases. The PBAEs used in this study are based on a recently reported step-growth copolymerisation, which results in polymers with a unique balance of lipophilicity and positive charge, thereby showcasing diverse properties.

Upon incubation with siRNA, these PBAEs form a unique structure and topology, which we classify as a subtype of classical polyplexes, termed "micelle-embedded polyplexes" (mPolyplexes). The impact of different nebulisers on the physicochemical performance of these nanoparticles were investigated, and it was found that various mPolyplexes can be nebulised using Vibrating-Mesh Nebulisers (VMNs) without loss of gene silencing activity nor change in physicochemical properties, setting them apart from other nanoparticles such as marketed LNPs.

Finally, their therapeutic application was tested *ex vivo* in human precision cut lung slices (PCLS) from patients with lung fibrosis. mPolyplexes mediated 52% gene silencing of matrix metalloprotease 7 (MMP7) and a downstream effect on Collagen I (Col I) with a 33% downregulation as determined via qPCR.

## 2. Introduction

The lung offers numerous advantages for local administration over systemic administration, particularly when treating diseases that originate in the lung. This non-invasive approach is generally more comfortable for patients than parenteral administration. It is essential to distinguish whether the treatment is intended for local or systemic effects; in the former case, the drug should remain in the lungs for as long as possible to maximise its effectiveness and minimise side effects. Furthermore, this approach ensures direct delivery to the target tissue and cells, while reduced protein concentration in the lungs minimises adsorption effects that can lead to unpredictable changes in cellular uptake<sup>119</sup>. Reduced overall protein concentration typically correlates with reduced nuclease concentration in the lungs, enhancing RNA stability for pulmonary delivery<sup>120</sup>.

This study focuses on the treatment of idiopathic pulmonary fibrosis (IPF), a lung disease, which would clearly benefit from a local therapeutic approach. Small interfering RNA (siRNA) presents a promising method for downregulating mRNA associated with the disease utilising the cell's own machinery. While ONPATTRO®, the first siRNA drug, was approved in 2018, no siRNA-based therapies have so far been approved for pulmonary application. However, numerous studies are currently underway targeting extrahepatic application, reflecting a growing interest in this research area<sup>121</sup>. For the encapsulation of negatively charged siRNA molecules using non-viral carriers, a variety of materials and nanoparticles are available, including lipid nanoparticles (LNPs), lipoplexes, polyplexes, micelleplexes, lipid-polymer hybrid nanoparticles, gold nanoparticles and others. Our group specialises in biodegradable and biocompatible poly( $\beta$ -aminoesters) (PBAEs), which irregularly alternate with spermine side chains for RNA-encapsulating and oleylamine side chains for hydrophobicity and fusogenicity<sup>75,109</sup>.

To produce an inhalable formulation from aqueous solutions, different nebulisation devices are available. Besides air-jet and ultrasonic nebulisers, vibrating mesh nebulisers (VMN) are the most recently developed technology. VMNs nebulise aqueous suspensions via extrusion through a thin vibrating perforated membrane driven by piezoelectric crystals. Given that siRNA is an expensive and highly shear and heat sensitive material, it is essential to nebulise this active pharmaceutical ingredient (API) through the least stress-inducing nebuliser device. VMNs are suitable for this purpose due to their low dead volume, heat resistance and low shear stress. Unsurprisingly, most current clinical trials of siRNA inhalation utilise VMNs<sup>122</sup>.

Here, we will evaluate two VMNs, the Aerogen Pro and the PARI eFlow® Rapid, for their suitability in nebulising PBAE-based drug delivery systems. Kleeman et al. described that VMNs are preferable to air-jet nebulisers for liposomal formulations due to lower shear stress<sup>123</sup>. VMNs also exert less thermal load, as the energy required for nebulisation is introduced through the vibrating mesh rather than directly into the solution. Other researchers also identified VMNs as the best option for surface-active substances, as they maintained constant drug output<sup>124</sup>. However, the PARI eFlow® Rapid caused a temperature increase of over 10°C, as shown by Hertel et al., which is noticeably higher than the temperature increase of 3.2°C for the Aerogen Pro<sup>51</sup>. Nevertheless, the same study demonstrated that active cooling prevented any temperature rise for over four minutes for the PARI eFlow® Rapid. Furthermore, VMNs were shown to preserve the aerodynamic properties of reconstituted, freeze-dried nanoparticle suspensions during nebulisation<sup>125</sup>. Unlike air-jet and ultrasonic nebulisers, which left most resuspended nanoparticles in the reservoir, VMNs did not. As a result, VMNs are recommended for "sensitive" formulations, including nanoparticle suspensions. Patel et al. further demonstrated that PBAE nanoparticles remain stable during nebulisation with an Aerogen VMN, as evidenced by both dynamic light scattering (DLS) and electron microscopy (EM), and resulting in uniform distribution across all five lung lobes after nebulisation in vivo<sup>56</sup>. IPF is clinically characterised by exertional dyspnoea, dry cough, and often auscultatory findings, with a poor median survival of 3-5 years 126,127. IPF pathogenesis is still poorly understood, but the prevailing theory involves repeated microinjuries to a genetically predisposed alveolar epithelium, followed by activation of fibroblasts, their transdifferentiation into collagen-producing myofibroblasts, and finally excessive extracellular matrix (ECM) deposition in the lungs<sup>128</sup>. This process impairs gas exchange and lung function. The accumulation of ECM and Col I, a key component of fibrotic ECM, creates a diffusive barrier that complicates treatment – a hallmark of all interstitial lung diseases. Interestingly, Jacquemart et al. demonstrated that hydrophobic materials exhibit stronger adsorption to Col I than more hydrophilic ones, a factor that could influence the effectiveness and penetration of PBAEformulation through collagen deposits in treating IPF<sup>129,130</sup>.

With IPF's unclear aetiology, recent research has focused on identifying both genetic factors involved in the disease development and biomarkers with predictive, diagnostic, or prognostic value<sup>128</sup>. The only approved drugs for IPF, pirfenidone and nintedanib, have limited efficacy in reducing mortality, merely slowing disease progression through pleiotropic effects such as reducing inflammation and inhibiting fibroblast proliferation and ECM production<sup>131</sup>. Consequently, IPF is currently considered an "undruggable" disease, making it a prime

candidate for siRNA-based interventions, which are commonly more target specific than small molecule drugs.

MMP7, a zinc-dependent endopeptidase, has been consistently identified as one of the most upregulated genes in the lungs of patients with various forms of progressive pulmonary fibrosis, including IPF<sup>131</sup>. Primarily expressed in lung epithelial cells, MMP7 (also known as *matrilysin*), contributes to IPF progression via the WNT/β-catenin pathways. Following the dephosphorylation of β-catenin, transcription factors are activated<sup>126</sup>, resulting in the transactivation of MMP7 and triggering downstream disease-promoting effects: MMP7 facilitates epithelial-to-mesenchymal cell transdifferentiation and increases pro-fibrotic mediators through regulation of PKA and ERK1/2 signalling, ultimately leading to an overexpression of collagen I<sup>132,133</sup>. Elevated MMP7 levels have been found in lung tissue, bronchoalveolar lavage fluid (BALF), and peripheral blood of IPF patients, with higher blood levels predicting increased mortality risk<sup>134</sup>. Notably, *in vivo* studies also suggests MMP7's central role, as MMP7'- mice were protected against bleomycin-induced IPF<sup>135</sup>. Arrowhead Pharmaceuticals is currently conducting a clinical trial on inhaled siRNA targeting MMP7, underscoring its potential therapeutic application<sup>121</sup>.

The aim of this project is the development of an inhalable siRNA formulation for MMP7 downregulation. This aim was pursued by synthesizing various PBAEs with differing oleylamine (OA) content and forming mPolyplexes by adding siRNA. Additionally, the impact of nebulisation using VMNs on the stability and performance of these complexes was investigated, followed by testing in a relevant *ex vivo* model to downregulate the therapeutic target MMP7 using RNA interference (RNAi).

## 3. Materials and Methods

#### **Materials**

Dicer substrate double-stranded siRNA targeting enhanced green fluorescent protein (eGFP) (siGFP, 25/27mer), amine-modified Dicer substrate double-stranded siRNA targeting enhanced green fluorescent protein (25/27mer) and scrambled siRNA (siNC, 25/27mer) were purchased from IDT (Integrated Technologies, Inc., Leuven, Belgium), sequences and additional information are given in Supplementary Table S1. HEPES (4-(2-hydroxyethyl)-1piperanzineethanesulfonic acid), Tris-EDTA buffer solution 100X, RPMI-1640 Medium, Triton-X-100®, Heparin sodium salt from porcine intestinal mucosa, heat inactivated Fetal Bovine Serum (FBS), Penicillin/Streptomycin solution (P/S), Geneticin (G418), Dulbecco's Phosphate Buffered Saline (PBS) and branched polyethylenimine (PEI) (5 kDa, Lupasol® G 100) were obtained from Sigma Aldrich (Darmstadt, Germany). Ditert-butyl decarbonate, Oleylamine, Spermine, Lipofectamine 2000, OPTI-MEM Serum Reduced Medium, 0.05% Trypsin-EDTA, Alexa Fluor 647 NHS Ester, SYBR Gold Nucleic Acid Gel Stain 10.000X concentrate in DMSO and siMMP7 were purchased from ThermoFisher Scientific (Schwerte, Germany). 1,4-butanendiol diacrylate was obtained from TCI Chemical Industry Co., Ltd. (Tokyo, Japan). Trifluoroacetic acid (99,9%, extra pure) was purchased from Acros Organics (Geel, Belgium).

#### **Polymer synthesis**

PBAE copolymers were synthesised applying a well characterised synthesis approach previously reported by our group<sup>109</sup>. Briefly, the reaction is composed of a diacrylate monomer forming the backbone of the polymer and two side-chain forming primary amines in different ratios. We applied 1,4-butandiol diacrylate as backbone and tri-boc-spermine (TBS) together with OA in different ratios. All educts were dissolved in a concentration of 300 mg/mL in DMF. After the reaction time, polymers were deprotected using trifluoro acetic acid. The deprotected polymers were precipitated three times in pentane before final drying. Monomer ratios (stated forthgoing as the percentage of OA in the final polymer) were estimated by <sup>1</sup>H-NMR spectroscopy.

#### Particle preparation

Particles were prepared using a batch mixing approach. Briefly, siRNA and polymer solutions were prepared and mixed in equivalent volumes of 10 mM HEPES at pH 5.4. Polymer concentrations varied between each polymer, and siRNA solutions were prepared in a concentration of 500 nM. PBAE or PEI were mixed to the siRNA solution by rapid pipetting

for a defined speed and time. PBAE or PEI solutions were prepared at concentrations resulting in a 10-fold excess of protonated amines in used polymer over phosphate groups in the siRNA backbone (N/P ratio of 10) following equations 1 and 2.

$$\frac{N}{P} = \frac{m_{(Polymer)}}{n_{(siRNA)*} n_{(Nucleotides)*} M_{(Protonable Unit)}}$$
(Eq. 1)

$$M_{(Protonable\ Unit)} = \frac{(m_{(OA)} * r_{(OA)}) + (m_{(Spermine)} * r_{(Spermine)})}{(n_{(OA\ amines)} * r_{(OA)}) + (n_{(Spermine\ amines)} * r_{(Spermine)})}$$
(Eq. 2)

Where  $m_{(Polymer)}$  describes the mass of used polymer,  $n_{(siRNA)}$  describes the molar amount of applied siRNA,  $n_{(Nucleotides)}$  is the molar amount of nucleotides in the used siRNA sequence,  $r_{(OA/Spermine)}$  gives the relative ratio of either OA or Spermine in the used polymer, and  $n_{(OA/Spermine amines)}$  refers to the total number of protonable amines in the respective unit. After mixing, solutions were incubated at room temperature for 90 minutes for mPolyplexes (PBAE) and 30 minutes for polyplexes (PEI).

#### Nebulisation

Two commercially available nebulisers were utilised for this study; a PARI eFlow Rapid (PARI, Starnberg, Germany) and an Aerogen Pro (Aerogen, Ratingen, Germany). Each nanoparticle suspension was immediately nebulised after the incubation time ended. Samples were loaded in the corresponding reservoirs, and aerosols were collected in cooled 15 mL falcon tubes for further analysis. A minimum volume of 600  $\mu$ L was applied to the Aerogen Pro and at least 1000  $\mu$ L was added to the PARI eFlow Rapid for each nebulisation.

#### Particle characterisation

Hydrodynamic diameter and polydispersity index (PDI) of nanoparticles were determined by dynamic light scattering (DLS), and  $\zeta$ -potential was determined by phase analysis light scattering (PALS) applying a Zetasizer Advance Ultra (Malvern Instruments Inc., Malvern, UK) at 173° backscatter mode. Nanoparticles were measured in formulation triplicates (N=3) and analysed using the ZS Xplorer software (v.3.2.0). Additionally, nanoparticle tracking analysis (NTA) was applied using a NanoSight NS300 (Malvern Instruments Inc., Malvern, UK) to support DLS data and get more information regarding particle concentration. All results are reported as the mean size (nm)  $\pm$  standard deviation (SD). Results were further validated using cryogenic transmission electron microscopy (cryoTEM) of nanoparticle suspensions before and after nebulisation.

#### RNA encapsulation and stability assay

RNA encapsulation efficiency was determined using a modified SYBR Gold assay, comparable to a previously described method<sup>136</sup>. Briefly, nanoparticles were prepared as described above and splitted before being partially subjected to nebulisation. The collected samples were diluted with RNase-free water to obtain the same siRNA concentration as in the RNA stability test. Formulations were transferred to a fluotrac 384 well plate (Greiner Bio-One, Frickenhausen, Germany) and incubated for 1 hour at 37°C under shaking. Per sample, 3 µL of 4X SYBR Gold Nucleic Acid Gel Stain was added and incubated for 5 minutes under light exclusion. Encapsulation efficiency was determined in comparison to a sample with siRNA only (nonnebulised), which represents 100% free siRNA. To evaluate potential losses of RNA through nebulisation, a newly developed particle disruption approach was applied. Nanoparticles encapsulating 10 pmol siRNA were prepared as described above and subjected to nebulisation. Formulations were transferred to a fluotrac 384 well plate. Per formulation, 10 µL of a 2% Triton-X detergent solution and 2 µL of a 2000 U/mL heparin solution were added and incubated for 1 hour at 37°C under shaking. Subsequently, 3 µL of 4X SYBR Gold Nucleic Acid Gel Stain were added and incubated for 5 minutes under light exclusion. A sample containing free siRNA only was subjected to the same conditions and represents 100% free siRNA. Following incubation, fluorescence measurements were conducted on a microplate reader (TECAN Spark, TECAN, Männedorf, Switzerland) at excitation wavelength 492/20 nm and emission wavelength 537/20 nm. The results are expressed as a percentage of free siRNA ± standard deviation (SD). Technical triplicates (n=3) of formulation triplicates (N=3) were utilised for the measurements.

#### **Molecular dynamics simulations**

Molecular Dynamics (MD) simulations were run in Gromacs 2021.4 applying the Martini 3 force field as previously described<sup>137</sup>. The siRNA was adapted from the model introduced previously for the Martini 2 force field, whereas polymers were newly parametrised based on an All-Atom model<sup>137</sup>.

Simulations contain 15 siRNA molecules and the respective polymer at an N/P ratio of 10, randomly inserted at initial setup. The box size is (40 nm), molecules are solvated with 10 mM HEPES pH 5.4.

#### Aerosol characterisation by laser diffraction

Aerosol characterisation was evaluated applying laser diffraction analysis. Particles were prepared as described above and nebulised with the two respective VMNs into the laser diffractor (HELOS, Sympatec, Clausthal-Zellerfeld, Germany) with an equipped R2 lens and

INHALER module. Aerosol was applied through a punched silicone mouthpiece using a Aerogen Pro T-piece placed approximately 50-100 mm before entering the laser beam. The whole experimental set-up was carried out in a closed plexiglass box to control the relative humidity (% RH), which was kept over 70% RH during analysis. Aerosol was extracted with a rate of 13.9 L/min to avoid re-entry of aerosol to the laser beam. Each measurement consisted of 3 repeated runs with a duration of 5 seconds and a signal integration time of 200 ms. Measurements were carried out in triplicates (n=3). Results are given as Q3 volume median diameter (Q3-VMD)  $\pm$  SD of nebulised droplets following Mie-theory suitable for nebulised droplets, calculated as aqueous buffer with corresponding complex refractive indices.

#### In vitro protein knockdown in H1299-eGFP cells

H1299 cells stably expressing eGFP (H1299-eGFP) were used to determine the in vitro performance of the different nanoparticle systems. H1299-eGFP were cultured in RPMI 1640 medium supplemented with 10% FBS, 1% P/S and 0.4% G418. Cells were routinely cultured and passaged when reaching a confluency of 80-90% with 0.05% (v/v) trypsin and maintained at all times in humidified air with 5% CO<sub>2</sub> at a temperature of 37°C. For experiments, cells were seeded at a density of 8 x  $10^3$  cells/well in 500  $\mu$ L of culture medium in 24 well plates and incubated for 24 h. Subsequently, medium was exchanged and transfection was performed by adding 100 µL of transfection medium. Transfection medium consisted of nanoparticle suspensions encapsulating 50 pmol siRNA either in nebulised or non-nebulised form, 10 mM HEPES pH 5.4 as a blank and free siRNA or Lipofectamine 2000 with the same amount of siRNA, prepared according to the instruction manuals. Samples were prepared as described under 3.3 and were nebulised with the nebuliser, which had resulted in the lowest impact on physicochemical properties of the respective formulation. Following transfection, cells were incubated for another 48 h. Afterwards, cells were detached using 0.05 % (v/v) trypsin and washed twice with PBS (400 rcf, 5 min, 21°C) before resuspending them in 400 µL of PBS with 2 mM EDTA. Samples were analysed by flow cytometry (Attune® NxT, Thermo Fischer Scientific, Waltham, Massachusetts, USA), and the average median fluorescence intensity (MFI) was measured with a 488 nm excitation laser and emitted light was detected through the BL-1H filter set. Experiments were performed in three biological replicates (N=3), each measured in technical triplicates (n=3). Sample results are displayed as % eGFP Expression through dividing average MFI of siRNA-treated samples by blank samples with corresponding standard deviation (SD).

#### **Application in fibrotic Precision-Cut Lung Slices (PCLS)**

#### Human donors and ethics statement

Investigations using human fibrotic tissue were approved by the ethics committee of the Hannover Medical School (MHH, Hannover, Germany) and are in compliance with "The Code of Ethics of the World Medical Association" (renewed on 2015/04/22, number 2701–2015). Informed consent was obtained from all patients prior to inclusion in the study. PCLS were prepared from explanted peripheral lung tissue obtained from 45 and 53-year-old male patients with progressive pulmonary fibrosis having a usual interstitial pneumonia (UIP)-pattern. Non-fibrotic tissue from non-CLD patient was obtained from the CPC-M bioArchive at the Comprehensive Pneumology Center (CPC Munich, Germany). The study was approved by the local ethics committee of the Ludwig-Maximilians University of Munich, Germany (Ethic vote 19-630). Written informed consent was obtained for study participant.

### **Preparation of PCLS**

After cannulating the human lung lobes with a flexible catheter, the explanted lung segments were inflated with warm (37 °C) low-melting agarose (1.5%) prepared in Dulbecco's Modified Eagle's Medium Nutrient Mixture F-12 Ham (DMEM-F-12), supplemented with 15 mM HEPES, 100 U/mL penicillin, and 100 μg/mL streptomycin (Invitrogen Life Technologies, Carlsbad, CA). Following sol-gel transition of the agarose solution on ice, tissue cores of a diameter of 8 mm were sectioned into 250–300 μm thin slices using a sharp, rotating metal tube. Sectioning procedure was conducted using a Krumdieck Live Tissue Microtome (Alabama Research and Development, AL). PCLS were washed three times for 30 min in DMEM-F-12 supplemented with 15 mM HEPES, 100 U/mL penicillin, and 100 μg/mL streptomycin (growth medium), and then left for 2 days in culture to acclimate and settle prior to transfection experiments.

#### Transfection and MMP7 gene silencing in PCLS

PCLS were placed into a 12 well plate and cultured in 800  $\mu$ L growth medium for 24 h. mPolyplexes were prepared according to section 3.3 encapsulating either siMMP7, siNC or AlexaFluor647-labeled siRNA at an N/P ratio of 10. Afterwards, the mPolyplexes were nebulised applying the best-suited nebulizer, and aerosol was collected in a 15 mL falcon tube. Subsequently, PCLS were transfected with 100 pmol siRNA in 200  $\mu$ L formulation buffer. PCLS were cultured for another 72 h and then collected for imaging, RNA or protein isolation, respectively.

#### **Two-Photon Laser Scanning Microscopy of PCLS**

Two-photon microscopy of transfected PCLS was performed with an inverted Leica SP8 DIVE system, equipped with a SpectraPhysics Insight X3 multiphoton laser and external spectral detectors. For the acquisition of the 2-photon z-stacks, we used a 10x0.4NA air objective, while the samples were mounted on a 35 mm glass-bottom dish with a glass thickness of 0.17mm. The xyz image data had a voxel of 0.76 x 0.76 x 5 µm. The Second Harmonic Generation (SHG), which is produced by collagen fibers, was acquired using an excitation at 860 nm. The back-scattered SHG was recorded with a Hybrid External Spectral Detector (HyD) set at 425-430 nm detection range. Simultaneously, we recorded with a second HyD the autofluorescence signal (produced by the same excitation at 860 nm), at a range of 450-510 nm. The AlexaFluor647 dye was excited at a frame-by-frame sequential manner by the 2-photon laser tuned at 1250 nm and the emission was captured with an external spectral PMT (Photomultiplier Tube) at a range of 635-705 nm. The acquired image data were uploaded on an Omero instance and the presented image panel was generated using the Omero. Figure plugin 138.

#### RNA isolation and qPCR

Total RNA was isolated by means of TRIzol/chloroform method and quantified using a Nanodrop Spectrophotometer (Thermo Fisher Scientific, Darmstadt, Germany). Complementary DNA (cDNA) was synthesised using a High-Capacity cDNA Reverse Transcription Kit (Thermo Fisher Scientific) according to the manufacturer's protocol. Quantitative real-time PCR (qRT-PCR) was performed using an iTaq Universal SYBR Green Supermix (BioRad, Feldkirchen, Germany) on a StepOnePlus System (Thermo Fisher Scientific). Hypoxanthine Guanine Phosphoribosyltransferase (HPRT) was used as the reference gene. For normalisation of MMP7 levels, the ΔΔCt method was applied. The primer sequences used are depicted in Table 1.

**Table 1.** Primers for PCR reaction. A = Adenine; C = Cytosine; G = Guanine; T = Thymine; MMP-7 = Matrix metalloprotease-7; HPRT = Hypoxanthine Guanine Phosphoribosyltransferase; Fw = forward; Rev = reverse.

Name	Primer sequences (5'-3')	
	Fw: AGTGAGCTACAGTGGGAACAG	Rev:
MMP7	TTTTGCATCTCCTTGAGTTTGGC	

Fw: AAGGACCCCACGAAGTGTTG Rev:

**HPRT** GGCTTTGTATTTTGCTTTTCCA

Fw: CTCCCCAGCCACAAAGAGTC Rev:

Collagen I CCGTTCTGTACGCAGGTGAT

Fw: CACCTCTGTGCAGACCACAT Rev:

**Fibronectin** ACCACACCACTGTCTGTGAC

#### Western-Blot

PCLS were homogenised in lysis buffer containing 50 mM Tris (pH 7.4), 150 mM NaCl, 1 mM EDTA, 1% triton X-100, 1% sodium deoxycholate, and 0.1% SDS, supplemented with 1 mM Na<sub>3</sub>VO<sub>4</sub>, 1 mM PMSF protease inhibitor, and 1 µg/mL cOmplete® protease inhibitor cocktail (Roche Applied Science, Indianapolis, IN). The detergent-insoluble material was precipitated by centrifugation at 18,600 g for 30 min at 4 °C. Protein concentration was measured using a Pierce<sup>TM</sup> BCA Protein Assay Kit (Thermo Fisher Scientific). Twenty µg of protein were separated on a 12% SDS polyacrylamide gel and subsequently transferred to a PVDF membrane (Roth, Karlsruhe, Germany). The membrane was blocked with 5% non-fat milk for 1h at room temperature and then incubated with a mouse anti-MMP7 (1:500, cat. no.: #MAB9071, R&D Systems, Wiesbaden, Germany) or goat anti-collagen 1 (1:500, cat. no.: 1310-01, Southernbiotech Birmingham, AL) antibody overnight at 4°C. β-actin, used as a loading control, was detected using a mouse anti-β-actin antibody (1:5000, cat. no.: A1978, Sigma-Aldrich, Taufkirchen, Germany). Proteins were detected using either Amersham ECL Select Western Blotting Detection Reagent (GE Healthcare, Chicago, IL) or Pierce ECL Western Blotting Substrate (Thermo Fisher Scientific). All images were acquired using a ChemiDoc Imaging Systems (Bio-Rad, Hercules, CA).

#### Statistical analysis

All experiments were performed in triplicates. Statistical analysis was performed using the GraphPad Prism 9.5.1 software and One-way ANOVA analysis or unpaired t-test.

## 4. Results and Discussion

#### **Particle formation**

Using the endogenous polyamine spermine, we established polymers with significantly improved encapsulation efficiencies, reaching 100% encapsulation at polymer to siRNA weight ratios of less than 10. It was previously shown that introducing hydrophobicity into polymeric siRNA delivery vehicles can have many advantages, such as increasing transfection efficiency through enhanced endosomal escape<sup>75</sup> and reducing toxicity through shielding of cationic charges 139,140. Therefore, we introduced varying hydrophobicity into the PBAE polymers studied here in a new and precise matter applying a controlled synthesis approach previously reported by our lab (Figure 1A)<sup>141</sup>. This enabled a precise tuning of polymer characteristics improving the conclusiveness of resulting data. By analysing the resulting structures with various methods, including cryo-TEM and MD simulations, a new structure type of nanoparticles was observed and named micelle-embedded polyplexes. This name was chosen because of the results obtained by previous MD simulations showing a deviation from typical micelleplex or polyplex structures reported by our group<sup>137</sup>. Micelleplexes are known to have a hydrophobic core and a hydrophilic shell, in which the siRNA is encapsulated. Polyplexes such as PEI typically have a uniform inner structure composed of encapsulated siRNA and polymer. Our results indicate the formation of small micelles composed of the PBAE carrier attaching to the siRNA with their hydrophilic outer shell. Thereby larger structures form with an siRNA core, a hydrophobic micelle-shell and a hydrophilic outer surface, composed of spermine sidechains. Several of these structures coalesce into bigger particles with an additional hydrophilic outer shell (Figures 1B & C). Due to this unique structure, we named these particles micelle-embedded Polyplexes (mPolyplex).

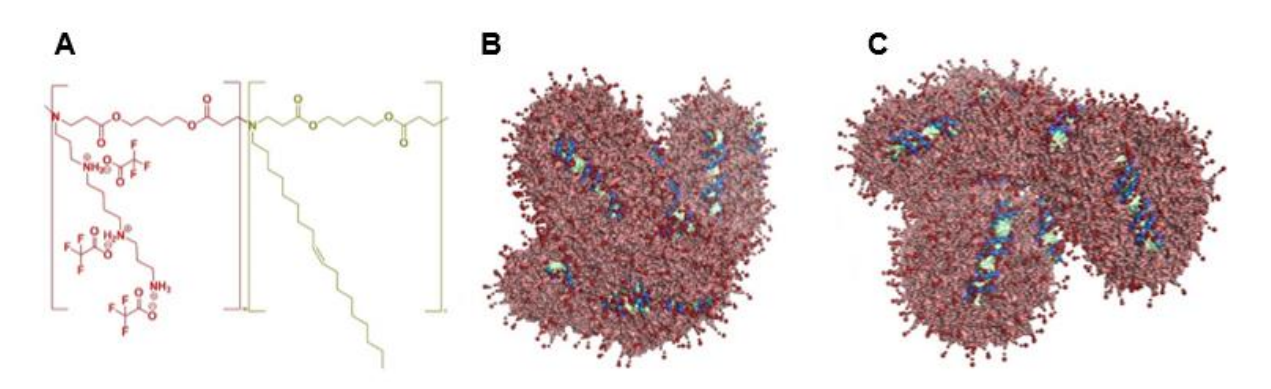


**Figure 1.** A) Chemical structure of the PBAEs described here with ionic spermine (red) and hydrophobic oleylamine (brown) side chains, B) and C) show two projections of MD simulations of mPolyplexes made of the 75% OA polymer at N/P 10 and pH of 5.4 in 10 mM HEPES buffer. Green and blue structures depict siRNA

strands, light red structures represent the hydrophobic parts of the polymer and dark red spots denote the hydrophilic spermine subunits.

#### Particle characterisation

The aim of this study was therapeutic pulmonary delivery of siRNA to target idiopathic pulmonary fibrosis. Therefore, a suitable delivery route to reach the cytosol of alveolar cells was necessary. As already discussed above, VMN have been reported to be the gentlest aerosolisation devices for liquid formulations. Here, the two clinically applied VMNs, the PARI eFlow® Rapid and the Aerogen Pro were applied to nebulise different mPolyplex suspensions. The difference between non-nebulised and nebulised particles was investigated for each mPolyplex formulation nebulised with each VMN. For additional comparison, PEI polyplexes were nebulised and investigated as well (Figure 2A).

All polymers tested formed monodisperse particles with small size ranging from 90 to 110 nm and a PDI of 0.1 to 0.2 (Figure 2B). The 30% OA mPolyplexes formed the smallest and the 75% OA mPolyplexes formed the largest particles. This size increase may be due to decreased charge density in the 75% OA mPolyplexes, leading to less compact particles. As the OA ratio increases, particle hydrophobicity also rises, leading to a greater proportion of weaker hydrophobic interactions as particle stabilizing forces. Consequently, overall intraparticular forces decrease, potentially causing larger particles, as similarly observed with NTA (Figure 2C). All particles exhibited positive ζ-potentials between 15 and 25 mV (Figure 2D), crucial for cellular uptake as the positive charge aids in attraction to the negatively charged the cellular membrane<sup>142</sup>, which is rich in glycan chains. Although not statistically significant, the ζpotential decreased with increasing OA ratios, likely due to shielding effects of the hydrophobic polymer content. Finally, the siRNA encapsulation and release from the particles was evaluated, and all polymers encapsulated 100% of the provided siRNA at N/P 10, with no detectable free siRNA even after nebulisation. Interestingly, only a combination of Triton-X, a surfactant, which disrupts hydrophobic interactions, and heparin, a polyanion that displaces siRNA from polyplexes through competition, successfully released 100% of the encapsulated siRNA from the mPolyplexes (Figure 2E and 2F). Neither heparin and Triton-X alone achieved full siRNA release (data not shown, but available in this reference 136). This observation suggests that mPolyplexes are stabilised by hydrophobic and electrostatic intraparticular forces which underlines the unique structure of this new particle class.

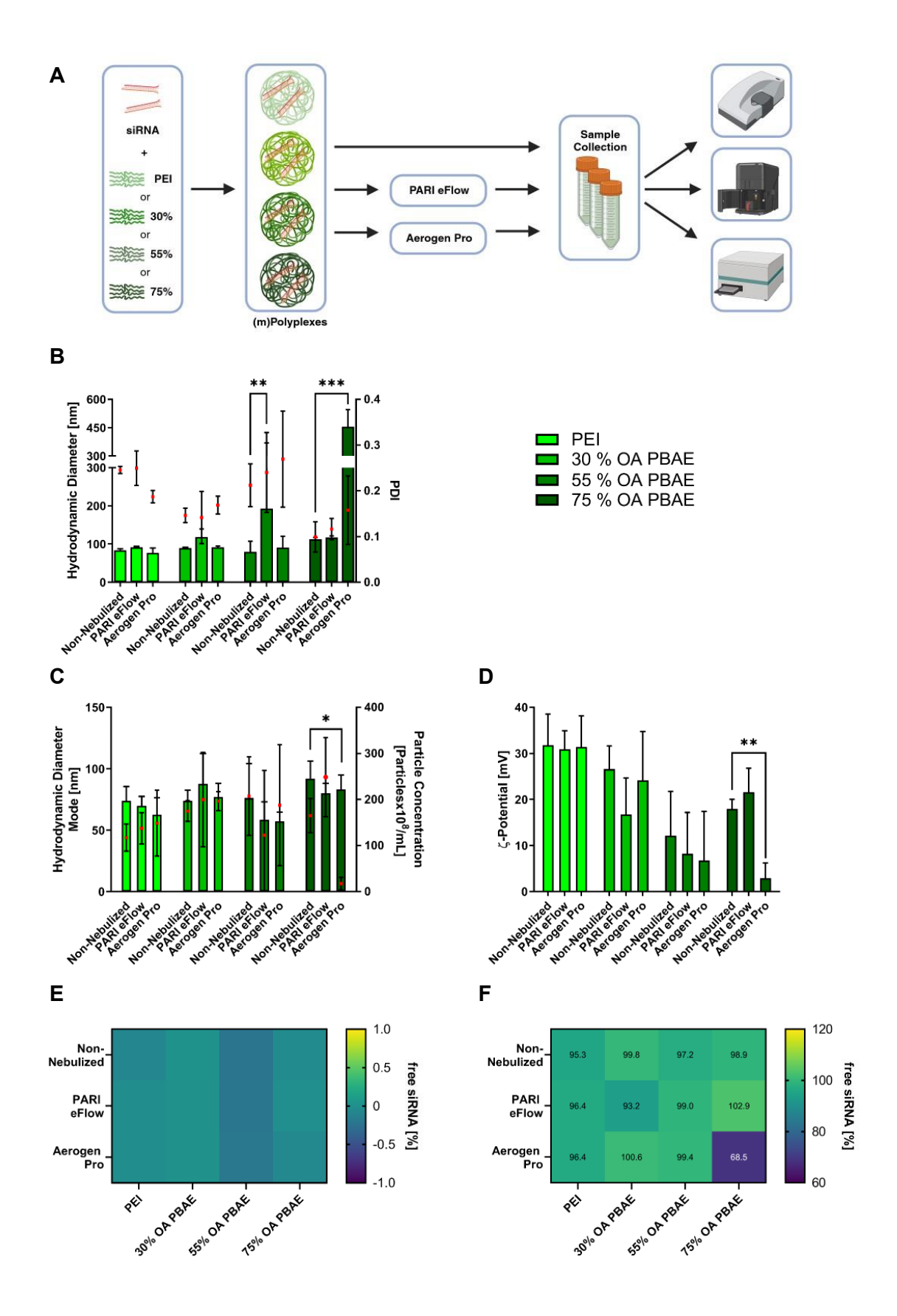


**Figure 2.** Physicochemical characteristics of PEI polyplexes and mPolyplex formulations before and after nebulisation with two different nebulisers. (A) is a scheme describing the experimental workflow, (B) shows the hydrodynamic diameter, determined via DLS with a 173° backscatter angle in a bar graph and the polydispersity

index (PDI) as red dots in the same graph, with the colour legend present on the right side. Colour legend also serves for Figure 2C and Figure 2D. Statistical analysis refers to hydrodynamic diameter data. (C) indicates the Mode of the particle sizes [nm] and the particle concentration in  $10^8$  particles/mL determined by Nanoparticle Tracking Analysis. Statistical analysis refers to particle concentration data. (D) shows the  $\zeta$ -Potential determined by Phase Analysis Light Scanning. (E) depicts the [%] encapsulated siRNA, either in a non-nebulized state or nebulized via the two respective VMNs, (F) shows the [%] of released siRNA, either in a non-nebulized state or nebulized via the two respective VMNs. Error bars denote mean  $\pm$  SD (N=3), One-Way ANOVA, \*, p < 0.05, \*\*, p < 0.01, \*\*\*, p < 0.001, no indication reflects non-significant differences.

PEI and 30% OA mPolyplexes showed no statistically significant changes in their physicochemical properties after nebulisation with either VMN. Parameters such as hydrodynamic diameter (Figure 2B), PDI (Figure 2B), particle concentration (Figure 2C) and ζ-potential (Figure 2D) remained stable, indicating that the stronger ionic intraparticular forces are resistant to nebulisation-associated stress. Changes were only observed for particles with higher hydrophobicity content. Physicochemical characteristics of 55% OA mPolyplex were affected by nebulisation with the PARI eFlow® Rapid. The hydrodynamic diameter increased (Figure 2B), while particle concentration, determined by NTA, decreased (Figure 2C). This concentration drop likely results from aggregate formation during nebulisation, explaining the increased particle size. A similar, though not statistically significant, trend was observed for the 30% OA mPolyplexes (Figure 2C), suggesting that higher hydrophobic contents within the particles increases the susceptibility to VMN-induced shear stress. Interestingly, this susceptibility was even more pronounced in the 75% OA mPolyplex, but only when nebulised with the Aerogen Pro VMN. Here, the hydrodynamic diameter increased significantly (Figure 2B), and the ζ-potential became significantly more neutral (Figure 2D), which could promote aggregation due to reduced particle repulsion. This explains the increased particle size and the significantly lower particle concentration (Figure 2C). Additionally, these particles were the only formulation, in which only a fraction of the encapsulated siRNA could be recovered (Figure 2F). It remains unclear if the siRNA was indeed degraded or if the formed aggregates resisted complete dissociation by the Triton-X and heparin mixture.

It seems plausible that the higher OA content, with its weaker intracellular forces, the 55% OA mPolyplexes, was insufficient to withstand the higher energy input of the PARI eFlow® Rapid (Table 2). However, it is surprising that this trend was not observed in the 75% OA mPolyplexes, which appeared more resistant to the high energy input but were more sensitive

to the faster nebulisation speed. This suggests that the shear stress in the Aerogen Pro may be higher, causing destabilisation of the 75% OA mPolyplexes.

Table 2. Differences in performance indicating parameters for the PARI eFlow® Rapid and Aerogen Pro VMNs

Nebuliser	Energy Input [J/g] <sup>143</sup>	Nebulisation Speed [mL/min]	Residual Volume [mL]
PARI eFlow® Rapid	35 ± 12	0.54	~ 1
Aerogen Pro	$18 \pm 6$	0.29	n. a.

These results confirm that a suitable VMN device was identified for all mPolyplex formulations, without impacting their physicochemical characteristics. Cryo-TEM images of the 30% and 55% OA mPolyplexes taken before and after nebulisation (Supplementary Figure S1) further support this observation. It was concluded that particles stabilised by hydrophobic interactions are more susceptible to nebuliser-induced aggregation and degradation, a trend also observed with lipid nanoparticles. However, it is surprising that mPolyplexes with very high OA ratios responded differently to the two tested nebulisers.

#### Aerosol characterisation by laser diffraction

**Table 3.** Laser diffraction results of different nebulised nanoparticle formulations. (Data points indicate mean  $\pm$  SD, N = 3)

Cample	$X (Q3 = 50\%) [\mu m]$	X (Q3 = 50%) [μm]  PARI eFlow® Rapid		
Sample	Aerogen Pro			
10 mM HEPES	$5.43 \pm 0.09$	$4.49 \pm 0.13$		
PEI	$4.54 \pm 0.07$	$4.77\pm0.06$		
30% OA PBAE	$4.19 \pm 0.01$	$4.12\pm0.16$		
55% OA PBAE	$4.31\pm0.04$	$4.19\pm0.09$		
75% OA PBAE	$4.18 \pm 0.02$	$4.25\pm0.11$		

Aerosol characterisation was carried out using Laser Diffraction, with results presented as Q3-VMD in Table 3. The results allow direct comparison of each nanoparticle formulation, varying in hydrophobic content, across the different VMNs in comparison to the formulation buffer only. PEI served as the control for siRNA polyplexes without any surface-active properties. As shown in Table 3 and Supplementary Figure S2, all nebulised nanoparticle formulations fell within the  $1-5 \mu m$  droplet range, a well-known size range for effective sedimentation and deposition within the alveoli, making all tested nebulisers suitable for pulmonary delivery of the chosen formulations<sup>144</sup>. An interesting trend emerged for the Aerogen Pro: the formulation buffer only showed the highest median diameter at  $5.43 \pm 0.09$  µm. When PEI polyplexes were added, the median diameter decreased to  $4.54 \pm 0.07$  µm. However, including surface-active polymers forming mPolyplexes, further reduced the median diameter, with the 75% OA PBAE (the most lipophilic compound) reaching a minimum of  $4.18 \pm 0.02 \,\mu m$  with the Aerogen Pro. A similar trend was observed with the PARI eFlow, though less pronounced: the formulation buffer had a median diameter of  $4.49 \pm 0.13 \,\mu m$  appeared, which increased slightly to 4.77 $\pm 0.06$  µm with PEI polyplexes. However, adding amphiphilic nanoparticles reduced the median diameter below that of the formulation buffer, reaching a low of  $4.12 \pm 0.16$  µm for the 30% OA PBAE polyplex formulation.

Literature provides some theories about these findings: first, adding nanoparticles to the buffer may decrease the median droplet diameter due to higher charge density from negatively charged siRNA and positively charged carriers such as PEI and PBAEs. Increased charge-density is known to reduce the mass median aerodynamic diameter (MMAD), as shown in studies adding different salts to nebuliser solutions <sup>145,146</sup>. Zhang et al. observed that increased conductivity lowers droplet VMD and fine particle fraction (FPF) of aerosols and increases reproducibility between the measurements <sup>146</sup>.

The experimental setup chosen here also answers the less clear influence of surface-active molecules on aerosol characteristics. Studies with surfactants, such as SDS (sodium dodecyl sulfate) and Tween 20, in formulations used in vibrating mesh nebulisers resulted in a decrease in VMD. Beck-Broichsitter et al. attributed this effect primarily to the increased conductivity rather than changes in surface tension alone, as both parameters were monitored during their study<sup>125</sup>.

A 2012 study found that increasing polyvinyl alcohol (PVA) concentrations reduced MMAD<sup>125</sup>, suggesting that surface-active molecules significantly affect droplet size. According to Tate's law, surface tension influences droplet volume as Zhang et al. noted<sup>146</sup>. Another factor is the wetting of the hydrophilic nebuliser's palladium-nickel membrane. While increased surface tension reduces output due to decreased spreading on the nebuliser membrane, Zhang et al. also found that surfactants such as pluronic at equilibrium concentrations cannot consistently lower surface tension at the continuously forming new droplet interfaces. The comparably minor influence of surface tension was explained by the surfactants' slow adsorption rate to the newly created air—water interfaces, leading to surface tension gradients at the site where aerosol droplets form<sup>146</sup>.

It was also shown that increased viscosity reduces MMADs and output ranges  $^{145}$ , but this parameter is expected to have little-to-no influence here. Instead, relative humidity significantly impacts aerosol performance, with higher % RH (as present in the physiological lung) leading to smaller median diameters, fitting better into the target  $1-5~\mu m$  range. This is due to the faster evaporation from smaller particles at low % RH leading to a shift to wrongfully higher median diameters. Therefore, our experimental set-up (Supplementary Figure S3) was all enclosed in a plastic box with a humidifier (Beurer GmbH, Ulm, Germany), maintaining values above 70% RH.

#### In vitro protein knockdown in H1299-eGFP cells

Although the above experiments sowed that the physicochemical properties of the nanoparticle systems remained stable during nebulisation with at least one of the tested VMNs, it is equally important to preserve the biological stability and activity of the siRNA during this process. To assess biological activity post-nebulisation, the stably eGFP expressing cell line H1299-eGFP served as an *in vitro* model for siRNA gene silencing efficacy. This epithelial-like lung cell line is an ideal model as it mimics the likely port of entry for nebulised formulations.

Based on the above experiments the best-performing nebulisers were selected for each formulation: the Aerogen Pro for 30% OA PBAE and 55% OA PBAE mPolyplexes was chosen and the PARI eFlow® Rapid for 75% OA PBAE mPolyplexes. As shown in Figure 3A-C, particles encapsulating negative control siRNA had no gene silencing efficacy at all. On the contrary, these particles seemed to induce eGFP, possibly through nanoparticle-stimulated overall induction of protein biosynthesis. Most importantly, however, siGFP-loaded nanoparticles mediated sequence-dependent RNAi: the 30% OA non-nebulized mPolyplexes reduced eGFP expression by about 23% (Figure 3A), while the nebulised achieved a 73% reduction, tripling gene silencing efficacy despite no observable differences in physicochemical properties. Nebulisation was hypothesised to induce internal structural changes that may loosen siRNA/polymer interactions. A previously reported stability assay confirmed this assumption (Figure S4), revealing a decrease in EC50 from 9.4 to 8.4, indicating slightly weakened intraparticular forces. It was previously hypothesized that highly stable particles can be detrimental to successful cytosolic siRNA delivery due to a hampered release of siRNA<sup>33</sup>. It is important to point out that the reduced intraparticular binding strength had no observable impact on the colloidal stability. Additionally, no significant differences in transfection efficiency were observed between non-nebulised and the nebulised 55% OA PBAE (Figure 3B) and 75% OA PBAE formulations (Figure 3C). In case of the most cationic 30% OA PBAE polymer (Figure 3A), however, significantly improved gene silencing activity after nebulisation further supports our hypothesis of a reduction in intraparticular binding strength during nebulisation.

Comparing the three different OA contents of the PBAEs reveals a trend: higher hydrophobic OA content correlates with increased gene silencing efficacy. The 75% OA PBAE mPolyplexes showed the highest efficiency, silencing eGFP by 91% in the non-nebulised form and 80% postnebulisation. The 55% OA PBAE achieved 78% before and 79% after nebulisation. Recent literature also underlines this trend<sup>75,141</sup>, suggesting that higher unsaturated fatty acid content enhances nanoparticle fusogenicity, thus enhancing endosomal escape. Furthermore, considering the changed behaviour of the 30% OA PBAE before and after nebulisation, it is

possible that increased hydrophobic contents could lead to a favourable less pronounced siRNA binding to the polymer, allowing more effective siRNA release. Overall, these results are promising for therapeutic applications, as the biological effect of mPolyplexes was maintained or even improved after nebulisation.

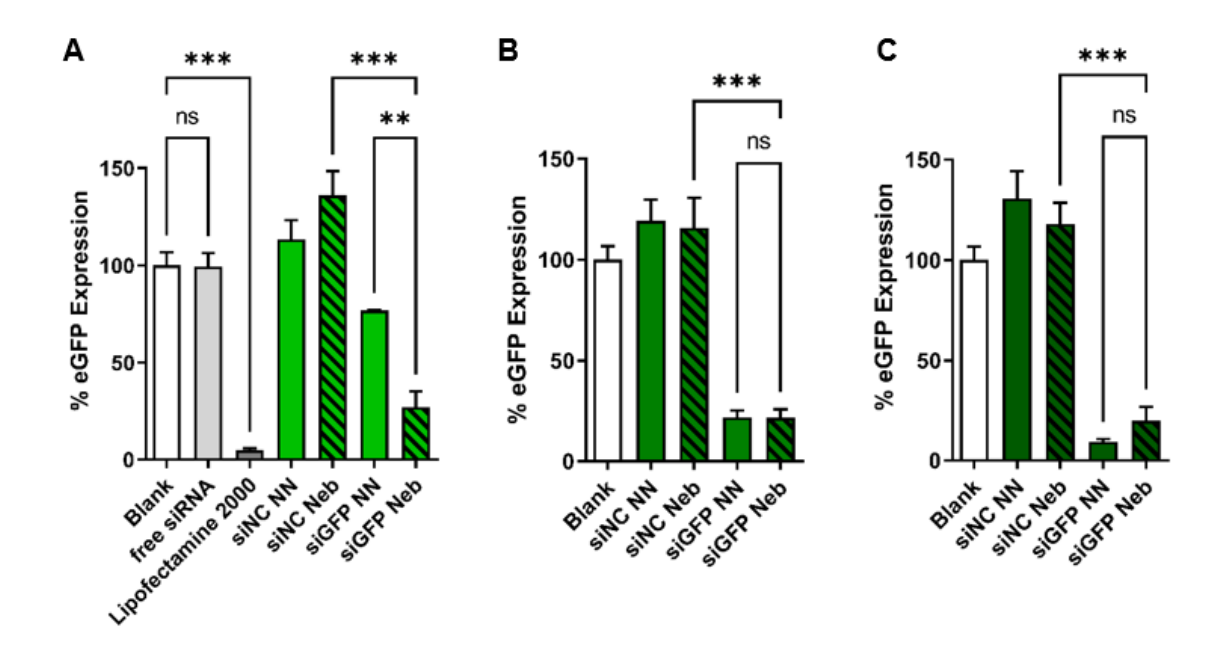


**Figure 3.** In-vitro eGFP knockdown in H1299-eGFP cells. Polymers with varying OA content encapsulating 50 pmol siRNA were tested either in non-nebulised (NN) or in nebulised (Neb) form and compared to blank cells (white bar), free siRNA (light grey) and Lipofectamine 2000 lipoplexes encapsulating the same siRNA as positive control (dark grey). mPolyplexes are divided into (A) 30% OA PBAE, (B) 55% OA PBAE and (C) 75% OA PBAE. Bars show % eGFP expression as calculated from MFI values  $\pm$  SD (N=3), One-Way ANOVA, \*\*, p < 0.01, \*\*\*, p < 0.001, ns = non-significant.

#### Nanoparticle transfection efficiency in fibrotic PCLS

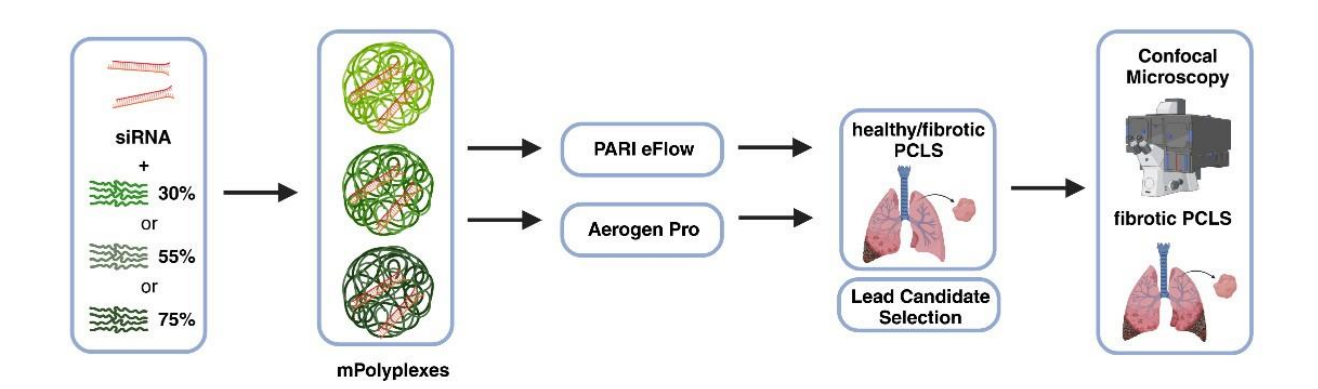


**Figure 4.** Workflow of NP's performance evaluation *ex vivo*. The siRNA was encapsulated by 30%, 55%, and 75% OA PBAE polymers at N/P 10 and nebulised via the Pari eFlow<sup>®</sup> Rapid or Aerogen Pro and evaluated in healthy and / or fibrotic PCLS.

Following the 3R principle we applied a model better suited for studying human IPF than classical murine models. We tested the efficacy of our approach in the complex model of human lung fibrosis using PCLS, which maintain the lung's native architecture, including cell and ECM composition, and thus mimics the disease's pathophysiological characteristics (Figure 4)<sup>147</sup>. Studying nanoparticle behaviour in this diseased state is crucial for better understanding potential treatment options and advancing from preclinical to clinical stages. Preliminary experiments in peritumour tissue, using GAPDH knockdown, showed no difference between the nebulised and non-nebulised 30% OA PBAE mPolyplexes (Supplementary Figure S5). In fact, mPolyplexes made of 30% OA PBAE showed no negative changes in physicochemical properties across all VMNs. While mPolyplexes made of 75% OA PBAE showed a slight decrease in gene silencing efficacy post-nebulisation, the 30% OA PBAE mPolyplexes performed better in PCLS (Supplementary Figure S5). Furthermore, initial pre-screening in fibrotic PCLS showed superior gene silencing capacity of the 30% OA PBAE in comparison to the more lipophilic ones (Supplementary Figure S6), making it the lead candidate for additional PCLS experiments.

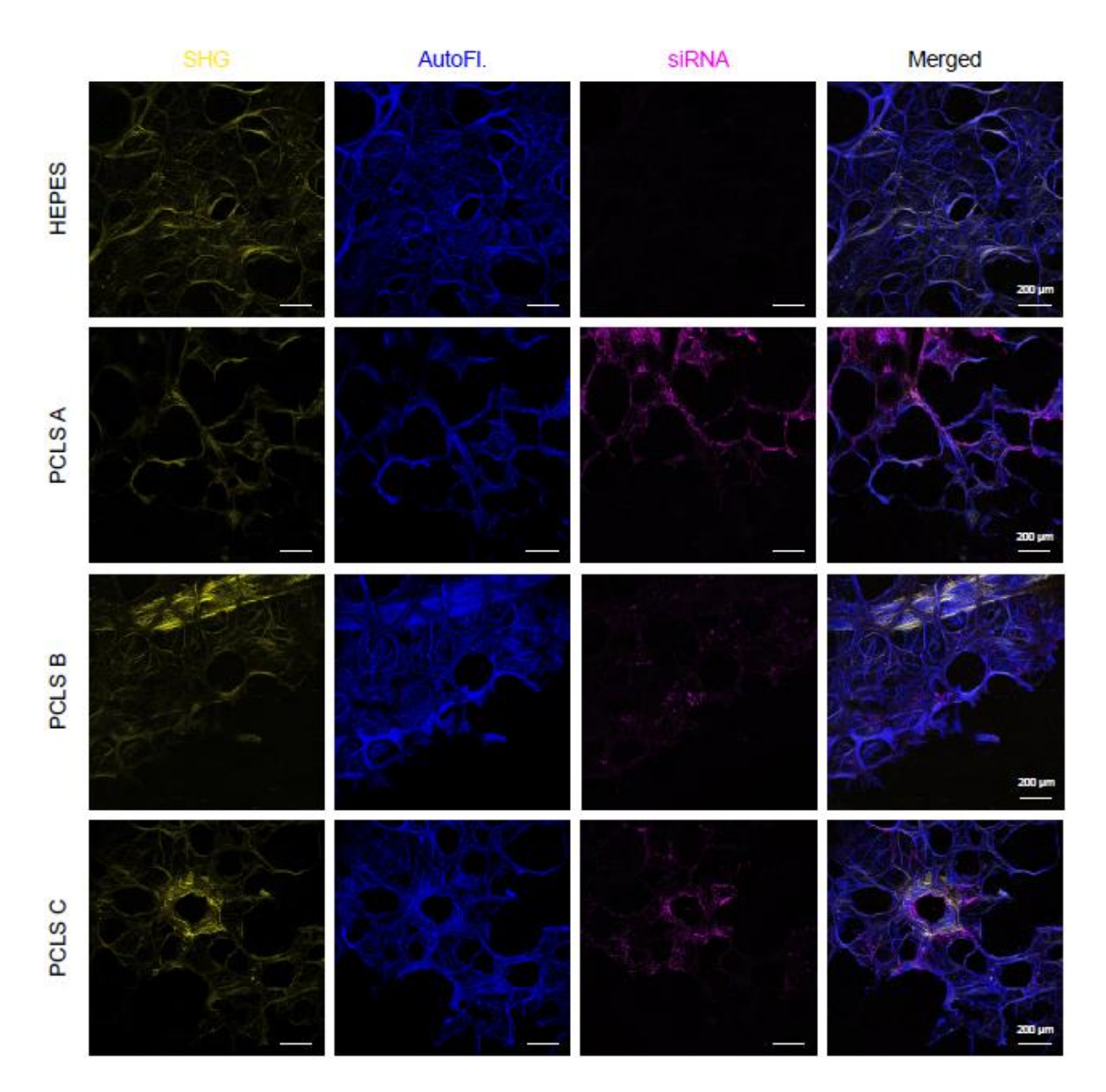


**Figure 5.** Maximum intensity projections of 2-Photon microscopy images of fibrotic PCLS; first column presents the Second Harmonic Generation (SHG in yellow) from collagen fibers, second column presents tissue autofluorescence in blue (450-510nm), the third column shows the signal of Alexa Fluor 647 (in magenta) while the last column is an overlay of all channels. First row indicated as HEPES was transfected with 10 mM HEPES, pH 5.4 as blank; PCLS A, B and C were transfected with 100 pmol AF-647 labelled siRNA, encapsulated by 30% OA PBAE at a N/P ratio of 10.

Transfection efficacy of this lead formulation was subsequently investigated in three PCLS samples from different regions of the fibrotic lung from one patient, using high-resolution live imaging. A transfection control with formulation buffer only was included. As shown in Figure 5, all PCLS samples displayed pronounced ECM, visualised by strong fluorescence in

the second harmonic generation (SHG) channel, which visualises fibrillar collagen I and II, confirming the fibrotic nature of the samples. In the control sample with HEPES, no fluorescence was detected in the siRNA channel, but strong fluorescence appeared in all nanoparticle-treated samples, indicating excellent transfection efficiency with varying signal intensity depending on lung tissue architecture and cell composition. Across all three *ex vivo* samples, the siAF647-labeled nanoparticles penetrated the fibrotic PCLS, confirming that excessive collagen in the model does not hinder nanoparticles mobility.

### MMP7 knockdown in a relevant idiopathic fibrotic PCLS model

Gene silencing efficacy of mPolyplexes was further investigated in a relevant idiopathic fibrotic PCLS model. MMP7, a profibrotic molecule that contributes to increased ECM production and, consequently, to elevated collagen I levels, is a promising RNAi target for treating IPF. Given the satisfactory siRNA delivery efficiency observed in confocal images, 30% OA mPolyplexes were selected to assess MMP7 knockdown potential. Lipofectamine 2000, while efficient for transfection, is too toxic for *in vivo* use and served as positive control only. According to qPCR results (Figure 6A), using the  $\Delta\Delta$ Ct method with the house-keeping gene HPRT, Lipofectamine 2000 achieved a relative knockdown of 21% of the target gene compared to siNC samples. Interestingly, the nebulised lead nanoparticle formulation showed a superior 52% knockdown, surpassing Lipofectamine 2000's transfection level without its associated high toxicity. For downstream effect, collagen I levels were determined via qPCR, showing similar trends (Figure 6B): while Lipofectamine 2000's treatment led to a non-significant gene silencing of 11%, the tested 30% OA PBAE achieved a downregulation of 33% for Col I, indicating that the MMP7 downstream cascade was partially inhibited ex vivo. Fibronectin levels, which is also considered to be part of IPF's pathology<sup>148</sup>, were downregulated on minor levels for Lipofectamine 2000 and 30% OA PBAE after siMMP7 treatment and are depicted in Supplementary Figure S5. Interestingly, the hydrophobic carrier appears to influence treatment effectiveness. Others have shown that hydrophobic polystyrene exhibits stronger adsorption to collagen I than its oxidised counterpart<sup>129</sup>. Therefore, it is hypothesized that 30% OA PBAE mPolyplexes balance effective collagen penetration with sufficient endosomal release for gene silencing. While increasing OA content improved knockdown efficiency in the H1299-eGFP model before nebulisation, this effect was less pronounced in peritumour PCLS tissue (Supplementary Figure S6 and S7). Consequently, it can be inferred that in tissues with significant collagen overexpression, the use of a more hydrophilic carrier system may be advantageous.

Western blot analysis was used to assess the effect of the siRNA formulations on protein levels, specifically targeting MMP7 (Figure S8), with  $\beta$ -actin serving as a control protein. 30% OA mPolyplexes reduced MMP7 protein levels compared to the control formulation, leading to a marked reduction in collagen I expression, a downstream effector of MMP7. Since collagen I is a key ECM component and often elevated in IPF patients, this reduction is highly relevant and suggests that this treatment may positively influence the progression of the disease, addressing the underlying cause of IPF rather than merely alleviating symptoms.

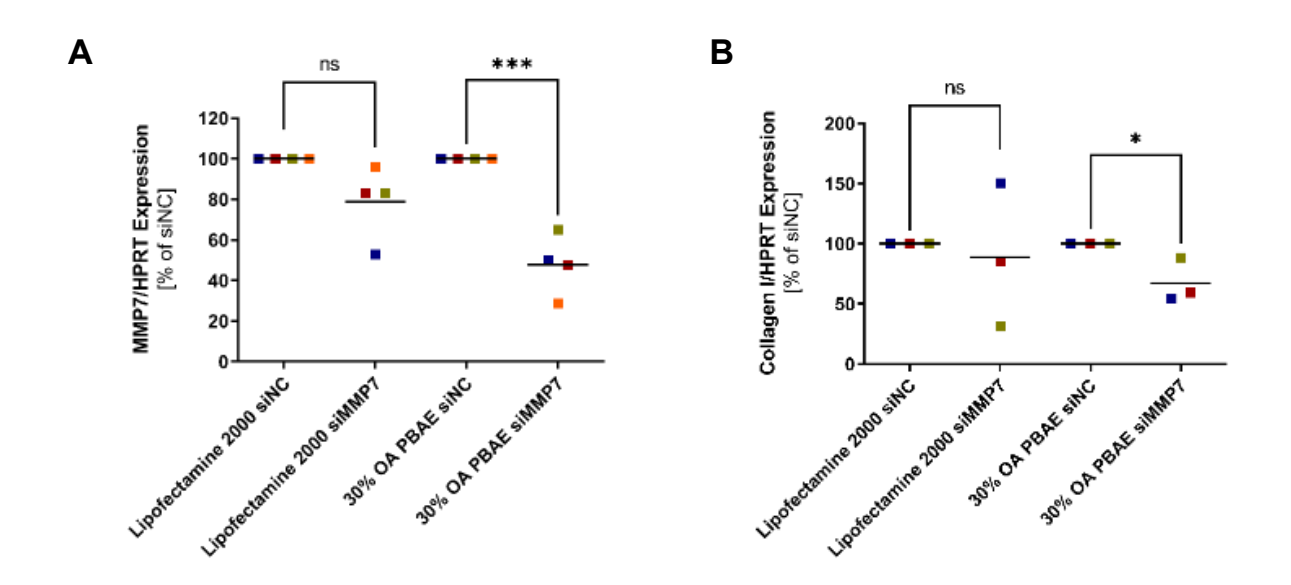


**Figure 6.** Ex vivo MMP7 knockdown in fibrotic PCLS. Fibrotic PCLS were transfected with 100 pmol of either siMMP7 or siNC, encapsulated by 30% OA PBAE N/P 10 after nebulisation or with the same amount siRNA lipoplexes, formed with Lipofectamine 2000 as positive control. RT-qPCR results from A) MMP7 and B) Collagen I in comparison to housekeeping gene HPRT. Unpaired t-test, \*, p < 0.05, \*\*\*, p < 0.001, ns = non-significant. Dots indicate results from each single fibrotic tissue while the line indicates the mean (N=4 for A) and N=3 for B)).

Therefore, the primary advantages of these newly developed PBAE-micelleplexes lie in their excellent nebulisability, which retains or even enhances their functionality, as well as their customisable properties. The ability to adjust lipophilic content to suit specific disease states is particularly advantageous, as is the overall flexibility in modifying structural entities and potentially incorporating targeting ligands.

### 5. Conclusion

This study demonstrated that PBAE-based nanoparticles can be nebulised using clinically relevant VMNs without altering their physicochemical characteristics. Increasing hydrophobicity reduced nanoparticle stability against nebulisation associated stress, but suitable nebulisation settings were found to maintain particle integrity and functionality as confirmed in vitro. The presence of mPolyplexes slightly decreased VMDs of buffer solutions with the used VMNs. The research aimed to assess a potential inhalable siRNA therapeutic approach for IPF. With a disease relevant ex vivo model, successful nanoparticle uptake and MMP7 gene knockdown were confirmed via western blot and qPCR in PCLS, resulting in downregulation of the disease-related protein collagen I. These findings highlight the potential of this new delivery system for targeting pulmonary diseases, even in challenging conditions such as IPF. Especially the tunability of hydrophobicity and nebuliser settings allow for rapid adaptation to different pathophysiological needs. Furthermore, IPF patients would benefit from nebulisation as route of administration compared to other pulmonary delivery methods such as pressurised metered dose inhalers or dry powder inhalers, due to their often limited lung capacity. Additionally, this approach could also be applied to other pulmonary diseases, including asthma or chronic obstructive pulmonary disease, by choosing a suitable molecular target. It is believed that this study will advance nebulisation-based pulmonary disease research and accelerate the development of clinically relevant formulations.

## 6. Acknowledgments

We thank Ronan MacLoughlin from Aerogen Ltd. for kindly providing us the used Aerogen Pro for experimental purposes. Olivia Merkel gratefully acknowledges Volkswagen Foundation (AZ-9A872) and the European Research Council (ERC-2022-COG-101088587). We gratefully acknowledge the provision of human biomaterial (non-fibrotic fresh tissue from non-CLD patient) and clinical data from the CPC-M bioArchive and its partners at the Asklepios Biobank Gauting, the LMU Hospital and the Ludwig-Maximilians-Universität München. We thank the patient and their family for their support. We thank Thomas Michler for providing scientific input and supervision. Figures were partially generated using biorender.com.

## 7. Supporting Information

**Table S1.** from Zimmermann et al, doi:  $\underline{10.1016/j.j.conrel.2022.09.021}$ . Sequences of siRNAs used in the study. Nt = nucleotides; GFP = green fluorescence protein; NC = negative control; GAPDH = housekeeping gene GAPDH; A = Adenine; C = Cytosine; G = Guanine; G =

Name	Sense strand (5'-3')	Antisense strand (3'-5')	Length (nt)	
			Sense	Antisense
siGFP	pACCCUGAAGUUCAUCUG	<u>ACU</u> GGGACUUCAAGUAGAC	25	27
	CACCACcg	GUGGUGGC		
siNC	pCGUUAAUCGCGUAUAAU	<u>CAG</u> C <u>A</u> A <u>U</u> U <u>A</u> G <u>C</u> G <u>C</u> A <u>U</u> A <u>U</u> U <u>A</u>	25	27
	ACGCGUat	UGCGCAUAp		
siGAPDH	pGGUCGGAGUCAACGGAU	<u>UUC</u> C <u>A</u> G <u>C</u> C <u>U</u> C <u>A</u> G <u>U</u> U <u>G</u> C <u>C</u> U <u>A</u>	25	27
	UUGGUCgt	AACCAGCA		

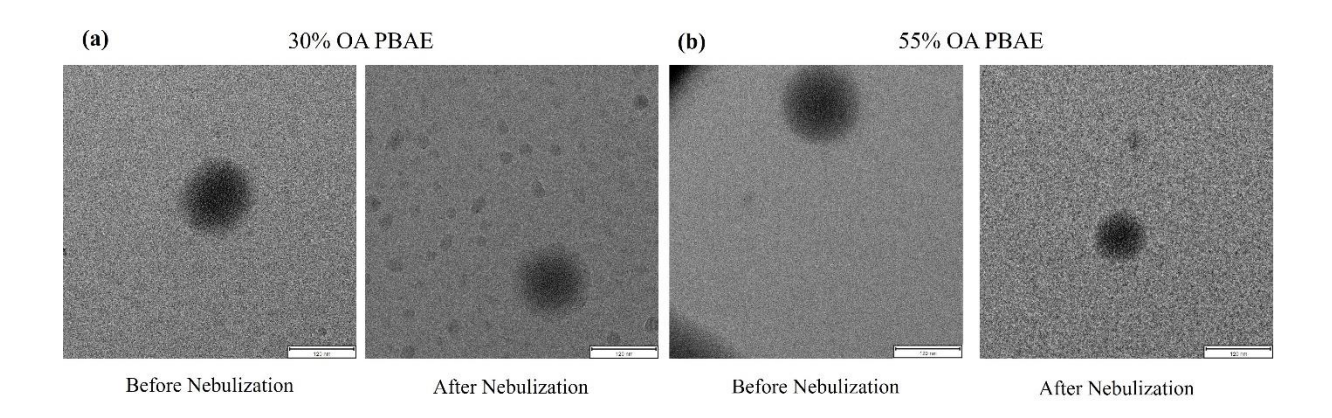


Figure S1. Cryo-TEM pictures of 30% OA (a) and 55% OA (b) PBAEs mPolyplexes before (left) and after nebulisation (right)

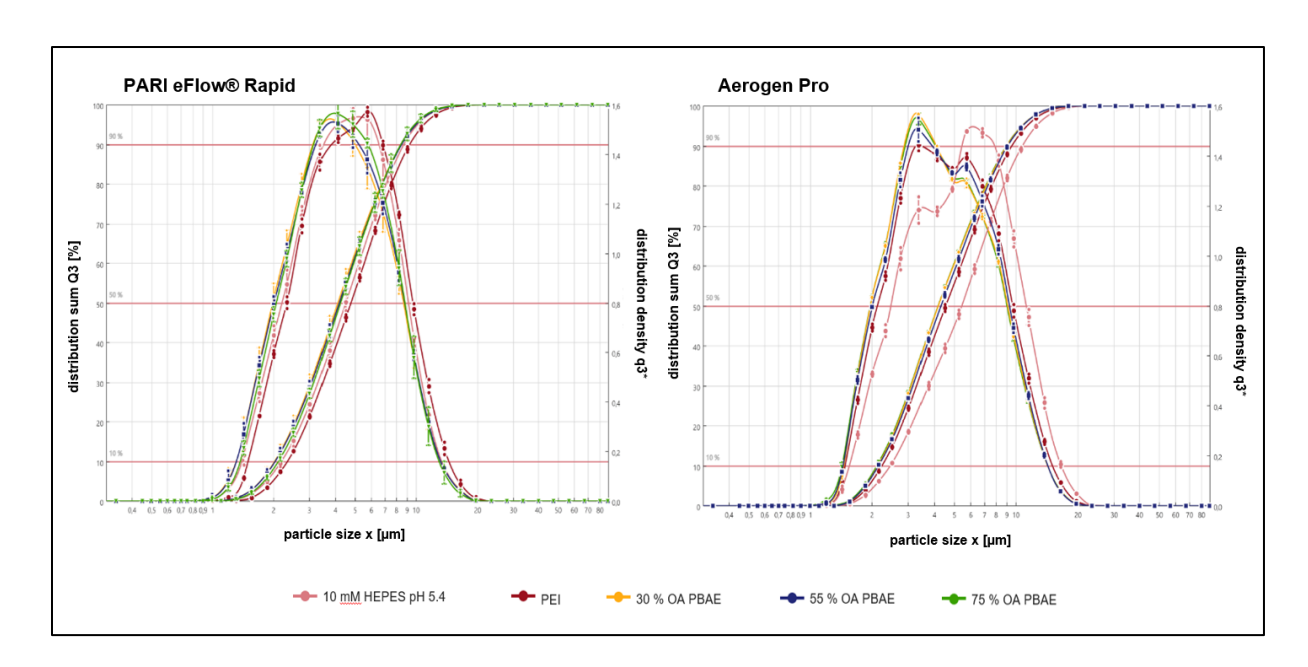


Figure S2. Laser diffraction results of nebulised formulations and control solutions.

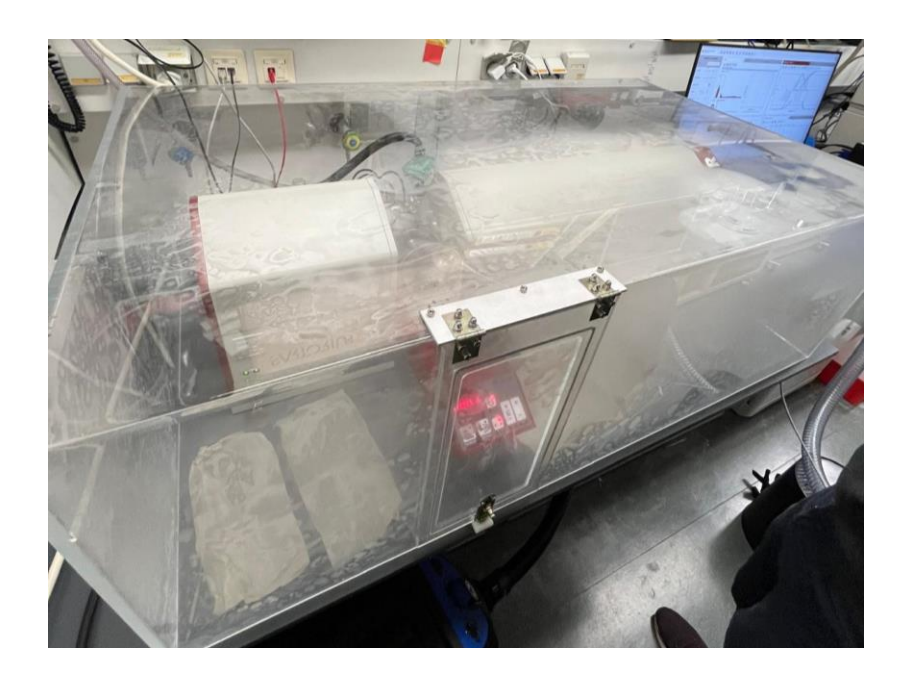
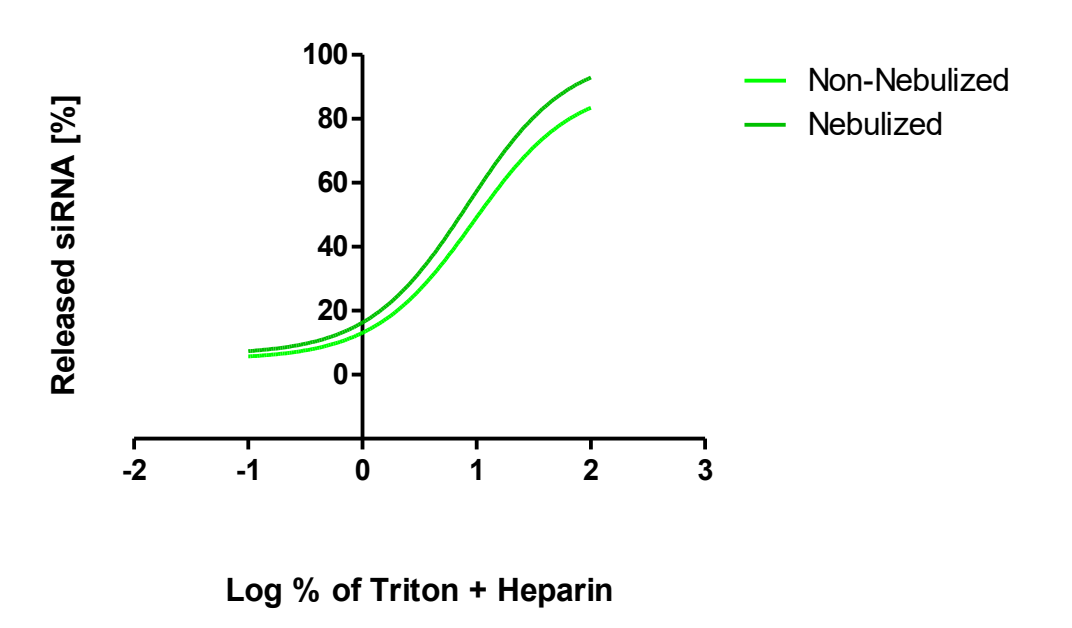


Figure S3. Experimental set-up with equipped humidity box.



**Figure S4.** Intraparticular stability of 30% OA NP's determined via siRNA release as a function of of Triton-X and heparin concentrations.

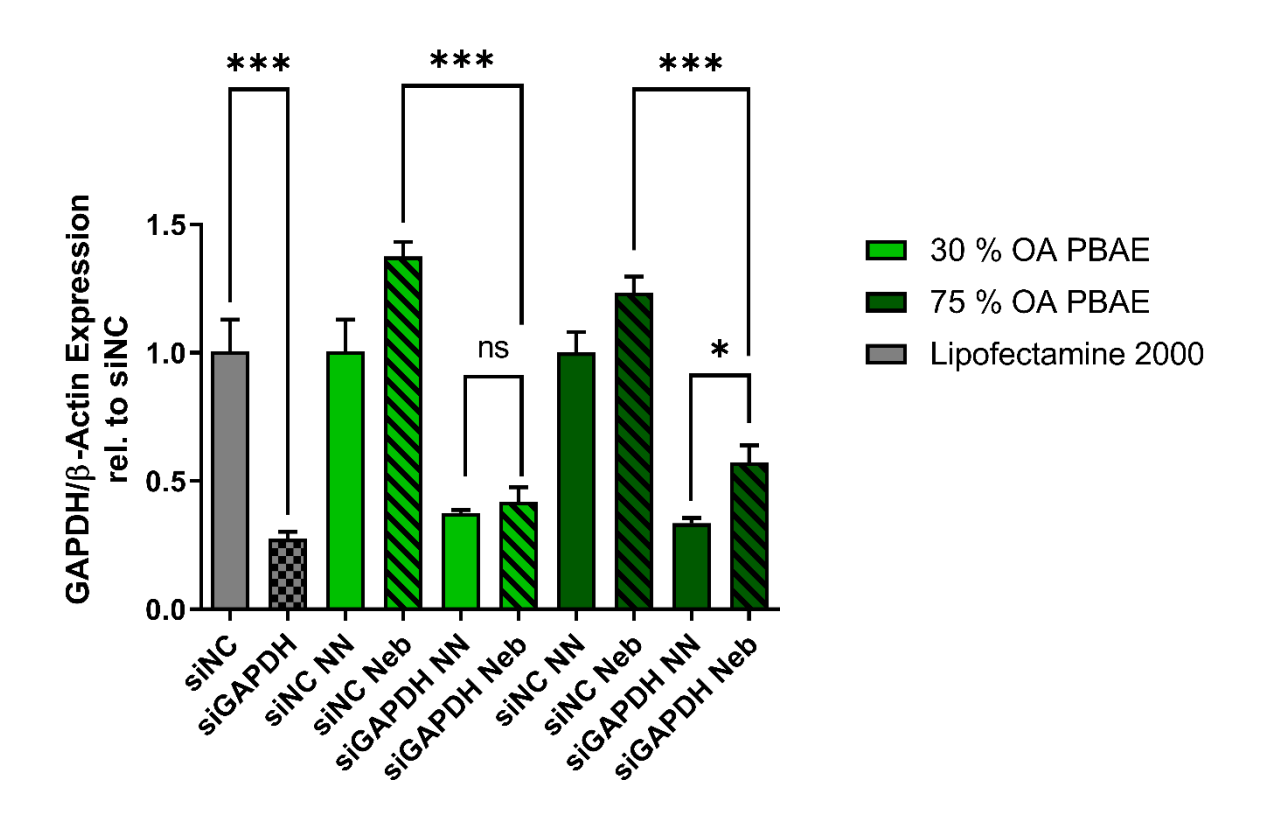
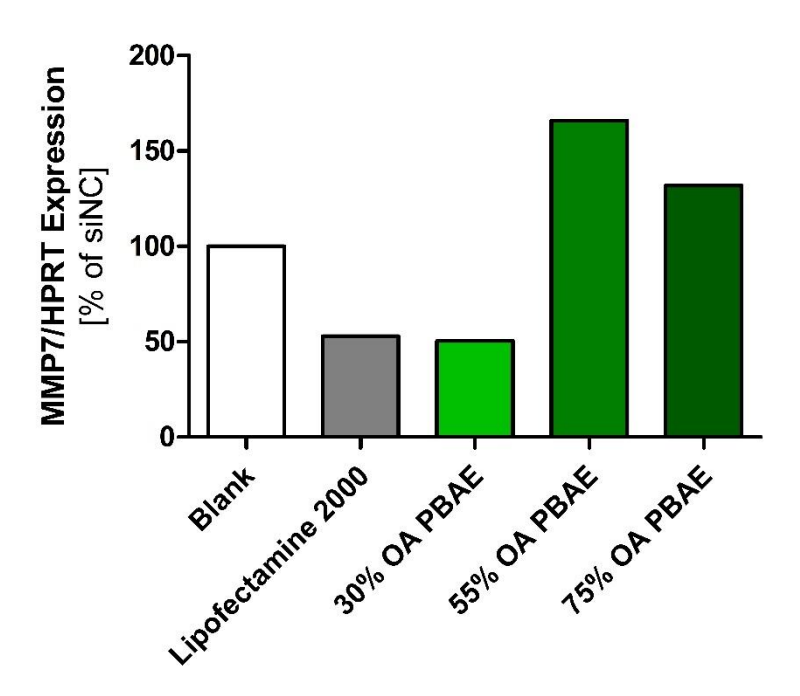


Figure S5. GAPDH knockdown in peritumour PCLS after transfection with mPolyplexes made of PBAEs with different OA content before and after nebulisation.



**Figure S6.** MMP7 Knock-Down Screening in fibrotic PCLS with mPolyplexes consisting of PBAEs with different OA content.

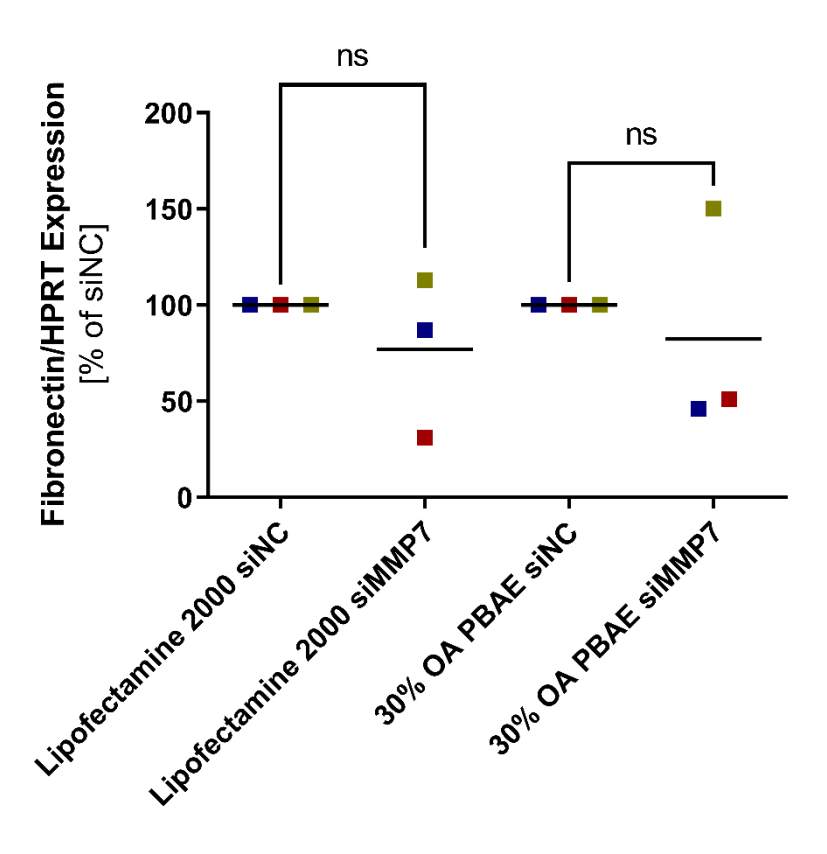


Figure S7. Fibronectin knockdown in fibrotic PCLS transfected with Lipofectamine 2000 and nebulised 30% OA PBAEs mPolyplexes.

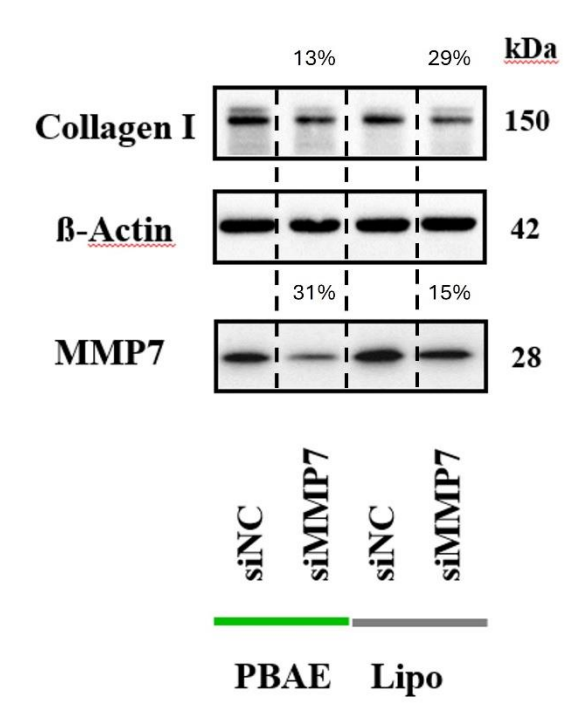


Figure S8. Collagen I and MMP-7 knockdown after transfection with Lipofectamine 2000 and nebulised 30% OA PBAEs. Percentages are shown against negative control sequence and all bands are corrected for  $\beta$ -actin bands intensity as housekeeping gene.

### **CMC** determination of the polymers:

PBAE stocks were diluted in 10 mM HEPES pH 5.4 to concentrations between 0.1 and  $200 \,\mu g/mL$ . Fluorescence emission spectra (Figure S9 and S10.) were recorded for each concentration using a plate reader (TECAN Spark, TECAN, Männedorf, Switzerland)) between 300 and 450 nm excitation and 500 nm emission wavelength.

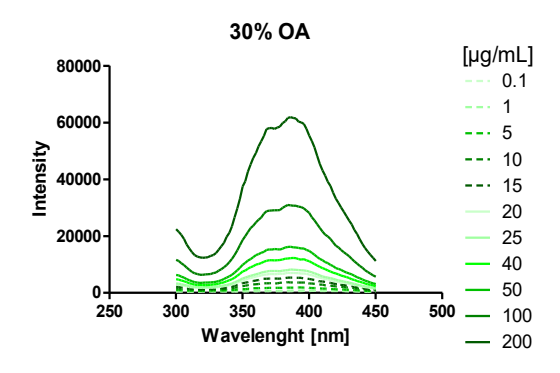


Figure S9. Exemplary fluorescence emission spectra recorded at 500 nm for different concentrations of 30% OA PBAE solutions in 10 mM HEPES pH 5.4

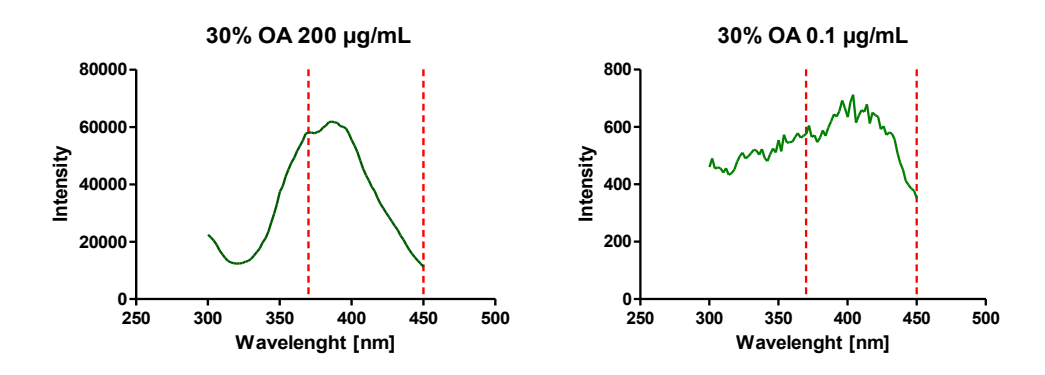
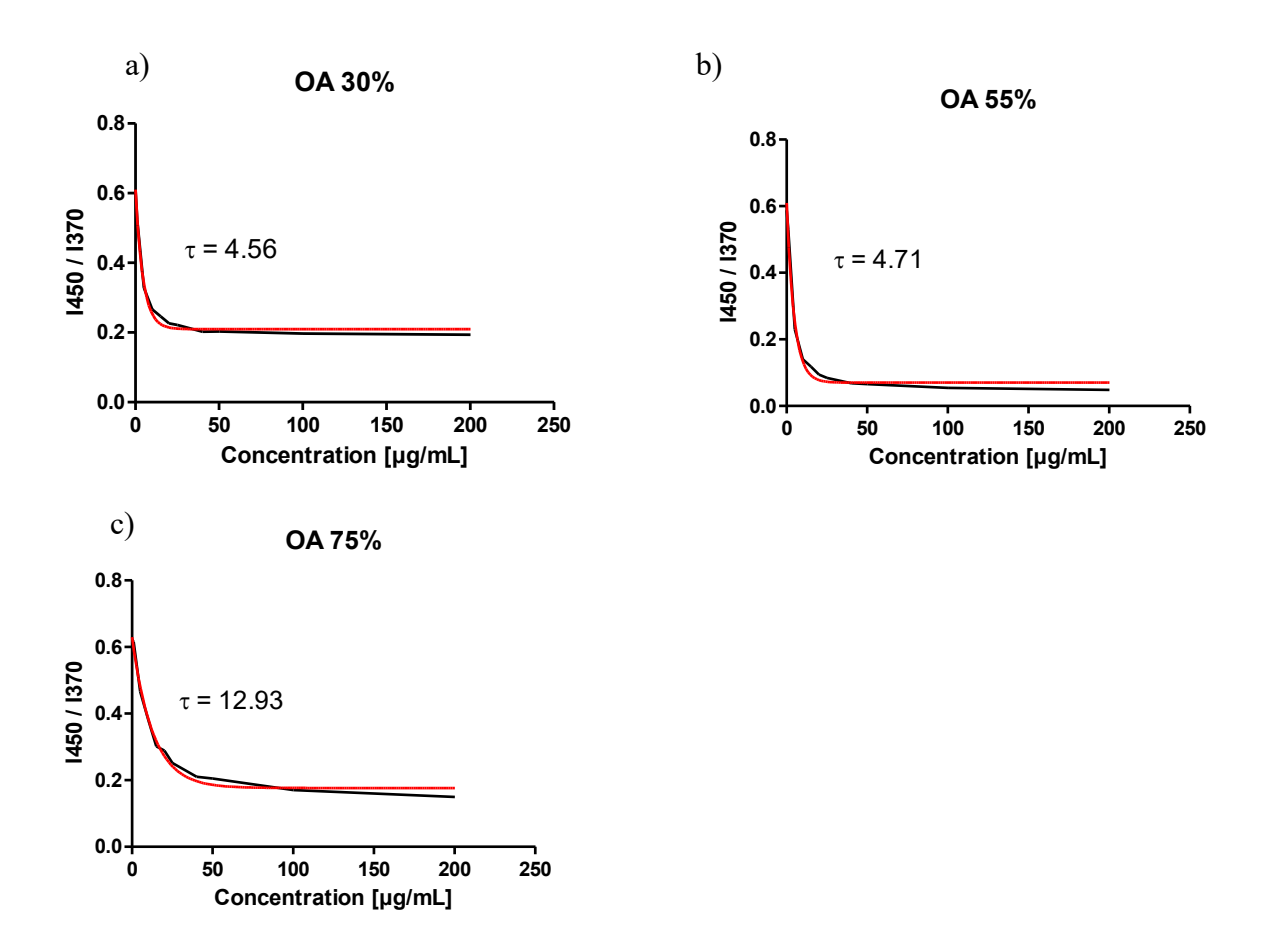


Figure S10. Difference in fluorescence emission spectra above (left) and below (right) the CMC.

To calculate the CMC, the ratio between fluorescence intensities between 450 nm and 370 nm was plotted against the polymer concentrations (Figure S11).



*Figure S11.* Intensity ratios from fluorescence spectra plotted against PBAE concentrations for a) 30%, b) 55%, and c) 75% OA. Depicted are the exponential decay curve fit (red) and measurement data (black).

The time constant  $\tau$  was extrapolated from the resulting curve fits and depicts the determined CMC. Noteworthy, the CMC values vary only slightly from each other in the investigated OA range. Since all nanoparticle formulations used in the study were prepared at concentrations exceeding the respective CMC by orders of magnitude, the differences between them were neglected in this study.

# VI. Summary and Perspective

Poly( $\beta$ -aminoesters) (PBAEs) have emerged as a highly versatile platform for RNA delivery. A key challenge in harnessing their full potential lies in the nuanced understanding and control of their step-growth polymerization. This challenge was addressed through the application of Design of Experiments (DoE), which enabled the systematic identification and quantification of the most influential factors governing polymer synthesis. Leveraging this data-driven approach, predictive models were developed to design novel PBAEs with tailored physicochemical properties. These model-derived predictions were subsequently validated through the synthesis and characterization of a new polymer library.

Comprehensive evaluation of critical performance metrics—including cytotoxicity, transfection efficiency, and colloidal stability—across this orthogonally designed polymer library yielded deeper mechanistic insights. Notably, a negative correlation was observed between particle stability and gene silencing efficiency, suggesting that excessive stability may impede intracellular release. Furthermore, the widely accepted paradigm that high transfection efficiency inherently coincides with increased toxicity was challenged by several of the findings presented.

To integrate and exploit these multifactorial insights, machine learning algorithms were employed, culminating in the identification of a new lead polymer candidate. This optimized polymer outperformed all previously developed variants in vitro, exhibiting both superior transfection efficiency and a favorable toxicity profile. However, in vivo studies revealed a lack of gene knockdown, prompting further investigation into the influence of delivery methodology.

This led to a third area of inquiry: the aerosolization of nanoparticles within a physiologically relevant 3D cell model. It was demonstrated that nanoparticles formulated from polymers with varying hydrophobicities could be successfully nebulized using a specifically selected vibrating mesh nebulizer, without compromising their physicochemical integrity. Intriguingly, the nebulization process appeared to modestly reduce particle internal stability—a phenomenon that may enhance transfection efficacy, as previously suggested.

In an ex vivo human pulmonary fibrosis model, nebulized nanoparticles carrying diseaserelevant siRNA effectively reduced target protein levels as well as downstream effector proteins. Surprisingly, the polymer that showed the weakest performance in conventional in vitro assays yielded the most pronounced gene silencing effect in this complex ex vivo system. This finding underscores the limitations of traditional in vitro models in predicting biological outcomes in more physiologically relevant environments, echoing the broader challenges faced in establishing reliable in vitro—in vivo correlations across pharmaceutical research.

Nevertheless, this study illustrates the power of combining statistical experimental design with rational optimization strategies to significantly accelerate lead identification and development. Such approaches promise to enhance research efficiency and translational potential.

The nanoparticles in this study were produced via manual batch mixing, a technique characterized by limited scalability, high user dependency, and poor reproducibility. Ongoing research aims to transition this process to microfluidic mixing platforms, which offer high-throughput, low-variance manufacturing capabilities suitable for clinical-scale production. Design of Experiments will once again play a pivotal role in optimizing formulation parameters to establish robust and scalable production workflows.

## VII. Publication List

#### **Unpublished Work:**

- Sieber-Schafer, F.; Kromer, APE.; Molbay, M; Carneiro, S; Jiang, M; Nguyen, A;
   Müller, J; Farfan Benito, J.; Merkel, OM\*. Machine Learning on an Orthogonal Polymer
   Library Reveals Governing Factors and Optimizes PBAE Copolymers' Synthesis and
   Performance Submitted to Biomaterials
- Coppola, PG, Kromer, APE, Boffito, M, Winkeljann, B, Ciardelli, G, Merkel, OM\*:
   Design of an injectable and bioerodible supramolecular hydrogel as local nucleic acid delivery system Submitted to Biomacromolecules
- Rademacker, S, Müller, JT, Kromer, APE, Carneiro, SP\*, Merkel, OM: Nanoparticle-mediated siRNA transfection in human epithelial lung cells cultured at the air-liquid interface Submitted to Springer Protocols Manuscripts

#### **Peer Reviewed Articles:**

- Sieber-Schäfer F, Jiang, M, Kromer, APE, Nguyen, A, Molbay, M, Carneiro, SP, Jürgens, D, Burgstaller, G, Popper, B, Winkeljann, B, Merkel, OM\*: Machine Learning-Enabled Polymer Discovery for Enhanced Pulmonary siRNA Delivery, Accepted in Advanced Functional Materials
- Müller, JT, Kromer, APE, Ezaddoustdar, A, Alexopoulos, I, Steinegger, KM, Porras-Gonzalez, DL, Berninghausen, O, Beckmann, R, Braubach, P, Burgstaller, G, Wygrecka, M, and Merkel, OM\*: Nebulization of RNA-Loaded Micelle-Embedded Polyplexes as a Potential Treatment of Idiopathic Pulmonary Fibrosis ACS Applied Materials & Interfaces DOI: 10.1021/acsami.4c21657
- Steinegger, KM, Allmendinger, L, Sturm, S, Sieber-Schäfer, F, Kromer, APE, Müller-Caspary, K, Winkeljann, B, Merkel, OM\*: Molecular Dynamics Simulations Elucidate the Molecular Organization of Poly(beta-amino ester) Based Polyplexes for siRNA Delivery Nano Letters 2024: doi: 10.1021/acs.nanolett.4c04291
- **Kromer, APE**, Sieber-Schäfer F, Farfan Benito J, Merkel OM\*: Design of Experiments Grants Mechanistic Insights into the Synthesis of Spermine-Containing PBAE Copolymers ACS Applied Materials and Interfaces 2024, ahead of print, https://doi.org/10.1021/acsami.4c06079

- Jin Y, Wang X, Kromer, APE, Müller J, Zimmermann C, Xu Z, Hartschuh A, Adams F, Merkel OM\*: Role of Hydrophobic Modification in Spermine-Based Poly(β-amino ester)s for siRNA Delivery and Their Spray-Dried Powders for Inhalation and Improved Storage *Biomacromolecules 2024, doi: 10.1021/acs.biomac.4c00283*
- Hartl N, Gabold B, Uhl P, Kromer A, Xiao X, Mier W, Fricker G, Liu R, Merkel OM:ApoE-functionalization of nanoparticles for targeted brain delivery-a feasible method for polyplexes? *Drug Delivery and Translational Research*, 2023, doi: 10.1007/s13346-023-01482-w.

#### **Poster Presentations:**

- **Kromer, APE**, Jin, Y, Merkel, OM\*: Design of Experiment methodology enables streamlined development of a siRNA based COVID-10 therapy *CRS Local Chapter Germany*, *Würzburg*, *Germany* 02-03.03.2023
- Kromer, APE, Müller, JT, Steinegger, K, Merkel, OM\*: Nebulization of siRNA: Estimating the Impact of the Transiction from Polyplex to Micelleplex CLINAM conference Basel, Switzerland, 8-9.10.2023
- **Kromer, APE**, Sieber-Schaefer, F, Merkel, OM\*: Design of Experiment Reveals Mechanistic Insights and Optimizes PBAE Copolymers' Synthesis and Performance *nanoDDS Florida*, *USA*, 13-15.09.2024
- Kromer, APE, Sieber-Schaefer, F, Molbay, M, Carneiro, S, Jiang, M, Nguyen, A, Merkel, OM\*: Design of Experiment Reveals Mechanistic Insights and Optimizes PBAE Copolymers' Synthesis and Performance CRS DeChAt Meeting Bern, Switzerland, 13-14.02.2025 Awarded with the Best Poster Award

### VIII. Reference List

- (1) Carthew, R. W.; Sontheimer, E. J. Origins and Mechanisms of miRNAs and siRNAs. *Cell* **2009**, *136* (4), 642–655. https://doi.org/10.1016/j.cell.2009.01.035.
- (2) Wilson, R. C.; Doudna, J. A. Molecular Mechanisms of RNA Interference. *Annu. Rev. Biophys.* **2013**, *42* (1), 217–239. https://doi.org/10.1146/annurev-biophys-083012-130404.
- (3) Fire, A.; Xu, S.; Montgomery, M. K.; Kostas, S. A.; Driver, S. E.; Mello, C. C. Potent and Specific Genetic Interference by Double-Stranded RNA in Caenorhabditis Elegans. *Nature* **1998**, *391* (6669), 806–811. https://doi.org/10.1038/35888.
- (4) Rivas, F. V.; Tolia, N. H.; Song, J.-J.; Aragon, J. P.; Liu, J.; Hannon, G. J.; Joshua-Tor, L. Purified Argonaute2 and an siRNA Form Recombinant Human RISC. *Nat. Struct. Mol. Biol.* **2005**, *12* (4), 340–349. https://doi.org/10.1038/nsmb918.
- (5) Wu, S. Y.; Lopez-Berestein, G.; Calin, G. A.; Sood, A. K. RNAi Therapies: Drugging the Undruggable. *Sci. Transl. Med.* **2014**, 6 (240), 240ps7. https://doi.org/10.1126/scitranslmed.3008362.
- (6) Ambike, S.; Cheng, C.-C.; Feuerherd, M.; Velkov, S.; Baldassi, D.; Afridi, S. Q.; Porras-Gonzalez, D.; Wei, X.; Hagen, P.; Kneidinger, N.; Stoleriu, M. G.; Grass, V.; Burgstaller, G.; Pichlmair, A.; Merkel, O. M.; Ko, C.; Michler, T. Targeting Genomic SARS-CoV-2 RNA with siRNAs Allows Efficient Inhibition of Viral Replication and Spread. *Nucleic Acids Res.* 2022, 50 (1), 333–349. https://doi.org/10.1093/nar/gkab1248.
- (7) Santoyo, J.; Vaquerizas, J. M.; Dopazo, J. Highly Specific and Accurate Selection of siRNAs for High-Throughput Functional Assays. *Bioinformatics* **2005**, *21* (8), 1376–1382. https://doi.org/10.1093/bioinformatics/bti196.
- (8) Paunovska, K.; Loughrey, D.; Dahlman, J. E. Drug Delivery Systems for RNA Therapeutics. *Nat. Rev. Genet.* **2022**, *23* (5), 265–280. https://doi.org/10.1038/s41576-021-00439-4.
- (9) Kumar, H.; Kawai, T.; Akira, S. Toll-like Receptors and Innate Immunity. *Biochem. Biophys. Res. Commun.* **2009**, *388* (4), 621–625. https://doi.org/10.1016/j.bbrc.2009.08.062.
- (10) Adams, D.; Gonzalez-Duarte, A.; O'Riordan, W. D.; Yang, C.-C.; Ueda, M.; Kristen, A. V.; Tournev, I.; Schmidt, H. H.; Coelho, T.; Berk, J. L.; Lin, K.-P.; Vita, G.; Attarian, S.; Planté-Bordeneuve, V.; Mezei, M. M.; Campistol, J. M.; Buades, J.; Brannagan, T. H.; Kim, B. J.; Oh, J.; Parman, Y.; Sekijima, Y.; Hawkins, P. N.; Solomon, S. D.; Polydefkis, M.; Dyck, P. J.; Gandhi, P. J.; Goyal, S.; Chen, J.; Strahs, A. L.; Nochur, S. V.; Sweetser, M. T.; Garg, P. P.; Vaishnaw, A. K.; Gollob, J. A.; Suhr, O. B. Patisiran, an RNAi Therapeutic, for Hereditary Transthyretin Amyloidosis. *N. Engl. J. Med.* **2018**, *379* (1), 11–21. https://doi.org/10.1056/NEJMoa1716153.
- (11) Mashima, R.; Takada, S. Lipid Nanoparticles: A Novel Gene Delivery Technique for Clinical Application. *Curr. Issues Mol. Biol.* **2022**, 44 (10), 5013–5027. https://doi.org/10.3390/cimb44100341.
- (12) Wagner, E.; Zenke, M.; Cotten, M.; Beug, H.; Birnstiel, M. L. Transferrin-Polycation Conjugates as Carriers for DNA Uptake into Cells. *Proc. Natl. Acad. Sci.* **1990**, *87* (9), 3410–3414. https://doi.org/10.1073/pnas.87.9.3410.
- (13) Singha, K.; Namgung, R.; Kim, W. J. Polymers in Small-Interfering RNA Delivery. *Nucleic Acid Ther.* **2011**, *21* (3), 133–147. https://doi.org/10.1089/nat.2011.0293.
- (14) Narasipura, E. A.; VanKeulen-Miller, R.; Ma, Y.; Fenton, O. S. Ongoing Clinical Trials of Nonviral siRNA Therapeutics. *Bioconjug. Chem.* **2023**, *34* (7), 1177–1197. https://doi.org/10.1021/acs.bioconjchem.3c00205.
- (15) Herdiana, Y.; Wathoni, N.; Shamsuddin, S.; Muchtaridi, M. Scale-up Polymeric-Based Nanoparticles Drug Delivery Systems: Development and Challenges. *OpenNano* **2022**, *7*, 100048. https://doi.org/10.1016/j.onano.2022.100048.
- (16) Kafil, V.; Omidi, Y. Cytotoxic Impacts of Linear and Branched Polyethylenimine Nanostructures in A431 Cells. *BioImpacts ISSN 2228-5660* **2011**. https://doi.org/10.5681/BI.2011.004.
- (17) Lynn, D. M.; Langer, R. Degradable Poly(β-Amino Esters): Synthesis, Characterization, and Self-Assembly with Plasmid DNA. *J. Am. Chem. Soc.* **2000**, *122* (44), 10761–10768. https://doi.org/10.1021/ja0015388.

- (18) Green, J. J.; Langer, R.; Anderson, D. G. A Combinatorial Polymer Library Approach Yields Insight into Nonviral Gene Delivery. *Acc. Chem. Res.* **2008**, *41* (6), 749–759. https://doi.org/10.1021/ar7002336.
- (19) Sunshine, J. C.; Akanda, M. I.; Li, D.; Kozielski, K. L.; Green, J. J. Effects of Base Polymer Hydrophobicity and End-Group Modification on Polymeric Gene Delivery. *Biomacromolecules* **2011**, *12* (10), 3592–3600. https://doi.org/10.1021/bm200807s.
- (20) Rui, Y.; Wilson, D. R.; Tzeng, S. Y.; Yamagata, H. M.; Sudhakar, D.; Conge, M.; Berlinicke, C. A.; Zack, D. J.; Tuesca, A.; Green, J. J. High-Throughput and High-Content Bioassay Enables Tuning of Polyester Nanoparticles for Cellular Uptake, Endosomal Escape, and Systemic in Vivo Delivery of mRNA. *Sci. Adv.* **2022**, *8* (1), eabk2855. https://doi.org/10.1126/sciadv.abk2855.
- (21) Jin, Y.; Wang, X.; Kromer, A. P. E.; Müller, J. T.; Zimmermann, C.; Xu, Z.; Hartschuh, A.; Adams, F.; Merkel, O. M. Role of Hydrophobic Modification in Spermine-Based Poly(β-Amino Ester)s for siRNA Delivery and Their Spray-Dried Powders for Inhalation and Improved Storage. *Biomacromolecules* **2024**, *25* (7), 4177–4191. https://doi.org/10.1021/acs.biomac.4c00283.
- (22) Mrksich, K.; Padilla, M. S.; Mitchell, M. J. Breaking the Final Barrier: Evolution of Cationic and Ionizable Lipid Structure in Lipid Nanoparticles to Escape the Endosome. *Adv. Drug Deliv. Rev.* **2024**, *214*, 115446. https://doi.org/10.1016/j.addr.2024.115446.
- (23) Behr, J.-P. The Proton Sponge: A Trick to Enter Cells the Viruses Did Not Exploit. *CHIMIA* **1997**, *51* (1–2), 34. https://doi.org/10.2533/chimia.1997.34.
- (24) Vermeulen, L. M. P.; De Smedt, S. C.; Remaut, K.; Braeckmans, K. The Proton Sponge Hypothesis: Fable or Fact? *Eur. J. Pharm. Biopharm.* **2018**, *129*, 184–190. https://doi.org/10.1016/j.ejpb.2018.05.034.
- (25) Ponomareva, N.; Brezgin, S.; Karandashov, I.; Kostyusheva, A.; Demina, P.; Slatinskaya, O.; Bayurova, E.; Silachev, D.; Pokrovsky, V. S.; Gegechkori, V.; Khaydukov, E.; Maksimov, G.; Frolova, A.; Gordeychuk, I.; Zamyatnin Jr., A. A.; Chulanov, V.; Parodi, A.; Kostyushev, D. Swelling, Rupture and Endosomal Escape of Biological Nanoparticles Per Se and Those Fused with Liposomes in Acidic Environment. *Pharmaceutics* **2024**, *16* (5), 667. https://doi.org/10.3390/pharmaceutics16050667.
- (26) Rehman, Z. U.; Hoekstra, D.; Zuhorn, I. S. Mechanism of Polyplex- and Lipoplex-Mediated Delivery of Nucleic Acids: Real-Time Visualization of Transient Membrane Destabilization without Endosomal Lysis. *ACS Nano* **2013**, *7*(5), 3767–3777. https://doi.org/10.1021/nn3049494.
- (27) Vaidyanathan, S.; Anderson, K. B.; Merzel, R. L.; Jacobovitz, B.; Kaushik, M. P.; Kelly, C. N.; Van Dongen, M. A.; Dougherty, C. A.; Orr, B. G.; Banaszak Holl, M. M. Quantitative Measurement of Cationic Polymer Vector and Polymer–pDNA Polyplex Intercalation into the Cell Plasma Membrane. *ACS Nano* **2015**, *9* (6), 6097–6109. https://doi.org/10.1021/acsnano.5b01263.
- (28) Jia, Y.; Wang, X.; Li, L.; Li, F.; Zhang, J.; Liang, X. Lipid Nanoparticles Optimized for Targeting and Release of Nucleic Acid. *Adv. Mater.* **2024**, *36* (4), 2305300. https://doi.org/10.1002/adma.202305300.
- (29) Stille, J. K. Step-Growth Polymerization. *J. Chem. Educ.* **1981**, *58* (11), 862. https://doi.org/10.1021/ed058p862.
- (30) Sir Fisher, R. A. The Design of Experiments, 7th ed.; Hafner Press: Adelaide, USA, 1935; Vol. 1.
- (31) Box, G. E. P.; Wilson, K. B. On the Experimental Attainment of Optimum Conditions. *J. R. Stat. Soc. Ser. B Stat. Methodol.* **1951**, *13* (1), 1–38. https://doi.org/10.1111/j.2517-6161.1951.tb00067.x.
- (32) Wehrlé, P.; Nobelis, Ph.; Cuiné, A.; Stamm, A. Response Surface Methodology: An Interesting Statistical Tool for Process Optimization and Validation: Example of Wet Granulation in a High-Shear Mixer. *Drug Dev. Ind. Pharm.* **1993**, *19* (13), 1637–1653. https://doi.org/10.3109/03639049309069333.
- (33) Adusumili, P. S.; Bolton, S. M. Evaluation of Cetacean Citrate Complexes as Matrices for Controlled Release Formulations Using a 3<sup>2</sup> Full Factorial Design. *Drug Dev. Ind. Pharm.* **1991**, No. 17, 1931–1945.
- (34) Takayama, K.; Imaizumi, H.; Nambu, N.; Nagai, T. Mathematical Optimization of Formulation of Indomethacin/Polyvinylpolypyrrolidone/Methyl Cellulose Solid Dispersions by the Sequential Unconstrained Minimization Technique. *Chem. Pharm. Bull. (Tokyo)* **1985**, *33* (1), 292–300. https://doi.org/10.1248/cpb.33.292.

- (35) Terada, T.; Kulkarni, J. A.; Huynh, A.; Chen, S.; Van Der Meel, R.; Tam, Y. Y. C.; Cullis, P. R. Characterization of Lipid Nanoparticles Containing Ionizable Cationic Lipids Using Design-of-Experiments Approach. *Langmuir* **2021**, *37* (3), 1120–1128. https://doi.org/10.1021/acs.langmuir.0c03039.
- (36) Billingsley, M. M.; Hamilton, A. G.; Mai, D.; Patel, S. K.; Swingle, K. L.; Sheppard, N. C.; June, C. H.; Mitchell, M. J. Orthogonal Design of Experiments for Optimization of Lipid Nanoparticles for mRNA Engineering of CAR T Cells. *Nano Lett.* **2022**, *22* (1), 533–542. https://doi.org/10.1021/acs.nanolett.1c02503.
- (37) Kauffman, K. J.; Dorkin, J. R.; Yang, J. H.; Heartlein, M. W.; DeRosa, F.; Mir, F. F.; Fenton, O. S.; Anderson, D. G. Optimization of Lipid Nanoparticle Formulations for mRNA Delivery in Vivo with Fractional Factorial and Definitive Screening Designs. *Nano Lett.* **2015**, *15* (11), 7300–7306. https://doi.org/10.1021/acs.nanolett.5b02497.
- (38) DeLoach, R. Analysis of Variance in the Modern Design of Experiments. In 48th AIAA Aerospace Sciences Meeting Including the New Horizons Forum and Aerospace Exposition; American Institute of Aeronautics and Astronautics: Orlando, Florida, 2010. https://doi.org/10.2514/6.2010-1111.
- (39) Desai, N. Challenges in Development of Nanoparticle-Based Therapeutics. *AAPS J.* **2012**, *14* (2), 282–295. https://doi.org/10.1208/s12248-012-9339-4.
- (40) Feldmann, D. P.; Xie, Y.; Jones, S. K.; Yu, D.; Moszczynska, A.; Merkel, O. M. The Impact of Microfluidic Mixing of Triblock Micelleplexes on in Vitro \$/\$ in Vivo Gene Silencing and Intracellular Trafficking. Nanotechnology 2017, 28 (22), 224001. https://doi.org/10.1088/1361-6528/aa6d15.
- (41) Mehta, M.; Bui, T. A.; Yang, X.; Aksoy, Y.; Goldys, E. M.; Deng, W. Lipid-Based Nanoparticles for Drug/Gene Delivery: An Overview of the Production Techniques and Difficulties Encountered in Their Industrial Development. *ACS Mater. Au* **2023**, *3* (6), 600–619. https://doi.org/10.1021/acsmaterialsau.3c00032.
- (42) Jürgens, D. C.; Deßloch, L.; Porras-Gonzalez, D.; Winkeljann, J.; Zielinski, S.; Munschauer, M.; Hörner, A. L.; Burgstaller, G.; Winkeljann, B.; Merkel, O. M. Lab-Scale siRNA and mRNA LNP Manufacturing by Various Microfluidic Mixing Techniques an Evaluation of Particle Properties and Efficiency. *OpenNano* **2023**, *12*, 100161. https://doi.org/10.1016/j.onano.2023.100161.
- (43) Huanbutta, K.; Sriamornsak, P.; Suwanpitak, K.; Klinchuen, N.; Deebugkum, T.; Teppitak, V.; Sangnim, T. Key Fabrications of Chitosan Nanoparticles for Effective Drug Delivery Using Flow Chemistry Reactors. *Int. J. Nanomedicine* **2023**, *18*, 7889–7900. https://doi.org/10.2147/IJN.S433756.
- (44) WHO. Global Health Estimates Technical Paper WHO/DDI/DNA/GHE/2024.2, 2024.
- (45) Patton, J. S. The Lungs as a Portal of Entry for Systemic Drug Delivery. *Proc. Am. Thorac. Soc.* **2004**, *I* (4), 338–344. https://doi.org/10.1513/pats.200409-049TA.
- (46) Pangeni, R.; Meng, T.; Poudel, S.; Sharma, D.; Hutsell, H.; Ma, J.; Rubin, B. K.; Longest, W.; Hindle, M.; Xu, Q. Airway Mucus in Pulmonary Diseases: Muco-Adhesive and Muco-Penetrating Particles to Overcome the Airway Mucus Barriers. *Int. J. Pharm.* **2023**, *634*, 122661. https://doi.org/10.1016/j.ijpharm.2023.122661.
- (47) Fernández-García, R.; Fraguas-Sánchez, A. I. Nanomedicines for Pulmonary Drug Delivery: Overcoming Barriers in the Treatment of Respiratory Infections and Lung Cancer. *Pharmaceutics* **2024**, *16* (12), 1584. https://doi.org/10.3390/pharmaceutics16121584.
- (48) Joshi, N.; Walter, J. M.; Misharin, A. V. Alveolar Macrophages. *Cell. Immunol.* **2018**, *330*, 86–90. https://doi.org/10.1016/j.cellimm.2018.01.005.
- (49) Gonsalves, A.; Menon, J. U. Impact of Nebulization on the Physicochemical Properties of Polymer–Lipid Hybrid Nanoparticles for Pulmonary Drug Delivery. *Int. J. Mol. Sci.* **2024**, *25* (9), 5028. https://doi.org/10.3390/ijms25095028.
- (50) Olszewski, O. Z.; MacLoughlin, R.; Blake, A.; O'Neill, M.; Mathewson, A.; Jackson, N. A Silicon-Based MEMS Vibrating Mesh Nebulizer for Inhaled Drug Delivery. *Procedia Eng.* **2016**, *168*, 1521–1524. https://doi.org/10.1016/j.proeng.2016.11.451.
- (51) Hertel, S.; Pohl, T.; Friess, W.; Winter, G. That's Cool! Nebulization of Thermolabile Proteins with a Cooled Vibrating Mesh Nebulizer. *Eur. J. Pharm. Biopharm.* **2014**, *87* (2), 357–365. https://doi.org/10.1016/j.ejpb.2014.03.001.

- (52) Zong, Y.; Lin, Y.; Wei, T.; Cheng, Q. Lipid Nanoparticle (LNP) Enables mRNA Delivery for Cancer Therapy. *Adv. Mater.* **2023**, *35* (51), 2303261. https://doi.org/10.1002/adma.202303261.
- (53) Kon, E.; Elia, U.; Peer, D. Principles for Designing an Optimal mRNA Lipid Nanoparticle Vaccine. *Curr. Opin. Biotechnol.* **2022**, 73, 329–336. https://doi.org/10.1016/j.copbio.2021.09.016.
- (54) De, A.; Ko, Y. T. Why mRNA-Ionizable LNPs Formulations Are so Short-Lived: Causes and Way-Out. *Expert Opin. Drug Deliv.* **2023**, *20* (2), 175–187. https://doi.org/10.1080/17425247.2023.2162876.
- (55) Schoenmaker, L.; Witzigmann, D.; Kulkarni, J. A.; Verbeke, R.; Kersten, G.; Jiskoot, W.; Crommelin, D. J. A. mRNA-Lipid Nanoparticle COVID-19 Vaccines: Structure and Stability. *Int. J. Pharm.* **2021**, *601*, 120586. https://doi.org/10.1016/j.ijpharm.2021.120586.
- (56) Patel, A. K.; Kaczmarek, J. C.; Bose, S.; Kauffman, K. J.; Mir, F.; Heartlein, M. W.; DeRosa, F.; Langer, R.; Anderson, D. G. Inhaled Nanoformulated mRNA Polyplexes for Protein Production in Lung Epithelium. *Adv. Mater.* **2019**, *31* (8), 1805116. https://doi.org/10.1002/adma.201805116.
- (57) Anderson, D. G.; Akinc, A.; Hossain, N.; Langer, R. Structure/Property Studies of Polymeric Gene Delivery Using a Library of Poly(β-Amino Esters). *Mol. Ther.* **2005**, *11* (3), 426–434. https://doi.org/10.1016/j.ymthe.2004.11.015.
- (58) Capasso Palmiero, U.; Kaczmarek, J. C.; Fenton, O. S.; Anderson, D. G. Poly(B-amino Ester)- *Co*-poly(Caprolactone) Terpolymers as Nonviral Vectors for mRNA Delivery In Vitro and In Vivo. *Adv. Healthc. Mater.* **2018**, *7* (14), 1800249. https://doi.org/10.1002/adhm.201800249.
- (59) Kozielski, K. L.; Ruiz-Valls, A.; Tzeng, S. Y.; Guerrero-Cázares, H.; Rui, Y.; Li, Y.; Vaughan, H. J.; Gionet-Gonzales, M.; Vantucci, C.; Kim, J.; Schiapparelli, P.; Al-Kharboosh, R.; Quiñones-Hinojosa, A.; Green, J. J. Cancer-Selective Nanoparticles for Combinatorial siRNA Delivery to Primary Human GBM in Vitro and in Vivo. *Biomaterials* **2019**, *209*, 79–87. https://doi.org/10.1016/j.biomaterials.2019.04.020.
- (60) Shi, J.; Zhang, Y.; Ma, B.; Yong, H.; Che, D.; Pan, C.; He, W.; Zhou, D.; Li, M. Enhancing the Gene Transfection of Poly(β-Amino Ester)/DNA Polyplexes by Modular Manipulation of Amphiphilicity. *ACS Appl. Mater. Interfaces* **2023**, *15* (36), 42130–42138. https://doi.org/10.1021/acsami.3c03802.
- (61) Li, Y.; He, Z.; A, S.; Wang, X.; Li, Z.; Johnson, M.; Foley, R.; Sáez, I. L.; Lyu, J.; Wang, W. Artificial Intelligence (AI)-Aided Structure Optimization for Enhanced Gene Delivery: The Effect of the Polymer Component Distribution (PCD). *ACS Appl. Mater. Interfaces* **2023**, *15* (30), 36667–36675. https://doi.org/10.1021/acsami.3c05010.
- (62) Eltoukhy, A. A.; Siegwart, D. J.; Alabi, C. A.; Rajan, J. S.; Langer, R.; Anderson, D. G. Effect of Molecular Weight of Amine End-Modified Poly(β-Amino Ester)s on Gene Delivery Efficiency and Toxicity. *Biomaterials* 2012, 33 (13), 3594–3603. https://doi.org/10.1016/j.biomaterials.2012.01.046.
- (63) Lv, H.; Zhang, S.; Wang, B.; Cui, S.; Yan, J. Toxicity of Cationic Lipids and Cationic Polymers in Gene Delivery. *J. Controlled Release* **2006**, *114* (1), 100–109. https://doi.org/10.1016/j.jconrel.2006.04.014.
- (64) Wolfert, M. A.; Dash, P. R.; Nazarova, O.; Oupicky, D.; Seymour, L. W.; Smart, S.; Strohalm, J.; Ulbrich, K. Polyelectrolyte Vectors for Gene Delivery: Influence of Cationic Polymer on Biophysical Properties of Complexes Formed with DNA. *Bioconjug. Chem.* 1999, 10 (6), 993–1004. https://doi.org/10.1021/bc990025r.
- (65) Design of Experiments. In *Applied Biostatistics for the Health Sciences*; John Wiley & Sons, Ltd, 2022; pp 508–541. https://doi.org/10.1002/9781119722717.ch11.
- (66) Kumar, R. Materiomically Designed Polymeric Vehicles for Nucleic Acids: Quo Vadis? *ACS Appl. Bio Mater.* **2022**, *5* (6), 2507–2535. https://doi.org/10.1021/acsabm.2c00346.
- (67) Patel, R. A.; Webb, M. A. Data-Driven Design of Polymer-Based Biomaterials: High-Throughput Simulation, Experimentation, and Machine Learning. *ACS Appl. Bio Mater.* **2024**, *7* (2), 510–527. https://doi.org/10.1021/acsabm.2c00962.
- (68) Li, B.; Raji, I. O.; Gordon, A. G. R.; Sun, L.; Raimondo, T. M.; Oladimeji, F. A.; Jiang, A. Y.; Varley, A.; Langer, R. S.; Anderson, D. G. Accelerating Ionizable Lipid Discovery for mRNA Delivery Using Machine Learning and Combinatorial Chemistry. *Nat. Mater.* **2024**, 1–7. https://doi.org/10.1038/s41563-024-01867-3.

- (69) Aparna Loecher; Michael Bruyns-Haylett; Pedro J. Ballester; Salvador Borrós; Nuria Oliva. A Machine Learning Approach to Predict Cellular Uptake of pBAE Polyplexes. *Biomater. Sci.* **2023**, *11* (17), 5797–5808. https://doi.org/10.1039/d3bm00741c.
- (70) Blakney, A. K.; McKay, P. F.; Ibarzo Yus, B.; Hunter, J. E.; Dex, E. A.; Shattock, R. J. The Skin You Are In: Design-of-Experiments Optimization of Lipid Nanoparticle Self-Amplifying RNA Formulations in Human Skin Explants. *ACS Nano* **2019**, *13* (5), 5920–5930. https://doi.org/10.1021/acsnano.9b01774.
- (71) Kumar, R.; Lahann, J. Predictive Model for the Design of Zwitterionic Polymer Brushes: A Statistical Design of Experiments Approach. *ACS Appl. Mater. Interfaces* **2016**, 8 (26), 16595–16603. https://doi.org/10.1021/acsami.6b04370.
- (72) Li, Z.; Guo, R.; Zhang, Z.; Yong, H.; Guo, L.; Chen, Z.; Huang, D.; Zhou, D. Enhancing Gene Transfection of Poly(β-Amino Ester)s through Modulation of Amphiphilicity and Chain Sequence. *J. Controlled Release* **2024**, *368*, 131–139. https://doi.org/10.1016/j.jconrel.2024.02.002.
- (73) Nguyen-Vu, V. L.; Pham, M. A.; Huynh, D. P. The Effects of Temperature, Feed Ratio, and Reaction Time on the Properties of Copolymer PLA-PEG-PLA. *Vietnam J. Sci. Technol. Eng.* **2019**, *61* (1), 9–13. https://doi.org/10.31276/VJSTE.61(1).09-13.
- (74) Zhang, Q.; Jiang, X.; He, A. Synthesis and Characterization of Trans-1,4-Butadiene/Isoprene Copolymers: Determination of Monomer Reactivity Ratios and Temperature Dependence. *Chin. J. Polym. Sci.* **2014**, *32* (8), 1068–1076. https://doi.org/10.1007/s10118-014-1467-0.
- (75) Jin, Y.; Wang, X.; Kromer, A. P. E.; Müller, J. T.; Zimmermann, C.; Xu, Z.; Hartschuh, A.; Adams, F.; Merkel, O. M. The Role of Hydrophobic Modification in Spermine-Based Poly(β-Amino Ester)s for siRNA Delivery and Their Spraydried Powders for Inhalation and Improved Storage. *Biomacromolecules*. https://doi.org/10.1021/acs.biomac.4c00283.
- (76) Jin, Y.; Adams, F.; Isert, L.; Baldassi, D.; Merkel, O. M. Spermine-Based Poly(β-Amino Ester)s for siRNA Delivery against Mutated KRAS in Lung Cancer. *Mol. Pharm.* **2023**, *20* (9), 4505–4516. https://doi.org/10.1021/acs.molpharmaceut.3c00206.
- (77) Jin, Y.; Adams, F.; Nguyen, A.; Sturm, S.; Carnerio, S.; Müller-Caspary, K.; Merkel, O. M. Synthesis and Application of Spermine-Based Amphiphilic Poly(β-Amino Ester)s for siRNA Delivery. *Nanoscale Adv.* **2023**, *5* (19), 5256–5262. https://doi.org/10.1039/D3NA00272A.
- (78) Rampado, R.; Peer, D. Design of Experiments in the Optimization of Nanoparticle-Based Drug Delivery Systems. *J. Controlled Release* **2023**, *358*, 398–419. https://doi.org/10.1016/j.jconrel.2023.05.001.
- (79) Bowden, G. D.; Pichler, B. J.; Maurer, A. A Design of Experiments (DoE) Approach Accelerates the Optimization of Copper-Mediated 18F-Fluorination Reactions of Arylstannanes. *Sci. Rep.* **2019**, *9* (1), 11370. https://doi.org/10.1038/s41598-019-47846-6.
- (80) Hartl, N.; Adams, F.; Costabile, G.; Isert, L.; Döblinger, M.; Xiao, X.; Liu, R.; Merkel, O. M. The Impact of Nylon-3 Copolymer Composition on the Efficiency of siRNA Delivery to Glioblastoma Cells. *Nanomaterials* **2019**, *9* (7), 986. https://doi.org/10.3390/nano9070986.
- (81) Craparo, E. F.; Drago, S. E.; Mauro, N.; Giammona, G.; Cavallaro, G. Design of New Polyaspartamide Copolymers for siRNA Delivery in Antiasthmatic Therapy. *Pharmaceutics* **2020**, *12* (2), 89. https://doi.org/10.3390/pharmaceutics12020089.
- (82) Zhang, J.; Cai, X.; Dou, R.; Guo, C.; Tang, J.; Hu, Y.; Chen, H.; Chen, J. Poly(β-Amino Ester)s-Based Nanovehicles: Structural Regulation and Gene Delivery. *Mol. Ther. Nucleic Acids* **2023**, 32, 568–581. https://doi.org/10.1016/j.omtn.2023.04.019.
- (83) Gogoi, R.; Alam, M. S.; Khandal, R. K.; Gogoi, R. Effect of Reaction Time on the Synthesis and Properties of Isocyanate Terminated Polyurethane Prepolymer. *Int. J. Eng. Res.* **2014**, *3* (5).
- (84) Zamora, R.; Delgado, R. M.; Hidalgo, F. J. Model Reactions of Acrylamide with Selected Amino Compounds. *J. Agric. Food Chem.* **2010**, *58* (3), 1708–1713. https://doi.org/10.1021/jf903378x.
- (85) Carothers, W. H. Polymers and Polyfunctionality. *Trans. Faraday Soc.* **1936**, *32* (0), 39–49. https://doi.org/10.1039/TF9363200039.
- (86) Weiss, A. M.; Lopez, M. A.; Rawe, B. W.; Manna, S.; Chen, Q.; Mulder, E. J.; Rowan, S. J.; Esser-Kahn, A. P. Understanding How Cationic Polymers' Properties Inform Toxic or Immunogenic Responses via Parametric Analysis. *Macromolecules* **2023**, *56* (18), 7286–7299. https://doi.org/10.1021/acs.macromol.3c01223.

- (87) Tanne, J. H. Covid-19: FDA Approves Pfizer-BioNTech Vaccine in Record Time. *BMJ* **2021**, *374*, n2096. https://doi.org/10.1136/bmj.n2096.
- (88) Polack, F. P.; Thomas, S. J.; Kitchin, N.; Absalon, J.; Gurtman, A.; Lockhart, S.; Perez, J. L.; Marc, G. P.; Moreira, E. D.; Zerbini, C.; Bailey, R.; Swanson, K. A.; Roychoudhury, S.; Koury, K.; Li, P.; Kalina, W. V.; Cooper, D.; Frenck, R. W.; Hammitt, L. L.; Türeci, Ö.; Nell, H.; Schaefer, A.; Ünal, S.; Tresnan, D. B.; Mather, S.; Dormitzer, P. R.; Şahin, U.; Jansen, K. U.; Gruber, W. C. Safety and Efficacy of the BNT162b2 mRNA Covid-19 Vaccine. *N. Engl. J. Med.* 2020, 383 (27), 2603–2615. https://doi.org/10.1056/NEJMoa2034577.
- (89) Bowden-Reid, E.; Moles, E.; Kelleher, A.; Ahlenstiel, C. Harnessing Antiviral RNAi Therapeutics for Pandemic Viruses: SARS-CoV-2 and HIV. *Drug Deliv. Transl. Res.* **2025**. https://doi.org/10.1007/s13346-025-01788-x.
- (90) Jin, Y.; Adams, F.; Möller, J.; Isert, L.; Zimmermann, C. M.; Keul, D.; Merkel, O. M. Synthesis and Application of Low Molecular Weight PEI-Based Copolymers for siRNA Delivery with Smart Polymer Blends. *Macromol. Biosci.* **2023**, *23* (2), 2200409. https://doi.org/10.1002/mabi.202200409.
- (91) Toruntay, C.; Poyraz, F. S.; Susgun, S.; Yucesan, E.; Mansuroglu, B. Anticancer Effects of MAPK6 siRNA-Loaded PLGA Nanoparticles in the Treatment of Breast Cancer. *J. Cell. Mol. Med.* **2025**, *29* (2), e70309. https://doi.org/10.1111/jcmm.70309.
- (92) Lahan, M.; Saikia, T.; Dutta, K.; Baishya, R.; Bharali, A.; Baruah, S.; Bharadwaj, R.; Medhi, S.; Sahu, B. P. Multifunctional Approach with LHRH-Mediated PLGA Nanoconjugate for Site-Specific Codelivery of Curcumin and BCL2 siRNA in Mice Lung Cancer. *Future J. Pharm. Sci.* **2024**, *10* (1), 163. https://doi.org/10.1186/s43094-024-00743-w.
- (93) Kozielski, K. L.; Tzeng, S. Y.; Green, J. J. A Bioreducible Linear Poly(β-Amino Ester) for siRNA Delivery. *Chem. Commun.* **2013**, *49* (46), 5319. https://doi.org/10.1039/c3cc40718g.
- (94) Rui, Y.; Wilson, D. R.; Tzeng, S. Y.; Yamagata, H. M.; Sudhakar, D.; Conge, M.; Berlinicke, C. A.; Zack, D. J.; Tuesca, A.; Green, J. J. High-Throughput and High-Content Bioassay Enables Tuning of Polyester Nanoparticles for Cellular Uptake, Endosomal Escape, and Systemic in Vivo Delivery of mRNA. *Sci. Adv.* **2022**, *8* (1), eabk2855. https://doi.org/10.1126/sciadv.abk2855.
- (95) Eltoukhy, A. A.; Siegwart, D. J.; Alabi, C. A.; Rajan, J. S.; Langer, R.; Anderson, D. G. Effect of Molecular Weight of Amine End-Modified Poly(β-Amino Ester)s on Gene Delivery Efficiency and Toxicity. *Biomaterials* 2012, 33 (13), 3594–3603. https://doi.org/10.1016/j.biomaterials.2012.01.046.
- (96) Jogdeo, C. M.; Siddhanta, K.; Das, A.; Ding, L.; Panja, S.; Kumari, N.; Oupický, D. Beyond Lipids: Exploring Advances in Polymeric Gene Delivery in the Lipid Nanoparticles Era. *Adv. Mater.* **2024**, *36* (31), 2404608. https://doi.org/10.1002/adma.202404608.
- (97) Shan, X.; Cai, Y.; Zhu, B.; Zhou, L.; Sun, X.; Xu, X.; Yin, Q.; Wang, D.; Li, Y. Rational Strategies for Improving the Efficiency of Design and Discovery of Nanomedicines. *Nat. Commun.* **2024**, *15* (1), 9990. https://doi.org/10.1038/s41467-024-54265-3.
- (98) Wan, Q.; Sun, Y.; Sun, X.; Zhou, Z. Rational Design of Polymer-Based mRNA Delivery Systems for Cancer Treatment. *Polym. Chem.* **2024**, *15* (24), 2437–2456. https://doi.org/10.1039/D4PY00206G.
- (99) Wu, C.; Li, J.; Wang, W.; Hammond, P. T. Rationally Designed Polycationic Carriers for Potent Polymeric siRNA-Mediated Gene Silencing. *ACS Nano* **2018**, *12* (7), 6504–6514. https://doi.org/10.1021/acsnano.7b08777.
- (100) Yan, Y.; Xiong, H.; Zhang, X.; Cheng, Q.; Siegwart, D. J. Systemic mRNA Delivery to the Lungs by Functional Polyester-Based Carriers. *Biomacromolecules* **2017**, *18* (12), 4307–4315. https://doi.org/10.1021/acs.biomac.7b01356.
- (101) Anderson, D. G.; Akinc, A.; Hossain, N.; Langer, R. Structure/Property Studies of Polymeric Gene Delivery Using a Library of Poly(β-Amino Esters). *Mol. Ther.* **2005**, *11* (3), 426–434. https://doi.org/10.1016/j.ymthe.2004.11.015.
- (102) N. Politis, S.; Colombo, P.; Colombo, G.; M. Rekkas, D. Design of Experiments (DoE) in Pharmaceutical Development. *Drug Dev. Ind. Pharm.* **2017**, *43* (6), 889–901. https://doi.org/10.1080/03639045.2017.1291672.

- (103) Coley, C. W.; Barzilay, R.; Green, W. H.; Jaakkola, T. S.; Jensen, K. F. Convolutional Embedding of Attributed Molecular Graphs for Physical Property Prediction. *J. Chem. Inf. Model.* **2017**, *57* (8), 1757–1772. https://doi.org/10.1021/acs.jcim.6b00601.
- (104) Gómez-Bombarelli, R.; Wei, J. N.; Duvenaud, D.; Hernández-Lobato, J. M.; Sánchez-Lengeling, B.; Sheberla, D.; Aguilera-Iparraguirre, J.; Hirzel, T. D.; Adams, R. P.; Aspuru-Guzik, A. Automatic Chemical Design Using a Data-Driven Continuous Representation of Molecules. *ACS Cent. Sci.* **2018**, *4* (2), 268–276. https://doi.org/10.1021/acscentsci.7b00572.
- (105) Lin, Z.; Chou, W.-C.; Cheng, Y.-H.; He, C.; Monteiro-Riviere, N. A.; Riviere, J. E. Predicting Nanoparticle Delivery to Tumors Using Machine Learning and Artificial Intelligence Approaches. *Int. J. Nanomedicine* **2022**, *17*, 1365–1379. https://doi.org/10.2147/IJN.S344208.
- (106) McDonald, S. M.; Augustine, E. K.; Lanners, Q.; Rudin, C.; Catherine Brinson, L.; Becker, M. L. Applied Machine Learning as a Driver for Polymeric Biomaterials Design. *Nat. Commun.* **2023**, *14* (1), 4838. https://doi.org/10.1038/s41467-023-40459-8.
- (107) Kumar, R.; Le, N.; Tan, Z.; Brown, M. E.; Jiang, S.; Reineke, T. M. Efficient Polymer-Mediated Delivery of Gene-Editing Ribonucleoprotein Payloads through Combinatorial Design, Parallelized Experimentation, and Machine Learning. *ACS Nano* **2020**, *14* (12), 17626–17639. https://doi.org/10.1021/acsnano.0c08549.
- (108) Dennis Gong; Dennis Gong; Ben-Akiva, E.; Elana Ben-Akiva; Arshdeep Singh; Arshdeep Singh; Hannah Yamagata; Hannah M. Yamagata; Savannah Est-Witte; Savannah Est-Witte; Julie K. Shade; Julie K. Shade; Trayanova, N. A.; Natalia A. Trayanova; Green, J. J.; Jordan J. Green. Machine Learning Guided Structure Function Predictions Enable In Silico Nanoparticle Screening for Polymeric Gene Delivery. *Acta Biomater.* 2022. https://doi.org/10.1016/j.actbio.2022.09.072.
- (109) Kromer, A. P. E.; Sieber-Schäfer, F.; Farfan Benito, J.; Merkel, O. M. Design of Experiments Grants Mechanistic Insights into the Synthesis of Spermine-Containing PBAE Copolymers. *ACS Appl. Mater. Interfaces* **2024**, *16* (29), 37545–37554. https://doi.org/10.1021/acsami.4c06079.
- (110) Lundberg, S.; Lee, S.-I. A Unified Approach to Interpreting Model Predictions. arXiv November 25, 2017. https://doi.org/10.48550/arXiv.1705.07874.
- (111) Jin, Y.; Adams, F.; Isert, L.; Baldassi, D.; Merkel, O. M. Spermine-Based Poly(β-Amino Ester)s for siRNA Delivery against Mutated KRAS in Lung Cancer. *Mol. Pharm.* **2023**, *20* (9), 4505–4516. https://doi.org/10.1021/acs.molpharmaceut.3c00206.
- (112) Stability, Intracellular Delivery, and Release of siRNA from Chitosan Nanoparticles Using Different Cross-Linkers | PLOS One. https://journals.plos.org/plosone/article?id=10.1371/journal.pone.0128963 (accessed 2025-02-28).
- (113) Müller, J. T.; Kromer, A. P. E.; Ezaddoustdar, A.; Alexopoulos, I.; Steinegger, K. M.; Porras-Gonzalez, D. L.; Berninghausen, O.; Beckmann, R.; Braubach, P.; Burgstaller, G.; Wygrecka, M.; Merkel, O. M. Nebulization of RNA-Loaded Micelle-Embedded Polyplexes as a Potential Treatment of Idiopathic Pulmonary Fibrosis. *ACS Appl. Mater. Interfaces* **2025**, *17* (8), 11861–11872. https://doi.org/10.1021/acsami.4c21657.
- (114) Cirman, T.; Orešić, K.; Mazovec, G. D.; Turk, V.; Reed, J. C.; Myers, R. M.; Salvesen, G. S.; Turk, B. Selective Disruption of Lysosomes in HeLa Cells Triggers Apoptosis Mediated by Cleavage of Bid by Multiple Papain-like Lysosomal Cathepsins \*. J. Biol. Chem. 2004, 279 (5), 3578–3587. https://doi.org/10.1074/jbc.M308347200.
- (115) Melo, F. R.; Lundequist, A.; Calounova, G.; Wernersson, S.; Pejler, G. Lysosomal Membrane Permeabilization Induces Cell Death in Human Mast Cells. *Scand. J. Immunol.* **2011**, 74 (4), 354–362. https://doi.org/10.1111/j.1365-3083.2011.02589.x.
- (116) Sun, F.; Dong, B.; Zhang, H.; Tian, M. Permeability-Controlled Probe for Ratiometric Detection of Plasma Membrane Integrity and Late Apoptosis. *ACS Sens.* **2024**, *9* (11), 6092–6102. https://doi.org/10.1021/acssensors.4c01963.
- (117) Bannigan, P.; Bao, Z.; Hickman, R. J.; Aldeghi, M.; Häse, F.; Aspuru-Guzik, A.; Allen, C. Machine Learning Models to Accelerate the Design of Polymeric Long-Acting Injectables. *Nat. Commun.* **2023**, *14* (1), 35. https://doi.org/10.1038/s41467-022-35343-w.
- (118) Lu, W.-C.; Ji, X.-B.; Li, M.-J.; Liu, L.; Yue, B.-H.; Zhang, L.-M. Using Support Vector Machine for Materials Design. *Adv. Manuf.* **2013**, *1* (2), 151–159. https://doi.org/10.1007/s40436-013-0025-2.

- (119) Hartl, N.; Jürgens, D. C.; Carneiro, S.; König, A.-C.; Xiao, X.; Liu, R.; Hauck, S. M.; Merkel, O. M. Protein Corona Investigations of Polyplexes with Varying Hydrophobicity From Method Development to in Vitro Studies. *Int. J. Pharm.* **2023**, *643*, 123257. https://doi.org/10.1016/j.ijpharm.2023.123257.
- (120) Qiu, Y.; Lam, J.; Leung, S.; Liang, W. Delivery of RNAi Therapeutics to the Airways—From Bench to Bedside. *Molecules* **2016**, *21* (9), 1249. https://doi.org/10.3390/molecules21091249.
- (121) Guo, F.; Li, Y.; Yu, W.; Fu, Y.; Zhang, J.; Cao, H. Recent Progress of Small Interfering RNA Delivery on the Market and Clinical Stage. *Mol. Pharm.* **2024**, *21* (5), 2081–2096. https://doi.org/10.1021/acs.molpharmaceut.3c01158.
- (122) Neary, M. T.; Mulder, L. M.; Kowalski, P. S.; MacLoughlin, R.; Crean, A. M.; Ryan, K. B. Nebulised Delivery of RNA Formulations to the Lungs: From Aerosol to Cytosol. *J. Controlled Release* **2024**, *366*, 812–833. https://doi.org/10.1016/j.jconrel.2023.12.012.
- (123) Kleemann, E.; Schmehl, T.; Gessler, T.; Bakowsky, U.; Kissel, T.; Seeger, W. Iloprost-Containing Liposomes for Aerosol Application in Pulmonary Arterial Hypertension: Formulation Aspects and Stability. *Pharm. Res.* **2007**, *24* (2), 277–287. https://doi.org/10.1007/PL00022055.
- (124) Arzhavitina, A.; Steckel, H. Surface Active Drugs Significantly Alter the Drug Output Rate from Medical Nebulizers. *Int. J. Pharm.* **2010**, 384 (1–2), 128–136. https://doi.org/10.1016/j.ijpharm.2009.10.012.
- (125) Beck-Broichsitter, M.; Kleimann, P.; Schmehl, T.; Betz, T.; Bakowsky, U.; Kissel, T.; Seeger, W. Impact of Lyoprotectants for the Stabilization of Biodegradable Nanoparticles on the Performance of Air-Jet, Ultrasonic, and Vibrating-Mesh Nebulizers. *Eur. J. Pharm. Biopharm.* **2012**, *82* (2), 272–280. https://doi.org/10.1016/j.ejpb.2012.07.004.
- (126) Chanda, D.; Otoupalova, E.; Smith, S. R.; Volckaert, T.; De Langhe, S. P.; Thannickal, V. J. Developmental Pathways in the Pathogenesis of Lung Fibrosis. *Mol. Aspects Med.* **2019**, *65*, 56–69. https://doi.org/10.1016/j.mam.2018.08.004.
- (127) Tomos, I.; Roussis, I.; Matthaiou, A. M.; Dimakou, K. Molecular and Genetic Biomarkers in Idiopathic Pulmonary Fibrosis: Where Are We Now? *Biomedicines* **2023**, *11* (10), 2796. https://doi.org/10.3390/biomedicines11102796.
- (128) El Agha, E.; Wygrecka, M. State of the Art in Idiopathic Pulmonary Fibrosis. *Cells* **2022**, *11* (16), 2487. https://doi.org/10.3390/cells11162487.
- (129) Jacquemart, I.; Pamuła, E.; De Cupere, V. M.; Rouxhet, P. G.; Dupont-Gillain, Ch. C. Nanostructured Collagen Layers Obtained by Adsorption and Drying. *J. Colloid Interface Sci.* **2004**, *278* (1), 63–70. https://doi.org/10.1016/j.jcis.2004.05.040.
- (130) Dupont-Gillain, C. C. Understanding and Controlling Type I Collagen Adsorption and Assembly at Interfaces, and Application to Cell Engineering. *Colloids Surf. B Biointerfaces* **2014**, *124*, 87–96. https://doi.org/10.1016/j.colsurfb.2014.08.029.
- (131) Craig, V. J.; Zhang, L.; Hagood, J. S.; Owen, C. A. Matrix Metalloproteinases as Therapeutic Targets for Idiopathic Pulmonary Fibrosis. *Am. J. Respir. Cell Mol. Biol.* **2015**, *53* (5), 585–600. https://doi.org/10.1165/rcmb.2015-0020TR.
- (132) Chilosi, M.; Poletti, V.; Zamò, A.; Lestani, M.; Montagna, L.; Piccoli, P.; Pedron, S.; Bertaso, M.; Scarpa, A.; Murer, B.; Cancellieri, A.; Maestro, R.; Semenzato, G.; Doglioni, C. Aberrant Wnt/β-Catenin Pathway Activation in Idiopathic Pulmonary Fibrosis. *Am. J. Pathol.* **2003**, *162* (5), 1495–1502. https://doi.org/10.1016/S0002-9440(10)64282-4.
- (133) Ślusarz, A.; Nichols, L. A.; Grunz-Borgmann, E. A.; Chen, G.; Akintola, A. D.; Catania, J. M.; Burghardt, R. C.; Trzeciakowski, J. P.; Parrish, A. R. Overexpression of MMP-7 Increases Collagen 1A2 in the Aging Kidney. *Physiol. Rep.* **2013**, *I* (5). https://doi.org/10.1002/phy2.90.
- (134) Rosas, I. O.; Richards, T. J.; Konishi, K.; Zhang, Y.; Gibson, K.; Lokshin, A. E.; Lindell, K. O.; Cisneros, J.; MacDonald, S. D.; Pardo, A.; Sciurba, F.; Dauber, J.; Selman, M.; Gochuico, B. R.; Kaminski, N. MMP1 and MMP7 as Potential Peripheral Blood Biomarkers in Idiopathic Pulmonary Fibrosis. *PLoS Med.* **2008**, *5* (4), e93. https://doi.org/10.1371/journal.pmed.0050093.
- (135) Zuo, F.; Kaminski, N.; Eugui, E.; Allard, J.; Yakhini, Z.; Ben-Dor, A.; Lollini, L.; Morris, D.; Kim, Y.; DeLustro, B.; Sheppard, D.; Pardo, A.; Selman, M.; Heller, R. A. Gene Expression Analysis Reveals Matrilysin as a Key Regulator of Pulmonary Fibrosis in Mice and Humans. *Proc. Natl. Acad. Sci.* **2002**, *99* (9), 6292–6297. https://doi.org/10.1073/pnas.092134099.

- (136) Carneiro, S.; Müller, J. T.; Merkel, O. M. RNA Amplification and Analysis: Methods and Protocols; Springer US, 2024; pp 187–203.
- (137) Steinegger, K. M.; Allmendinger, L.; Sturm, S.; Sieber-Schäfer, F.; Kromer, A. P. E.; Müller-Caspary, K.; Winkeljann, B.; Merkel, O. M. Molecular Dynamics Simulations Elucidate the Molecular Organization of Poly(Beta-Amino Ester) Based Polyplexes for siRNA Delivery. *Nano Lett.* **2024**, *24* (49), 15683–15692. https://doi.org/10.1021/acs.nanolett.4c04291.
- (138) Allan, C.; Burel, J.-M.; Moore, J.; Blackburn, C.; Linkert, M.; Loynton, S.; MacDonald, D.; Moore, W. J.; Neves, C.; Patterson, A.; Porter, M.; Tarkowska, A.; Loranger, B.; Avondo, J.; Lagerstedt, I.; Lianas, L.; Leo, S.; Hands, K.; Hay, R. T.; Patwardhan, A.; Best, C.; Kleywegt, G. J.; Zanetti, G.; Swedlow, J. R. OMERO: Flexible, Model-Driven Data Management for Experimental Biology. *Nat. Methods* **2012**, *9* (3), 245–253. https://doi.org/10.1038/nmeth.1896.
- (139) Nelson, C. E.; Kintzing, J. R.; Hanna, A.; Shannon, J. M.; Gupta, M. K.; Duvall, C. L. Balancing Cationic and Hydrophobic Content of PEGylated siRNA Polyplexes Enhances Endosome Escape, Stability, Blood Circulation Time, and Bioactivity *in Vivo. ACS Nano* **2013**, *7* (10), 8870–8880. https://doi.org/10.1021/nn403325f.
- (140) Ogris, M.; Brunner, S.; Schüller, S.; Kircheis, R.; Wagner, E. PEGylated DNA/Transferrin–PEI Complexes: Reduced Interaction with Blood Components, Extended Circulation in Blood and Potential for Systemic Gene Delivery. *Gene Ther.* **1999**, *6* (4), 595–605. https://doi.org/10.1038/sj.gt.3300900.
- (141) Kromer, A. P. E.; Sieber-Schäfer, F.; Farfan Benito, J.; Merkel, O. M. Design of Experiments Grants Mechanistic Insights into the Synthesis of Spermine-Containing PBAE Copolymers. *ACS Appl. Mater. Interfaces* **2024**, *16* (29), 37545–37554. https://doi.org/10.1021/acsami.4c06079.
- (142) Jeon, S.; Clavadetscher, J.; Lee, D.-K.; Chankeshwara, S. V.; Bradley, M.; Cho, W.-S. Surface Charge-Dependent Cellular Uptake of Polystyrene Nanoparticles. *Nanomaterials* **2018**, *8* (12), 1028. https://doi.org/10.3390/nano8121028.
- (143) Van Rijn, C. J. M.; Vlaming, K. E.; Bem, R. A.; Dekker, R. J.; Poortinga, A.; Breit, T.; Van Leeuwen, S.; Ensink, W. A.; Van Wijnbergen, K.; Van Hamme, J. L.; Bonn, D.; Geijtenbeek, T. B. H. Low Energy Nebulization Preserves Integrity of SARS-CoV-2 mRNA Vaccines for Respiratory Delivery. Sci. Rep. 2023, 13 (1), 8851. https://doi.org/10.1038/s41598-023-35872-4.
- (144) Ray, L. Nanotechnology-Based Targeted Drug Delivery Systems for Lung Cancer; Academic Press, 2019; Vol. 4, pp 77–93.
- (145) Ghazanfari, T.; Elhissi, A. M. A.; Ding, Z.; Taylor, K. M. G. The Influence of Fluid Physicochemical Properties on Vibrating-Mesh Nebulization. *Int. J. Pharm.* **2007**, *339* (1–2), 103–111. https://doi.org/10.1016/j.ijpharm.2007.02.035.
- (146) Zhang, G.; David, A.; Wiedmann, T. S. Performance of the Vibrating Membrane Aerosol Generation Device: Aeroneb Micropump Nebulizer<sup>TM</sup>. *J. Aerosol Med.* **2007**, *20* (4), 408–416. https://doi.org/10.1089/jam.2007.0622.
- (147) Cedilak, M.; Banjanac, M.; Belamarić, D.; Paravić Radičević, A.; Faraho, I.; Ilić, K.; Čužić, S.; Glojnarić, I.; Eraković Haber, V.; Bosnar, M. Precision-Cut Lung Slices from Bleomycin Treated Animals as a Model for Testing Potential Therapies for Idiopathic Pulmonary Fibrosis. *Pulm. Pharmacol. Ther.* **2019**, *55*, 75–83. https://doi.org/10.1016/j.pupt.2019.02.005.
- (148) Wygrecka, M.; Kwapiszewska, G.; Jablonska, E.; Gerlach, S. V.; Henneke, I.; Zakrzewicz, D.; Guenther, A.; Preissner, K. T.; Markart, P. Role of Protease-Activated Receptor-2 in Idiopathic Pulmonary Fibrosis. *Am. J. Respir. Crit. Care Med.* **2011**, *183* (12), 1703–1714. https://doi.org/10.1164/rccm.201009-1479OC.

# IX. Acknowledgments

First and foremost, I would like to extend my deepest and most sincere gratitude to my supervisor, **Prof. Dr. Olivia Merkel**, whose unwavering passion and dedication have been a source of inspiration since the moment I joined her group in 2019. It has been a privilege to witness the group evolve and flourish over the years. Thank you for opening doors to a multitude of scientific fields — many of which I have come to hold close to my heart — and for the immense effort, insightful guidance, and steadfast support you have invested in this project. I am especially grateful for the trust you placed in me, allowing me the space to grow and ultimately become an expert in a field of my own.

My heartfelt appreciation goes to **Prof. Dr. Wolfgang Frieß** and his team, who always broadened my perspective not only on science but the extracurricular life as well. I am especially grateful for his role as my co-referee.

To **Prof. Dr. Ernst Wagner**, I extend my warmest thanks for introducing me to the fascinating world of "polyplexes" back in 2018 — a field so captivating that it has shaped the direction of my research ever since.

I am equally thankful to **PD Dr. Karin Bartel** and her group for the fruitful scientific exchanges, especially in all matters related to cell culture. Your collaboration has been a vital part of this journey.

My sincere thanks go to the **European Research Council (ERC)**. I hold the ERC in the highest regard — not only for funding this project, but for its unwavering support of independent research across Europe, which is more vital now than ever.

I am also grateful to the LMU institution, which has provided me with the opportunity to study and contribute to the field of pharmaceutical sciences.

To my **coauthors**: this work would not have been possible without you. Thank you for your invaluable contributions, stimulating discussions, and the countless late nights spent responding to reviewer comments.

A heartfelt thank you to the entire **Merkel Lab**. You have created an environment filled with support, enthusiasm, and collaboration. A special mention goes to my lab mate — your helping

hand was always there when I needed it most. I leave the lab confident that the soothing presence of the *passion flower* will continue to keep the atmosphere light and bright.

On a broader note, I would like to thank my fellow students **Lina Ouologuem**, **Michelle Peter**, and **Thomas Zerbes** as well as all my other friends I met along the way. Your presence lightened the load and brightened the journey. While a friendship may be built on shared laughter, the bond between lab partners is forged in flame, failure, and the occasional burst of toxic gas — a quiet trust born from precision, perseverance, and shared discovery.

To my friends back home — thank you for welcoming me with open arms every time I return. Though distance separates us, your support has never faltered.

I am deeply thankful to my **parents** for setting me on this path and shaping the outline of the person I became, to my **brother** — for being a lifelong role model and for igniting my motivation to pursue a PhD — and to my **sister**, for always lending a listening ear. To my **grandmother**: thank you for the deep and thought-provoking conversations. You are a shining example of what it means to be human. I hope to carry your boundless curiosity with me always.

To **R** and **A** — I miss you dearly.

Lastly, and above all, I want to thank my **wife**. Your unwavering support made this dissertation possible. When all else failed, you were my anchor and my safe harbor. You know every part of me in a way no one else ever could, and for that, I am eternally grateful. Words cannot fully express the depth of my gratitude.